UNIVERSITAT POLITÈCNICA DE VALENCIA

Instituto de Ingeniería Mecánica y Biomecánica - I2MB

PhD Thesis

Development of topology optimization techniques for noise pollution minimization in acoustic and fluid-structure problems

Presented by: Borja Ferrándiz Catalá

Supervised by: Ph.D. José Martínez Casas

Ph.D. Enrique Nadal Soriano

Advised by: Prof. Francisco David Denia Guzmán

Valencia, July 2023

PhD Thesis

Development of topology optimization techniques for noise pollution minimization in acoustic and fluid-structure problems

for the degree of

Doctor in Industrial Engineering and Production

presented by

Borja Ferrándiz Catalá

at the

Instituto de Ingeniería Mecánica y Biomecánica - I2MB

of Universitat Politècnica de Valencia

Supervised by

Ph.D. José Martínez Casas

Ph.D. Enrique Nadal Soriano

Advised by

Prof. Francisco David Denia Guzmán

Valencia, July 2023

PhD Thesis

Development of topology optimization techniques for noise pollution minimization in acoustic and fluid-structure problems

Presented by: Borja Ferrándiz Catalá

Supervised by: Ph.D. José Martínez Casas

Ph.D. Enrique Nadal Soriano

Advised by: Prof. Francisco David Denia Guzmán

QUALIFYING TRIBUNAL

President: PhD _____

Vocal: PhD _____

Secretary: PhD _____

Valencia, July 2023

Abstract

Noise pollution has become a cause of major health problems, such as sleep, cardiovascular or cognitive alterations. In urban areas, the high values of transport and other human-activity-related noise can be especially harmful. This issue is a large subject of study, due to the broad nature of noise and its range of possible sources (and therefore the potential solutions to alleviate each of them). This Thesis focuses on the minimization of (i) exhaust system noise, which can be addressed by the use of mufflers (which in turn have other applications, such as in HVAC systems, i.e., heating, ventilation, and air conditioning), and (ii) general noise and vibration caused by transport, such as railway rolling noise, and the use of sound barriers to alleviate it.

On the one hand, mufflers (which can be divided into reactive, dissipative, and hybrid configurations) were long ago adopted in the exhaust line, but also the use of catalytic converters and diesel particulate filters has become spread, and, while their use responds to environmental rather than noise reduction reasons, they have an impact in the acoustic performance of the exhaust system. Diverse techniques for the modelling of sound propagation within ducts and the other aforementioned devices are reviewed, and several optimization schemes are proposed for the minimization of noise transmission. This includes (i) the sizing optimization of mufflers (including reactive and dissipative chambers), (ii) the topology optimization of the dissipative material (its density layout) within the dissipative chamber, and (iii) the sizing optimization of exhaust aftertreatment devices (catalytic converters and diesel particulate filters).

On the other hand, sound barriers have a wide range of applications, such as traffic noise barriers, train wheel fairings or even HVAC duct coatings. At this point, it is required to pair the acoustic and the elastic problems at the air-structure boundary to obtain the vibroacoustic problem. A hybrid displacement-pressure formulation is recalled here and applied to several case studies, in order to obtain acoustically-optimized elastic designs.

Resumen

La contaminación acústica se ha convertido en una causa de importantes problemas de salud, como alteraciones del sueño, cardiovasculares o cognitivas. En áreas urbanas, los altos valores del ruido debido al transporte y a otras actividades humanas pueden ser especialmente dañinos. Se trata de un tema de estudio abierto, debido a la amplia naturaleza del ruido y su gama de posibles fuentes (y, por lo tanto, las posibles soluciones para paliar cada una de ellas). Esta tesis se centra en la minimización del (i) ruido del sistema de escape, que puede abordarse mediante el uso de silenciadores (que a su vez tienen otras aplicaciones, como en los sistemas HVAC, es decir, calefacción, ventilación y aire acondicionado), así como del (ii) ruido y las vibraciones generales causados por el transporte, como por ejemplo el ruido de rodadura de los ferrocarriles, y el uso de barreras acústicas para mitigarlo.

Por un lado, los silenciadores (que se pueden dividir en configuraciones reactivas, disipativas e híbridas) fueron adoptados hace tiempo en la línea de escape, pero también se ha extendido el uso de convertidores catalíticos y filtros de partículas diésel, los cuales, si bien su uso responde a razones medioambientales más que de reducción del ruido, tienen un impacto en el rendimiento acústico del sistema de escape. En este punto, se revisan diversas técnicas para la simulación numérica de la propagación del sonido dentro de conductos y demás dispositivos mencionados, y se proponen varios esquemas de optimización para la minimización de la transmisión del ruido. Esto incluye (i) la optimización dimensional de los silenciadores (incluidas las cámaras reactivas y disipativas), (ii) la optimización topológica del material disipativo (su distribución de densidad) dentro de la cámara disipativa y (iii) la optimización dimensional de los dispositivos de postratamiento de escape (convertidores catalíticos y filtros de partículas diésel).

Por otro lado, el apantallamiento acústico tiene una amplia gama de aplicaciones, como las barreras acústicas de tráfico, carenados de ruedas de trenes o incluso revestimientos de conductos HVAC. En este punto, se requiere acoplar los problemas acústico y elástico en el contorno aire-estructura para obtener el problema vibroacústico. Aquí se plantea una formulación híbrida en des-

plazamiento-presión y se aplica a varios casos prácticos, con el fin de obtener diseños elásticos acústicamente optimizados.

Resum

La contaminació acústica s'ha convertit en una causa d'importants problemes de salut, com ara alteracions del son, cardiovasculars o cognitives. En àrees urbanes, els alts valors del soroll degut al transport i a altres activitats humanes poden ser especialment nocius. Es tracta d'un tema d'estudi obert, a causa de l'àmplia naturalesa del soroll i la gamma de possibles fonts (i, per tant, les possibles solucions per pal · liar cadascuna). Aquesta tesi se centra en la minimització del (i) soroll del sistema d'escapament, que es pot abordar mitjançant l'ús de silenciadors (que alhora tenen altres aplicacions, com en els sistemes HVAC, és a dir, calefacció, ventilació i aire condicionat), així com del (ii) soroll i les vibracions generals causats pel transport, com ara el soroll de rodament dels ferrocarrils, i l'ús de barreres acústiques per mitigar-lo.

D'una banda, els silenciadors (que es poden dividir en configuracions reactives, dissipatives i híbrides) van ser adoptats fa temps a la línia d'escapament, però també s'ha estès l'ús de convertidors catalítics i filtres de partícules dièsel, els quals, si bé el seu ús respon a raons mediambientals més que de reducció del soroll, tenen un impacte en el rendiment acústic del sistema d'escapament. En aquest punt, es revisen diverses tècniques per a la simulació numèrica de la propagació del so dins de conductes i altres dispositius esmentats, i es proposen diversos esquemes d'optimització per minimitzar la transmissió del soroll. Això inclou (i) l'optimització dimensional dels silenciadors (incloses les càmeres reactives i dissipatives), (ii) l'optimització topològica del material disipatiu (la distribució de densitat) dins de la càmera disipativa i (iii) l'optimització dimensional dels dispositius de posttractament d'escapament (convertidors catalítics i filtres de partícules dièsel).

D'altra banda, l'apantallament acústic té una àmplia gamma d'aplicacions, com ara les barreres acústiques de trànsit, carenats de rodes de trens o fins i tot revestiments de conductes HVAC. En aquest punt, cal acoblar els problemes acústic i elàstic al contorn aire-estructura per obtenir el problema vibroacústic. Aquí es planteja una formulació híbrida en desplaçament-pressió i s'aplica a diversos casos pràctics per obtenir dissenys elàstics acústicament optimitzats.

Contents

List of acronyms

Acronym	Meaning
ATO	Acoustic topology optimization
BEM	Boundary element method
BESO	Bi-directional evolutionary structural optimization
CC	Catalytic converter
CFD	Computational fluid dynamics
DPF	Diesel particulate filter
EA	Evolutionary algorithm
FE	Finite element
FEM	Finite element method
FSI	Fluid-structure interaction
GA	Genetic algorithm
HVAC	Heating, ventilation and air conditioning
KKT	Karush-Kuhn-Tucker
MM	Mode matching
MMM	Mode matching method
MMA	Method of moving asymptotes
RAMP	Rational approximation of material properties
SIMP	Solid isotropic material with penalization
TO	Topology optimization
TL	Trasnmission Loss

Chapter 1

Introduction

In this Chapter, the acoustic optimization problem is introduced, along with the main objectives of the present Thesis. The use of different numerical models and optimization approaches for each type of subproblem addressed in later chapters is justified for the sake of efficiency and computation speed. Finally, the general arrangement of the Thesis is explained.

1.1. Motivation and background

Transport-related noise, such as the one originated by automobiles and trains, is one of the major sources of environmental noise pollution [1]. Over the last decades, this problem has been a growing concern in highly populated areas, since prolonged exposure to noise has been related by the World Health Organization (WHO) to a higher likelihood of major health problems, such as sleep disturbance, cardiovascular disease or cognitive impairment in children [2].

Some of the main sources of automotive noise are: engine noise coming out through the exhaust line, the induction system, noise caused by accessories (cooling fan, etc.), and noise radiated by the engine [1]. This Thesis focuses on the acoustic modelling of the exhaust line, and special attention is given to mufflers (which can be split into reactive, dissipative and hybrid configurations, depending on the physical phenomena that take place primarily within their chambers). Regarding railway noise, its most important types are squeal (due to the wheel-rail stick-slip effect, especially during sharp curves), aerodynamic, and rolling noise (due to wheel-rail roughness, it results in a vibration-excitation of the wheel) [3]. Some examples of strategies to reduce the emissions of wheel rolling noise are the modification of the wheel's web geometry, the use of wheel perforations, and the use of viscoelastic coatings on the wheel [3–7].

Additionally, transport is related to a big share of the world's energy consumption [1]; in industrialized countries, it is linked to 25-30 % of the total greenhouse emissions. In addition to emitting CO2, internal combustion engines produce air pollutants such as unburned hydrocarbons (HC), carbon monoxide (CO), nitrogen oxides (NOx) or particulate matter (PM) [8]. The use of catalytic converters (CC) and diesel particulate filters (DPF) is widely spread in the automotive industry in order to alleviate this problem. These devices, located along the exhaust line, in turn have an impact on the exhaust noise.

In this context, the present Thesis explores the application of acoustic optimization schemes to several noise-absorbing devices, in combination with

efficient modelling algorithms, with the aim of obtaining optimized designs that minimize transport-related noise emissions.

1.2. Objectives

The present Thesis aims to obtain nontrivial optimized sound-absorbing designs with a view to reducing noise emissions within a range of acoustic and vibroacoustic applications, specifically, it addresses the acoustic topology optimization (ATO) of the following devices: reactive and dissipative (and hybrid) mufflers, aftertreatment devices such as catalytic converters and diesel particulate filters, and noise barriers such as wheel fairings and duct insulations. Such purpose is accomplished by the implementation of efficient acoustic finite element (FE) models, in combination with optimization schemes, such as the method of moving asymptotes (MMA) or genetic algorithms (GA). The following objectives are proposed:

(i) Implementation of FE models capable of solving the three-dimensional behaviour of axisymmetric dissipative and hybrid mufflers with non-homogeneous distributions of the absorbing material within the dissipative chamber, i.e., allowing for arbitrary position-dependent layouts of the material bulk's density. Additional working conditions under consideration include: presence of mean flow along the central duct, non-uniform temperature functions, etc.

(ii) Implementation of efficient analytical-numerical models for the evaluation of aftertreatment devices (such as CC and DPF) of arbitrary cross section. The numerical FE computation of the transversal pressure modes for the inlet/outlet ducts and chamber, combined with the mode matching technique for the longitudinal analysis, allows the inexpensive evaluation of the device's acoustic behaviour.

(iii) Development and implementation of efficient FE models capable of solving several vibroacoustic problems, by the combination of the versatile mixed displacement/pressure ($\mathbf{u}/p$) formulation (within the design domain), along with the standard pressure formulation (within the air domain).

(iv) Definition of objective functions $\mathcal{F}_0$ for the aforementioned problems (i – iii), and development of sensitivity analysis algorithms for the straightforward obtaining of the sensitivities of $\mathcal{F}_0$ with respect to the design variables.

(v) Implementation of topology optimization (TO) algorithms for the obtaining of nontrivial designs, concerning problems (i, iii). Additional consideration of lateral constraints, for example, by the use of the MMA.

(vi) Revision of the available two-material and three-material interpolation methods, e.g., the rational approximation of material properties (RAMP) or the solid isotropic material with penalization (SIMP), required for addressing the TO problem via a gradient-based algorithm.

(vii) Parametrization of different arbitrary cross section geometries (such as triangular, rectangular, etc.) for the analysis of atertreatment devices defined in (ii), and implementation of a GA to optimize certain parameters of CC and DPF (such as chamber lengths, monolith type, cross-sectional geometric parameters, etc.).

1.3. Organization and development of the Thesis

The Thesis is structured in seven different chapters. Aside from the present introduction, these are organized as follows:

- In Chapter 2, some fundamental concepts are presented concerning diverse fields such as: theory of sound propagation, the wave equation, the acoustics of ducts and mufflers and their FE modelling, the fluid-structure interaction problem, and the basics of structural shape optimization. A state-of-the-art literature review concerning the existing modelling techniques and optimization algorithms is performed, with a view to applying this ideas in the following chapters.

- In Chapter 3, an existing FE model is recalled for the acoustic simulation of axisymmetric dissipative and hybrid mufflers with non-uniform bulk density distributions of the absorbing material. Next, an ATO problem

is set up with the aim of finding optimized designs that increase the muffler's mean transmission loss (TL) within a desired frequency range. For this purpose, each element of the dissipative chamber is assigned a variable v_j, which denotes the fibre's local bulk density which, in turn, has an influence on the sound propagation properties of the medium within the element's domain. Next, a scheme for the computing of the sensitivities of the TL with respect all design variables is defined. Some lateral constraints (such as the maximum allowed amount of dissipative fibre) are added. Finally, three case studies, with different working conditions and optimization frequency ranges, are performed, and results are discussed.

- In Chapter 4, an existing multidimensional technique for the evaluation of the acoustic behaviour of aftertreatment devices (CC and DPF) is recalled. The mode-matching method allows for longitudinally uniform, arbitrary cross sections of the chamber being studied, and therefore, a tool is developed here for the generation and meshing of any chamber geometry and location of the inlet and outlet ducts. The monolith present within the chamber is replaced in this work by a four-pole transfer matrix, by using the analytical models presented in Chapter 2. Due to the low number of design variables, a GA is set up to carry out the optimization process, enabling a global search of design solutions. Finally, optimal designs of CC and DPF are obtained for different target frequency ranges and results are discussed.

- In Chapter 5, the computationally costly but versatile $\mathbf{u}/p$ formulation presented in Chapter 2 is combined with the standard pressure formulation, in order to address 2D vibroacoustic problems. Three different case studies are generated, by including a noise source, a design region (which is meshed with u/p elements) and a distant absorbing boundary, where the noise emission is to be minimized. A software is implemented in order to allow for designs containing air, solid and porous materials. Next, a three-material interpolation scheme with two variables per element is set up in order to allow the vibroacoustic properties of the elements within the design region to range from those of the air to those of the elastic solid or the porous absorbing materials. In a similar way to Chapter 3, the adjoint method is used to obtain the sensitivities of $\mathcal{F}_0$ with respect to each v_j. Finally, the optimization results are shown and discussed.

- In Chapter 6, the main conclusions are withdrawn from the presented work, and possible future works following the current line of research are proposed and briefly discussed.
- In Chapter 7, the major contributions derived from the context of the present Thesis are detailed, including journal papers, as well as national and international conference works.

Chapter 2

Fundamentals: modelling of acoustic problems and optimization techniques

In this Chapter, a literature review is carried out on diverse topics such as the fundamentals of sound propagation, addressing different topics such as the acoustics of ducts and mufflers, and the acoustic characterization of several absorbent materials, perforated surfaces and monoliths. Next, the principles of vibroacoustics are presented, and a mixed $\boldsymbol{u}/p$ formulation is introduced, allowing to solve the topology optimization problem. Finally, a revision of the existing shape and topology optimization methods is performed.

2.1. The acoustic problem

2.1.1. Introduction

Sound propagation can be modelled by the corresponding mathematical equations [9–11], of higher or lower complexity, depending on the number and nature of the conveniently verified simplifying hypotheses. The solution obtained will model temporal and spatial distributions of acoustic variables such as pressure, velocity, density, etc.

In this Section, some physical models are recalled, regarding the modelling of the acoustic problem. First, the general sound propagation equations are introduced, and the corresponding simplifications are made in Section 2.1.3.

2.1.2. Models for the acoustic calculation

Several acoustic models can be taken into account in order to address the acoustic problem [12, 13]. First, the nonlinear fluid dynamic model is presented. Second, the linear acoustic model (considered throughout this Thesis) is introduced.

2.1.2.1. Dynamic model

The solving of a general fluid dynamic problem requires the study of three equations simultaneously:

- Continuity equation (2.1).
- Dynamic equilibrium equation (2.3–2.5).
- Energy equation (2.7).

Furthermore, three additional equations are also necessary, these are the state equation, the internal energy equation and a viscosity model, in order to evaluate the relationship among pressure, density, temperature, fluid velocity, viscosity and internal energy.

First, the continuity equation is fulfilled by any fluid which satisfies the law of conservation of mass, i.e., the difference between the mass entering and leaving any arbitrary volume equals the change of its corresponding mass. It can be stated locally as [14]:

$$\frac{\partial \rho}{\partial t} + \frac{\partial}{\partial x}(\rho u) + \frac{\partial}{\partial y}(\rho v) + \frac{\partial}{\partial z}(\rho w) = 0 \ , \tag{2.1}$$

or in the corresponding vector form:

$$\frac{\partial \rho}{\partial t} + \nabla^T (\rho \mathbf{u}) = 0 \ , \tag{2.2}$$

where the velocity vector $\mathbf{u}$ contains the three components u, v and w; while ρ and t denote density and time, and ∇^T is the divergence operator. Secondly, the dynamic equilibrium equation for a Newtonian fluid [14] can be stated as:

$$\begin{aligned} \rho a_x = \rho B_x - \frac{\partial p}{\partial x} &+ \frac{\partial}{\partial x}\left(2\mu \frac{\partial u}{\partial x} + \left(\zeta - \frac{2}{3}\mu\right)\nabla^T \mathbf{u}\right) \\ &+ \frac{\partial}{\partial y}\left(\mu\left(\frac{\partial u}{\partial y} + \frac{\partial v}{\partial x}\right)\right) + \frac{\partial}{\partial z}\left(\mu\left(\frac{\partial u}{\partial z} + \frac{\partial w}{\partial x}\right)\right) \end{aligned} \ , \tag{2.3}$$

$$\begin{aligned} \rho a_y = \rho B_y - \frac{\partial p}{\partial y} &+ \frac{\partial}{\partial y}\left(2\mu \frac{\partial v}{\partial y} + \left(\zeta - \frac{2}{3}\mu\right)\nabla^T \mathbf{u}\right) \\ &+ \frac{\partial}{\partial z}\left(\mu\left(\frac{\partial v}{\partial z} + \frac{\partial w}{\partial y}\right)\right) + \frac{\partial}{\partial x}\left(\mu\left(\frac{\partial v}{\partial x} + \frac{\partial u}{\partial y}\right)\right) \end{aligned} \ , \tag{2.4}$$

$$\begin{aligned} \rho a_z = \rho B_z - \frac{\partial p}{\partial z} &+ \frac{\partial}{\partial z}\left(2\mu \frac{\partial w}{\partial z} + \left(\zeta - \frac{2}{3}\mu\right)\nabla^T \mathbf{u}\right) \\ &+ \frac{\partial}{\partial x}\left(\mu\left(\frac{\partial w}{\partial x} + \frac{\partial u}{\partial z}\right)\right) + \frac{\partial}{\partial y}\left(\mu\left(\frac{\partial w}{\partial y} + \frac{\partial v}{\partial z}\right)\right) \end{aligned} \ , \tag{2.5}$$

where ρB_x, ρB_y and ρB_z denote the volumetric forces, p is the pressure, μ refers to the dynamic viscosity and ζ is the second viscosity coefficient (which for monoatomic gases is null). Components of acceleration $\mathbf{a}$ are defined as $a_x = Du/Dt$, $a_y = Dv/Dt$ and $a_z = Dw/Dt$; and D/Dt refers to the total time derivative:

$$\frac{D}{Dt} = \frac{\partial}{\partial t} + u\frac{\partial}{\partial x} + v\frac{\partial}{\partial y} + w\frac{\partial}{\partial z} \ . \tag{2.6}$$

For non-isothermal flows with a temperature-dependant viscosity, the continuity and dynamic equilibrium equations are coupled with the equation of

energy. The latter can be expressed in the following form:

$$\begin{aligned}&\frac{\partial}{\partial x}\left(\kappa\frac{\partial T}{\partial x}\right)+\frac{\partial}{\partial y}\left(\kappa\frac{\partial T}{\partial y}\right)+\frac{\partial}{\partial z}\left(\kappa\frac{\partial T}{\partial z}\right)+\frac{\partial Q}{\partial t}+\Phi_d-\nabla^T\mathbf{q}_r\\&=\frac{\partial}{\partial x}(pu)+\frac{\partial}{\partial y}(pv)+\frac{\partial}{\partial z}(pw)+\frac{\rho}{2}\frac{D}{Dt}\left(u^2+v^2+w^2\right)+\rho\frac{DE}{Dt}\ ,\end{aligned}\tag{2.7}$$

and expresses equilibrium among incoming, outgoing and accumulated energy. κ denotes the thermal conductivity, T the temperature, Q is the generated heat per unit volume, $\mathbf{q}_r$ the vector of heat radiation flux, E the internal energy and Φ_d refers to the heat dissipation function, expressed by Eq. (2.8):

$$\begin{aligned}\Phi_d=\lambda\left(\frac{\partial u}{\partial x}+\frac{\partial v}{\partial y}+\frac{\partial w}{\partial z}\right)^2+2\mu\left(\left(\frac{\partial u}{\partial x}\right)^2+\left(\frac{\partial v}{\partial y}\right)^2+\left(\frac{\partial w}{\partial z}\right)^2\right)\\+\mu\left(\left(\frac{\partial w}{\partial y}+\frac{\partial v}{\partial z}\right)^2+\left(\frac{\partial u}{\partial z}+\frac{\partial w}{\partial x}\right)^2+\left(\frac{\partial v}{\partial x}+\frac{\partial u}{\partial y}\right)^2\right)\ ,\end{aligned}\tag{2.8}$$

where $\lambda=\zeta-2/3\mu$. The three aforementioned additional equations [14] (equation of state, and the internal energy and the viscosity equations) can be stated in general form as:

$$\rho=\rho(p,T)\ ,\tag{2.9}$$

$$E=E(p,T)\ ,\tag{2.10}$$

$$\mu=\mu(p,T)\ .\tag{2.11}$$

Therefore, the solving of a general flow problem requires obtaining the velocity field $\mathbf{u}$, density ρ, internal energy E, pressure p, temperature T, and viscosity μ, given a domain and corresponding boundary and initial conditions, by solving eight equations. This System (2.1, 2.3–2.5, 2.7, 2.9–2.11) can be of high complexity since the acting forces and temperature can deform the domain boundary yielding to a fully coupled nonlinear fluid-structure interaction (FSI) problem.

2.1.2.2. Linear acoustic model

The linear acoustic model takes its name from the assumed hypotheses made in order to derive the wave equation (called Helmholtz equation in the harmonic case) [13] resulting from linearizing the continuity, dynamic equilibrium and constitutive equations. This linearization assumes that the increments of density and pressure of the particles are small with respect to their

mean or equilibrium values. It seems evident that the range of application of this equation is restricted to acoustic phenomena of low amplitude, such as those present within the mufflers and catalytic converters, where the excitation does not usually exceed 140 dB [15, 16].

2.1.3. Wave equation

The mathematical deduction of the liniarized wave equation is carried out in this Section, due to its importance in this Thesis. With the aim of simplifying the nomenclature, total variables are denoted hereinafter by subscript T, whereas subscript 0 refers to average values. Variables related to the acoustic perturbation used in order to carry out the linearization are denoted with no subscript. First, the initial hypotheses considered to derive the linearized wave equation are named:

- The acoustic wave propagates across an ideal fluid (with no viscosity), more specifically an ideal gas.
- Wave propagation is considered to be adiabatic. Entropy of the fluid particles remains almost invariable, since the thermal energy exchange among them is considered to be small. In fact, the temperature of a fluid increases during the process of compression, and decreases during its expansion. Hence the propagation of a sound wave would produce a longitudinal heat transfer from a condensation to a nearby rarefaction, located half a wavelength $\lambda/2$ away. The amount of heat transmitted depends on the thermal conductivity of the fluid. Audible frequencies (20 Hz – 20 kHz) have a wavelength λ that is too large, and a sufficiently low thermal conductivity to produce appreciable heat transfer, and the aforementioned process is hence considered adiabatic [17]. Along with the previous hypotheses, this leads to the process being considered isoentropic, satisfying:
$$p_T = C\rho_T^{\gamma} \ , \tag{2.12}$$
γ being the adiabatic coefficient or ratio of specific heat capacities (at constant-pressure to constant volume) [17, 18].
- As aforementioned, small fluctuations of pressure, density and particle velocity are assumed, what enables the problem to be liniarized by adding small acoustic amplitudes to the average pressure, density and

velocity:

$$\rho_T = \rho_0 + \rho \ , \tag{2.13}$$
$$p_T = p_0 + p \ , \tag{2.14}$$
$$\mathbf{u}_T = \mathbf{u}_0 + \mathbf{u} \ . \tag{2.15}$$

For the moving medium, this results in the convective wave equation. On the contrary, particles only present a vibratory motion around their equilibrium point in a non-moving medium [19].

The ideal fluid hypothesis implies that no viscosity effects are taken into consideration. The Navier-Stokes equations (2.3–2.5) can be expressed here as:

$$\begin{aligned} \rho_T \frac{Du_T}{Dt} &= \rho_T B_x - \frac{\partial p_T}{\partial x} \ , \\ \rho_T \frac{Dv_T}{Dt} &= \rho_T B_y - \frac{\partial p_T}{\partial y} \ , \\ \rho_T \frac{Dw_T}{Dt} &= \rho_T B_z - \frac{\partial p_T}{\partial z} \ , \end{aligned} \tag{2.16}$$

also known as Euler equations. In vector form these lead to:

$$\rho_T \frac{D\mathbf{u}}{Dt} = \rho_T \mathbf{B} - \nabla p_T \ . \tag{2.17}$$

From certain thermodynamic considerations [9], it can be deduced that:

$$\frac{Dp_T}{Dt} = c_0^2 \frac{D\rho_T}{Dt} \ , \tag{2.18}$$

where the speed of sound in the air is given by:

$$c_0^2 = \left(\frac{\partial p_T}{\partial \rho_T} \right)_s \ , \tag{2.19}$$

where subscript s denotes derivative at constant entropy. For an ideal gas, and taking into account Eqs. (2.12) and (2.19), it yields:

$$c_0^2 = \left(\frac{\partial p_T}{\partial \rho_T} \right)_s = \frac{\gamma \left(p_0 + p \right)}{\rho_0 + \rho} \approx \frac{\gamma p_0}{\rho_0} \ . \tag{2.20}$$

Applying the definition of total derivative (2.6) to the continuity equation (2.1) yields:

$$\frac{D\rho_T}{Dt} + \rho_T \nabla^T \mathbf{u}_T = 0 \ , \tag{2.21}$$

and by merging Equations (2.18) and (2.21) it is obtained:

$$\frac{Dp_T}{Dt} + \rho_T c_0^2 \nabla^T \mathbf{u}_T = 0 \ . \tag{2.22}$$

By differentiating with respect to time, one obtains:

$$\frac{D^2 p_T}{Dt^2} + \frac{D}{Dt}\left(\rho_T c_0^2 \nabla^T \mathbf{u}_T\right) = 0 \ . \tag{2.23}$$

On the other side, after neglecting gravitatory effects, Euler's equation (2.17) turns into:

$$\rho_T \frac{D\mathbf{u}}{Dt} = -\nabla p_T \ . \tag{2.24}$$

The linear equations that describe the acoustic perturbations are obtained by using the first-order terms of the initial nonlinear equations. Zeroth-order terms are not included, since ambient values of the variables correspond to a valid state of the system. For Equation (2.24), it is satisfied that:

$$\begin{aligned}
\rho_0\left(u_0\frac{\partial u_0}{\partial x} + v_0\frac{\partial u_0}{\partial y} + w_0\frac{\partial u_0}{\partial z}\right) + \frac{\partial p_0}{\partial x} = 0 \ , \\
\rho_0\left(u_0\frac{\partial v_0}{\partial x} + v_0\frac{\partial v_0}{\partial y} + w_0\frac{\partial v_0}{\partial z}\right) + \frac{\partial p_0}{\partial y} = 0 \ , \\
\rho_0\left(u_0\frac{\partial w_0}{\partial x} + v_0\frac{\partial w_0}{\partial y} + w_0\frac{\partial w_0}{\partial z}\right) + \frac{\partial p_0}{\partial z} = 0 \ ,
\end{aligned} \tag{2.25}$$

whose integration leads to the steady-flow Bernoulli equation [20].

2.1.3.1. Non-moving medium

In this case, $\mathbf{u}_0$ is null and therefore $\mathbf{u}_T = \mathbf{u}$ (see Eq. (2.15)). According to Expression (2.25), it is derived that $\nabla p_0 = 0$, and linearization of Equation (2.22) yields:

$$\frac{\partial p}{\partial t} + \rho_0 c_0^2 \nabla^T \mathbf{u} = 0 \ , \tag{2.26}$$

and Eq. (2.24) leads to:

$$\rho_0 \frac{\partial \mathbf{u}}{\partial t} = -\nabla p \ . \tag{2.27}$$

By differentiating Eq. (2.26) with respect to time, taking ∇^T of Eq. (2.27), and finally combining both, the wave equation for non-moving medium is obtained:

$$\boxed{\rho_0 \nabla\left(\frac{1}{\rho_0}\nabla p\right) - \frac{1}{c_0^2}\frac{\partial^2 p}{\partial t^2} = 0 \ ,} \tag{2.28}$$

where it is assumed that c_0 and ρ_0 are time-independent. Additionally, for spatially homogeneous propagation properties in the medium, it yields:

$$\nabla^2 p - \frac{1}{c_0^2}\frac{\partial^2 p}{\partial t^2} = 0 \ . \tag{2.29}$$

By assuming a harmonic solution $p = Pe^{j\omega t}$, the Helmholtz equation is obtained:

$$\nabla^2 P + k_0^2 P = 0 \ , \tag{2.30}$$

$k_0 = \omega/c_0$ being the wavenumber, P the spatially dependent complex acoustic pressure amplitude, $\omega = 2\pi f$ the angular frequency and j the imaginary unit. Equations (2.28–2.30) are of great importance and have been used throughout this Thesis.

2.1.3.2. Moving medium

For stationary flows, with position-independent ρ_0 and c_0, the convective wave equation can be deduced from Eqs. (2.23–2.25) [19]:

$$\begin{aligned}\nabla^2 p - \frac{1}{c_0^2}\frac{D^2 p}{Dt^2} + 2\rho_0 \Bigg(&\frac{\partial u_0}{\partial x}\frac{\partial u}{\partial x} + \frac{\partial v_0}{\partial x}\frac{\partial u}{\partial y} + \frac{\partial w_0}{\partial x}\frac{\partial u}{\partial z} \\ &+ \frac{\partial u_0}{\partial y}\frac{\partial v}{\partial x} + \frac{\partial v_0}{\partial y}\frac{\partial v}{\partial y} + \frac{\partial w_0}{\partial y}\frac{\partial v}{\partial z} + \frac{\partial u_0}{\partial z}\frac{\partial w}{\partial x} + \frac{\partial v_0}{\partial z}\frac{\partial w}{\partial y} + \frac{\partial w_0}{\partial z}\frac{\partial w}{\partial z}\Bigg) = 0 \ ,\end{aligned} \tag{2.31}$$

or in compact form:

$$\nabla^2 p - \frac{1}{c_0^2}\frac{D^2 p}{Dt^2} + 2\rho_0 \sum_{i=1}^{3}\sum_{j=1}^{3} \frac{\partial u_{0j}}{\partial x_i}\frac{\partial u_i}{\partial x_j} = 0 \ , \tag{2.32}$$

where $\nabla^2 = \partial^2/\partial x^2 + \partial^2/\partial y^2 + \partial^2/\partial z^2$ is the Laplace operator, and $x_1 = x$, $x_2 = y$, $x_3 = z$, $u_1 = u$, $u_2 = v$, $u_3 = w$, $u_{01} = u_0$, $u_{02} = v_0$ and $u_{03} = w_0$. For uniform (non-spatially dependent) steady flows with mean flow velocity $\mathbf{u}_0$, it yields [13]:

$$\nabla^2 p - \frac{1}{c_0^2}\frac{D^2 p}{Dt^2} = 0 \ , \tag{2.33}$$

the total time derivative being defined here in the following terms:

$$\frac{D}{Dt} = \frac{\partial}{\partial t} + u_0\frac{\partial}{\partial x} + v_0\frac{\partial}{\partial y} + w_0\frac{\partial}{\partial z} \ . \tag{2.34}$$

Equation (2.33) has been used throughout the actual Thesis in order to obtain the acoustic field within areas with uniform mean flow. However, for spatially non-uniform $\mathbf{u}_0$, an approach based on the acoustic velocity potential function ϕ [19, 21] can be used in order to simplify Expression (2.32). By defining ϕ so that $\mathbf{u} = \nabla\phi$, it is obtained:

$$\nabla^2\phi - \frac{1}{c_0^2}\frac{D^2\phi}{Dt^2} = 0 \ , \tag{2.35}$$

where ϕ can be also defined as [13]:

$$p = -\rho_0\frac{D\phi}{Dt} \ . \tag{2.36}$$

The mean flow velocity can be derived from the mean flow velocity potential ϕ_0, which satisfies the Laplace equation:

$$\nabla^2\phi_0 = 0 \ , \tag{2.37}$$

following the relation $\mathbf{u}_0 = \nabla\phi_0$. On the other hand, if ρ_0 and c_0 vary with position, the appropriate form of Equation (2.35) is [19]:

$$\boxed{\frac{1}{\rho_0}\nabla\left(\rho_0\nabla\phi\right) - \frac{D}{Dt}\left(\frac{1}{c_0^2}\frac{D\phi}{Dt}\right) = 0 \ .} \tag{2.38}$$

Equations (2.35) and (2.38) are of great importance and will be used throughout the present Thesis.

2.1.4. One-dimensional acoustics of ducts

One of the most elementary applications of the previously derived wave equations (see Section 2.1.3) is the unidimensional propagation which originates the traditional plane wave models [13, 22–27].

2.1.4.1. Non-moving medium

Starting from the Helmholtz equation (2.30), a rigid-wall duct is supposed, whose axis is parallel to axis z. By assuming that the solution is only a function of z (plane wave), it is obtained:

$$\frac{\partial^2 P}{\partial z^2} + k_0^2 P = 0 \ , \tag{2.39}$$

which is valid for a homogeneous propagating medium, and its solution can be expressed as:

$$P(z) = P^{+}e^{-jk_0 z} + P^{-}e^{jk_0 z} \ , \tag{2.40}$$

P^{+} and P^{-} being the associated amplitudes to the progressive and regressive waves, respectively. Analogously, Euler's equation (2.24) yields:

$$U(z) = \frac{-1}{j\rho_0\omega}\frac{\partial P(z)}{\partial z} = \frac{1}{Z_0}\left(P^{+}e^{-jk_0 z} - P^{-}e^{jk_0 z}\right) \ , \tag{2.41}$$

where $Z_0 = \rho_0 c_0$ is the characteristic impedance of the air. Additionally, the second acoustic variable, i.e., the mass flow V can be defined for a duct with cross-sectional area S, as:

$$V(z) = \rho_0 S U = \frac{1}{Y_0}\left(P^{+}e^{-jk_0 z} - P^{-}e^{jk_0 z}\right) \ , \tag{2.42}$$

$Y_0 = c_0/S$ being the characteristic impedance of the duct. Coefficients P^{+} and P^{-} are solved by taking into account the corresponding boundary conditions applied at the duct (see Section 2.1.5).

2.1.4.2. Moving medium

For the case of a moving medium, a rigid-walled duct is considered, as well as a one-dimensional uniform flow with speed U_{mf}. The relative speed of sound with respect to the moving medium is still c_0, and therefore the propagation speed of the progressive and regressive waves are respectively $U_{mf} + c_0$ and $U_{mf} - c_0$ due to the convective effect. The one-dimensional form of Equation (2.33) can be written as:

$$\frac{\partial^2 p}{\partial z^2} - \frac{1}{c_0^2}\frac{D^2 p}{Dt^2} = 0 \ , \tag{2.43}$$

where the total derivative is:

$$\frac{D}{Dt} = \frac{\partial}{\partial t} + U_{mf}\frac{\partial}{\partial z} \ , \tag{2.44}$$

and by combining Eqs. (2.43) and (2.44), it is obtained:

$$\left(1 - M_{mf}^2\right)\frac{\partial^2 p}{\partial z^2} - 2\frac{M_{mf}}{c_0}\frac{\partial^2 p}{\partial z \partial t} - \frac{1}{c_0^2}\frac{\partial^2 p}{\partial t^2} = 0 \ , \tag{2.45}$$

$M_{mf} = U_{mf}/c_0$ being the Mach number of the mean flow. The harmonic form of Eq. (2.45) is:

$$\left(1 - M_{mf}^2\right) \frac{\partial^2 P}{\partial z^2} - 2jk_0 M_{mf} \frac{\partial P}{\partial z} + k_0^2 P = 0 \ , \tag{2.46}$$

and the corresponding solution can be expressed as:

$$P\left(z\right) = P^+ e^{\frac{-jk_0 z}{1+M_{mf}}} + P^- e^{\frac{jk_0 z}{1-M_{mf}}} \ . \tag{2.47}$$

Euler's equation (2.27) can be rewritten, for the one-dimensional case, as:

$$\rho_0 \left(j\omega U + U_{mf} \frac{\partial U}{\partial z}\right) = -\frac{\partial P}{\partial z} \ , \tag{2.48}$$

and expressions for the acoustic velocity and mass flow can be built analogously to the previous case:

$$U\left(z\right) = \frac{1}{Z_0} \left(P^+ e^{\frac{-jk_0 z}{1+M_{mf}}} - P^- e^{\frac{jk_0 z}{1-M_{mf}}}\right) \ , \tag{2.49}$$

$$V\left(z\right) = \frac{1}{Y_0} \left(P^+ e^{\frac{-jk_0 z}{1+M_{mf}}} - P^- e^{\frac{jk_0 z}{1-M_{mf}}}\right) \ , \tag{2.50}$$

where the medium and duct impedances are defined previously for the case of non-moving medium (see Eqs. (2.41) and (2.42)).

2.1.5. Plane wave models. Matrix representations

The global acoustic performance of an exhaust system depends on its working conditions, the noise source and outlet type, as well as the acoustic contribution of each device included in the exhaust line. With the aim of studying the global acoustic performance of the exhaust line, a matrix method has been applied in this Thesis, which facilitates the definition of each device in an isolated manner.

In this way, a complex system can be decomposed into different subelements. The global response is hence given, by combining the four-pole matrices [13,28] corresponding to all devices involved. This philosophy can be applied both to mufflers, as well as to aftertreatment devices (such as catalytic converters and diesel particulate filters).

2.1.5.1. Generalities

Figure 2.1 shows a simplified scheme of an exhaust system, which consists of a noise source (engine), and two elements connected downstream: a muffler and a catalytic converter [17].

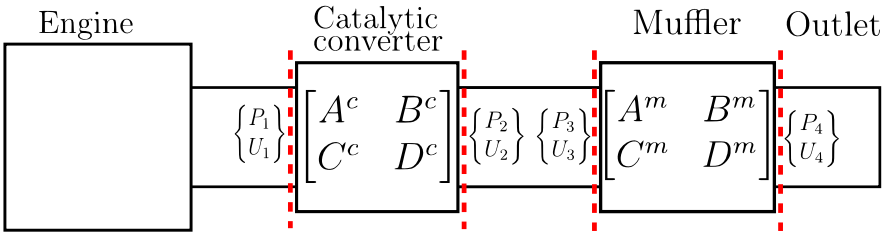

Figure 2.1: Scheme of an exhaust line.

The interest variables to be considered at the inlet and outlet of each element are usually the acoustic pressure and velocity. For the CC, this can be expressed as:

$$\begin{Bmatrix} P_1 \\ U_1 \end{Bmatrix} = \begin{bmatrix} A^c & B^c \\ C^c & D^c \end{bmatrix} \begin{Bmatrix} P_2 \\ U_2 \end{Bmatrix} = \mathbf{T} \begin{Bmatrix} P_2 \\ U_2 \end{Bmatrix} \; . \tag{2.51}$$

This means that the acoustic perturbation at duct 1, defined by the state vector $\{P_1, U_1\}^T$, can be expressed by the perturbation at a point located downstream $\{P_2, U_2\}^T$, and the transfer matrix $\mathbf{T}$ relative to the element that links 1 and 2, provided that plane wave propagation occurs at both points 1 and 2.

The evaluation of the four poles of the transfer matrix must be carried out by applying the appropiate boundary conditions to the acoustic system. From Eq. (2.51), it is obtained:

$$A^c = \left.\frac{P_1}{P_2}\right|_{U_2=0} \; , \quad B^c = \left.\frac{P_1}{U_2}\right|_{P_2=0} \; , \quad C^c = \left.\frac{U_1}{P_2}\right|_{U_2=0} \; , \quad D^c = \left.\frac{U_1}{U_2}\right|_{P_2=0} \; , \tag{2.52}$$

where the boundary condition $P_2 = 0$ refers to an open end at the outlet, and $U_2 = 0$ refers to a rigid wall (closed duct). Both expressions can be used with ease during the analytical or experimental obtaining of the transfer matrix.

2.1.5.2. Transfer matrix of a duct

In this Section, the tranfer matrix of a duct of length L and cross section S (see Figure 2.2), is obtained. Acoustic pressure and velocity are given by:

$$P(z) = P^{+}e^{-jk_0 z} + P^{-}e^{jk_0 z} \ , \tag{2.53}$$

$$U(z) = \frac{1}{Z_0}\left(P^{+}e^{-jk_0 z} - P^{-}e^{jk_0 z}\right) \ . \tag{2.54}$$

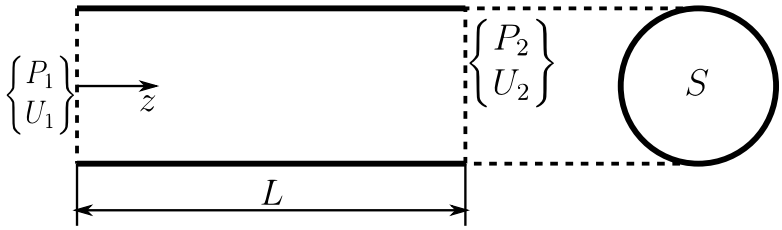

Figure 2.2: Constant cross section duct.

According to (2.52), two analyses must be performed, each one with different boundary conditions. To start with, a closed duct termination $U_2 = 0$ and an arbitrary unitary pressure $P_1 = 1$ at the inlet are imposed. This leads to:

$$P(z=0) = P_1 = P^{+} + P^{-} = 1 \ , \tag{2.55}$$

$$U(z=L) = U_2 = \frac{1}{Z_0}\left(P^{+}e^{-jk_0 L} - P^{-}e^{jk_0 L}\right) = 0 \ . \tag{2.56}$$

The solution to the previous system can be written as:

$$P^{+} = \frac{1}{2}\frac{\cos(k_0 L) + j\sin(k_0 L)}{\cos(k_0 L)} \ , \tag{2.57}$$

$$P^{-} = \frac{1}{2}\frac{\cos(k_0 L) - j\sin(k_0 L)}{\cos(k_0 L)} \ , \tag{2.58}$$

and therefore terms A and C of the transfer matrix (defined in Eq. (2.52)) are:

$$A = \left.\frac{P_1}{P_2}\right|_{U_2=0} = \cos(k_0 L) \ , \tag{2.59}$$

$$C = \left.\frac{U_1}{P_2}\right|_{U_2=0} = \frac{j}{Z_0}\sin(k_0 L) \ . \tag{2.60}$$

With a view to obtaining terms B and D, P_2 is set to zero, which leads to:

$$P(z=0) = P_1 = P^+ + P^- = 1 \ , \tag{2.61}$$

$$P(z=L) = P_2 = P^+ e^{-jk_0L} + P^- e^{jk_0L} = 0 \ , \tag{2.62}$$

solving for P^+ and P^- gives:

$$P^+ = \frac{-j}{2} \frac{\cos(k_0L) + j\sin(k_0L)}{\sin(k_0L)} \ , \tag{2.63}$$

$$P^- = \frac{1}{2} \frac{\sin(k_0L) + j\cos(k_0L)}{\sin(k_0L)} \ , \tag{2.64}$$

and the remaining terms are:

$$B = \left.\frac{P_1}{U_2}\right|_{P_2=0} = jZ_0 \sin(k_0L) \ , \tag{2.65}$$

$$D = \left.\frac{U_1}{U_2}\right|_{P_2=0} = \cos(k_0L) \ . \tag{2.66}$$

By joining Eqs. (2.51, 2.59–2.60, 2.65–2.66), it is obtained:

$$\begin{Bmatrix} P_1 \\ U_1 \end{Bmatrix} = \begin{bmatrix} \cos(k_0L) & jZ_0\sin(k_0L) \\ \dfrac{j}{Z_0}\sin(k_0L) & \cos(k_0L) \end{bmatrix} \begin{Bmatrix} P_2 \\ U_2 \end{Bmatrix} \ . \tag{2.67}$$

In a similar form, previous Eq. (2.67) can be expressed by means of pressure and mass flow as:

$$\begin{Bmatrix} P_1 \\ V_1 \end{Bmatrix} = \begin{bmatrix} \cos(k_0L) & jY_0\sin(k_0L) \\ \dfrac{j}{Y_0}\sin(k_0L) & \cos(k_0L) \end{bmatrix} \begin{Bmatrix} P_2 \\ V_2 \end{Bmatrix} \ . \tag{2.68}$$

In case of considering a uniform mean flow along the duct, the same procedure can be applied to Eqs. (2.47) and (2.49) [13], obtaining:

$$\begin{Bmatrix} P_1 \\ U_1 \end{Bmatrix} = e^{-jM_{mf}\frac{k_0}{1-M_{mf}^2}L} \begin{bmatrix} \cos\left(\dfrac{k_0}{1-M_{mf}^2}L\right) & jZ_0\sin\left(\dfrac{k_0}{1-M_{mf}^2}L\right) \\ \dfrac{j}{Z_0}\sin\left(\dfrac{k_0}{1-M_{mf}^2}L\right) & \cos\left(\dfrac{k_0}{1-M_{mf}^2}L\right) \end{bmatrix} \begin{Bmatrix} P_2 \\ U_2 \end{Bmatrix} \ . \tag{2.69}$$

2.1.5.3. Transfer matrix at expansions and contractions

Figure 2.3 shows the sketch of two unions of ducts with different cross sections: a tube expansion ($S_2 > S_1$) and a contraction ($S_2 < S_1$). As aforementioned, these form the basis for the functioning of reactive mufflers [13].

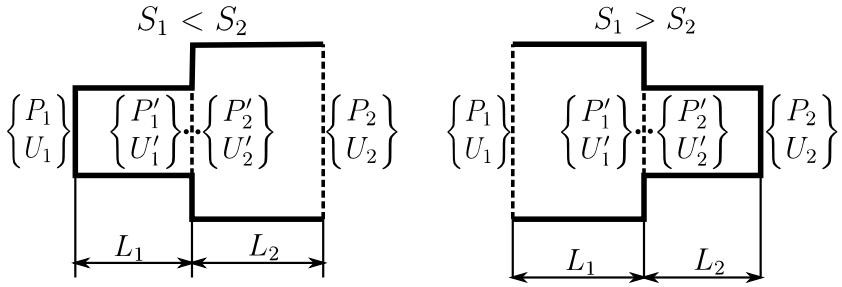

Figure 2.3: Duct expansion (left) and contraction (right).

With a view to obtaining the four-pole transfer matrix of the aforementioned cross section changes, a similar approach to the one described in Section 2.1.5.2 is followed. In absence of mean flow, pressure and mass flow do not change at both sides of the geometric discontinuity:

$$P_1' = P_2' \ , \tag{2.70}$$

$$\rho_0 S_1 U_1' = \rho_0 S_2 U_2' \ . \tag{2.71}$$

This can be expressed in matrix form as:

$$\begin{Bmatrix} P_1' \\ U_1' \end{Bmatrix} = \begin{bmatrix} 1 & 0 \\ 0 & \dfrac{S_2}{S_1} \end{bmatrix} \begin{Bmatrix} P_2' \\ U_2' \end{Bmatrix} \ , \tag{2.72}$$

$$\begin{Bmatrix} P_1' \\ V_1' \end{Bmatrix} = \begin{bmatrix} 1 & 0 \\ 0 & 1 \end{bmatrix} \begin{Bmatrix} P_2' \\ V_2' \end{Bmatrix} \ . \tag{2.73}$$

Equations (2.72) and (2.73) are of wide use for the matrix modelling of exhaust lines, since these normally contain several cross section changes. However, velocity fields must be continuous at the section change, and hence some multidimensional effects appear [29–31]. This effect is specially relevant at high frequencies, and therefore the afore introduced matrices are only valid in the low frequency range.

Finally, once the four-pole transfer matrix of the cross section change is known, the relation between the acoustic variables at planes 1 and 2 in Figure 2.3 can be built:

$$\begin{Bmatrix} P_1 \\ U_1 \end{Bmatrix} = \begin{bmatrix} \cos(k_0 L_1) & jZ_0 \sin(k_0 L_1) \\ \dfrac{j}{Z_0} \sin(k_0 L_1) & \cos(k_0 L_1) \end{bmatrix} \begin{bmatrix} 1 & 0 \\ 0 & \dfrac{S_2}{S_1} \end{bmatrix} \begin{bmatrix} \cos(k_0 L_2) & jZ_0 \sin(k_0 L_2) \\ \dfrac{j}{Z_0} \sin(k_0 L_2) & \cos(k_0 L_2) \end{bmatrix} \begin{Bmatrix} P_2 \\ U_2 \end{Bmatrix}. \tag{2.74}$$

2.2. The fluid-structure interaction problem

Chapter 5 of the present Thesis deals with the application of TO algorithms to the FSI problem, with the aim of reducing noise emissions in diverse problems. Hence, the basic principles of this kind of multi-physics problem are introduced below.

Figure 2.4 shows the set-up of a typical vibroacoustic problem, consisting of an elastic screen placed between an acoustic source and a receiver located at $\mathbf{P}_S$ and $\mathbf{P}_R$ respectively. The domain is split into the air and solid subdomains Ω_a and Ω_s, whose boundaries are respectively referred to as Γ_a and Γ_s, while the coupling interface between them is denoted by $\Gamma_{as} = \Gamma_a \cap \Gamma_s$. The outward normal unit vectors to the aforementioned boundaries are symbolized by $\mathbf{n}_a$ and $\mathbf{n}_s$; note that $\mathbf{n}_a = -\mathbf{n}_s$ along Γ_{as}. Γ_o denotes the absorbing boundary, and should be placed at a sufficient distance from geometric singularities in order to guarantee that the acoustic velocity at the wave front is perpendicular to it. Finally, Γ_{Dir} denotes a subregion of Γ_s where Dirichlet boundary conditions are applied.

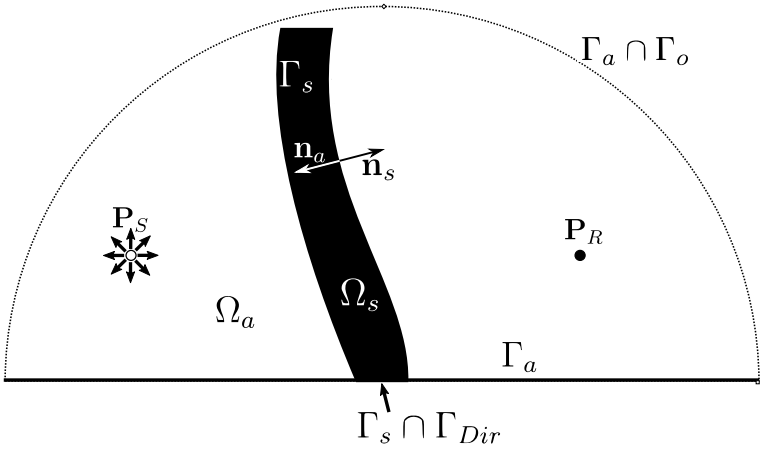

Figure 2.4: Fluid-structure interaction problem scheme.

Sound propagation in the homogeneous fluid corresponding to Ω_a can be described by the Helmholtz equation [13, 32]:

$$\nabla^2 P + \frac{\omega^2}{c_0^2} P = 0 \quad \text{in } \Omega_a \ , \tag{2.75}$$

where P, ω and c_0 are the acoustic pressure's amplitude, the excitation angular frequency and the speed of sound respectively. On the other hand, the governing equilibrium equation in Ω_s for time-harmonic linear elasticity is [32]:

$$\nabla \cdot \boldsymbol{\sigma} + \omega^2 \rho_s \mathbf{U} = 0 \quad \text{in } \Omega_s \ , \tag{2.76}$$

where $\boldsymbol{\sigma}$ and ρ_s are the stress tensor and density of the solid material, whereas $\mathbf{U}$ denotes in this point the vector of displacement amplitudes $\{U, V\}^T$, from which the time-harmonic solution can be derived by applying $u = Ue^{j\omega t}$ and $v = Ve^{j\omega t}$. As for the coupling of Ω_a and Ω_s, both subdomains move together in the normal direction of Γ_{as}: whereas the vibration of the structure induces an acoustic field on the surrounding acoustic domain, a perturbation in sound pressure p act as an external force on the surface, as described respectively by the compatibility Equations (2.77) and (2.78) [32]:

$$(\nabla P)^T \mathbf{n}_a - \omega^2 \rho_0 \mathbf{U}^T \mathbf{n}_a = 0 \quad \text{in } \Gamma_{as} \ , \tag{2.77}$$

$$\boldsymbol{\sigma} \mathbf{n}_s + P \mathbf{n}_s = 0 \quad \text{in } \Gamma_{as} \ , \tag{2.78}$$

where ρ_0 refers to the air density. Equations (2.75 – 2.78) provide the standard way to solve the FSI problem, provided that a well-defined air-solid interface

Γ_{as} is known. However, in the process of TO, the concept of well-defined geometry is disregarded, and fictitious intermediate materials can take place within any element, specially at early stages of the optimization process.

2.2.1. Displacement/pressure mixed formulation in 2D

The mixed $\mathbf{U}/p$ formulation [33, 34] permits to solve the coupled vibroacoustic problem by varying the vibroacoustic properties of each element, hence without explicitly defining the air-solid interface. This formulation is recalled next for the sake of completeness.

By applying the Newton's second law to a control volume in any continuum, and neglecting the body force term, the following expression is obtained [34]:

$$\nabla \cdot \boldsymbol{\sigma} = -\omega^2 \rho \mathbf{U} \ , \tag{2.79}$$

where the stress tensor can be decomposed into its volumetric and deviatoric components:

$$\boldsymbol{\sigma} = K\varepsilon_v \mathbf{I} + 2G\mathbf{e} \ , \tag{2.80}$$

ε_v and $\mathbf{e}$ being the volumetric strain and the deviatoric strain tensor, and $\mathbf{I}$ being the identity matrix. The vibroacoustic behaviour of both structure and air can be characterized by varying the bulk and shear moduli K and G [33]. ε_v is defined for the 2D case as:

$$\varepsilon_v = \frac{\Delta V}{V} = \varepsilon_{xx} + \varepsilon_{yy} = \mathbf{m}^T \boldsymbol{\varepsilon} \ , \tag{2.81}$$

where the strain vector is $\boldsymbol{\varepsilon} = \{\varepsilon_{xx}, \varepsilon_{yy}, \varepsilon_{xy}\}^T$, and $\mathbf{m} = \left\{1, 1, 0\right\}^T$. As an alternative to the pure displacement formulation, acoustic pressure p is also included as a variable [34]:

$$p = -K\varepsilon_v = -K\mathbf{m}^T \boldsymbol{\varepsilon} \ , \tag{2.82}$$

whereas the deviatoric strain $\mathbf{e}$ (here in vector form) in 2D can be calculated as:

$$\mathbf{e} = \boldsymbol{\varepsilon} - \mathbf{m}\frac{\varepsilon_v}{2} = \mathbf{D}\ \boldsymbol{\varepsilon} \ , \tag{2.83}$$

where $\mathbf{D} = \mathbf{I} - 1/2\ \mathbf{m}\mathbf{m}^T$. The weak form of Eqs. (2.79) and (2.80) can be stated as:

$$\int_\Omega \delta\boldsymbol{\varepsilon}^T 2G\mathbf{e}\ \mathrm{d}\Omega - \int_\Omega \delta\boldsymbol{\varepsilon}^T\ (\mathbf{m}p)\ \mathrm{d}\Omega - \omega^2 \int_\Omega \rho\delta\mathbf{U}^T\mathbf{U}\ \mathrm{d}\Omega - \int_\Gamma \delta\mathbf{U}^T\ (\boldsymbol{\sigma}\mathbf{n})\ \mathrm{d}\Gamma = 0\ , \tag{2.84}$$

and by taking into account Eqs. 2.81 and 2.83, it yields:

$$\int_\Omega 2G\delta\boldsymbol{\varepsilon}^T\mathbf{D}\boldsymbol{\varepsilon}\ \mathrm{d}\Omega - \int_\Omega \delta\boldsymbol{\varepsilon}^T\mathbf{m}p\ \mathrm{d}\Omega - \omega^2 \int_\Omega \rho\delta\mathbf{U}^T\mathbf{U}\ \mathrm{d}\Omega - \int_\Gamma \delta\mathbf{U}^T\ (\boldsymbol{\sigma}\mathbf{n})\ \mathrm{d}\Gamma = 0\ . \tag{2.85}$$

On the other hand, the weak form of Eq. (2.82) is:

$$\int_\Omega \delta p\left(p/K + \mathbf{m}^T\boldsymbol{\varepsilon}\right)\ \mathrm{d}\Omega = 0\ . \tag{2.86}$$

Equations (2.85) and (2.86) are of great use in Chapter 5 of this Thesis. Their FE version is recalled in Section 5.2, and due to its high computational cost, its application is restricted to a certain design region (*vibroacoustic domain*) of the problem, whereas the surrounding pure acoustic domain is meshed with the standard pressure formulation.

2.3. Structural shape optimization

2.3.1. Introduction

Simulation-based models, such as the finite element method (FEM) [35], the boundary element method (BEM) or computational fluid dynamics (CFD) are effectively applied during the early stages of product development [36]. In addition, these numerical techniques can be coupled up with deterministic or stochastic optimization methods in order to find optimal designs that minimize a physical quantity, such as the mean compliance (external work) or the peak stress under a certain load case, required weight, etc. [37]. Different optimization approaches are [36]:

- Sizing optimization: it consists, for example, in finding the optimal thickness of a linearly elastic plate. Its main feature is that the problem's domain is fixed throughout the optimization process [38].

- Shape optimization: it concerns the shape optimization of the structure's domain, i.e., the problem is defined in a domain that is, simultaneously, the design variable. This is achieved by selecting a set of variables that define the domain's boundary, given a fixed topology.
- Topology optimization: it serves to determine the number and size of holes, as well as the connectivity of the structure's domain. In this problem, only some boundary conditions (such as loads, possible supports, etc.) and further manufacturing constraints are given beforehand.

2.3.2. Optimization algorithms

A different optimization approach is required to solve each type of optimization problem. Mainly, optimization algorithms fall into one of these two categories: deterministic and stochastic algorithms [39], according to the scheme below:

- Optimization algorithms
  - Deterministic
    - Linear programming
    - Nonlinear programming
    - ...
    - Gradient-based
    - Non-gradient-based
  - Stochastic
    - Heuristic
    - Metaheuristic
      - Population-based
      - Trajectory-based

In this Thesis, the deterministic, nonlinear, gradient-based Method of moving asymptotes (MMA) has been considered to approach topology optimization problems, due to its capacity to efficiently handle a high amount of variables, despite the possibility to converge at local optimum points in non-convex optimization problems. On the contrary, in the proposed shape optimization problem (see Chapter 4), a small number of variables define the geometry. Therefore, the stochastic, metaheuristic, population-based Genetic algorithms (GA) have been used due to their ability to carry out a global search with a reasonable computational cost. Next, both aforementioned optimization methods are briefly recalled for the sake of completeness.

2.3.2.1. Method of moving asymptotes (MMA)

The Method of Moving Asymptotes (MMA) for nonlinear programming was first introduced by K. Svanberg [40] in 1987 and has since then been applied in numerous different ATO problems [33, 41–45]. This method is applied widely in the present Thesis and is recalled below for the sake of completeness.

Consider an optimization problem with the objective function $\mathcal{F}_0$ and a number M of inequality constraints $\mathcal{F}_i$:

$$\boxed{\begin{aligned} &\min_{\boldsymbol{\upsilon}} \mathcal{F}_0(\boldsymbol{\upsilon}) \ , \\ &\text{subject to: } \mathcal{F}_i(\boldsymbol{\upsilon}) \leq 0 \ , \qquad \text{for } i = 1, ..., M \ , \\ &\qquad\qquad \upsilon_j^{min} \leq \upsilon_j \leq \upsilon_j^{max}, \text{ for } j = 1, ..., N \ , \end{aligned}} \tag{2.87}$$

where $\boldsymbol{\upsilon} = \{\upsilon_1, \upsilon_2, ..., \upsilon_N\}^T$ is the vector of N design variables, and υ_j^{min} and υ_j^{max} are the lower and upper bounds of each υ_j. The next lines show briefly the workflow of the MMA algorithm. At each iteration k, a convex approximating subproblem to Problem (2.87) is generated by a summation of rational functions using gradient information. The corresponding approximating functions $\tilde{\mathcal{F}}_i^{(k)}$ can be expressed, for $i = 0, 1, ..., M$, as [40]:

$$\tilde{\mathcal{F}}_i^{(k)}(\boldsymbol{\upsilon}) = \sum_{j=1}^{N} \left(\frac{p_{ij}^{(k)}}{U_j^{(k)} - \upsilon_j} + \frac{q_{ij}^{(k)}}{\upsilon_j - L_j^{(k)}} \right) + r_i^{(k)} \ , \tag{2.88}$$

where the lower L and upper U asymptotes are chosen so that $L_j^{(k)} < \upsilon_j^{(k)} < U_j^{(k)}$ [46], and coefficients $p_{ij}^{(k)}$ and $q_{ij}^{(k)}$ are chosen at each iteration k by using gradient information $\nabla \mathcal{F}_j$ at the corresponding design point $\boldsymbol{\upsilon}^{(k)}$. It yields:

$$p_{ij}^{(k)} = \begin{cases} \left(U_j^{(k)} - \upsilon_j^{(k)}\right)^2 \partial \mathcal{F}_i / \partial \upsilon_j \ , & \text{if } \partial \mathcal{F}_i / \partial \upsilon_j > 0 \ , \\ 0 \ , & \text{if } \partial \mathcal{F}_i / \partial \upsilon_j \leq 0 \ , \end{cases} \tag{2.89}$$

$$q_{ij}^{(k)} = \begin{cases} 0 \ , & \text{if } \partial \mathcal{F}_i / \partial \upsilon_j \geq 0 \ , \\ -\left(\upsilon_j^{(k)} - L_j^{(k)}\right)^2 \partial \mathcal{F}_i / \partial \upsilon_j \ , & \text{if } \partial \mathcal{F}_i / \partial \upsilon_j < 0 \ , \end{cases} \tag{2.90}$$

and $r_i^{(k)}$ is chosen so that the value of the approximating function matches that of the corresponding original function at the current design point:

$$r_i^{(k)} = \mathcal{F}_i(\boldsymbol{\upsilon}^{(k)}) - \sum_{j=1}^{N} \left(\frac{p_{ij}^{(k)}}{U_j^{(k)} - \upsilon_j^{(k)}} + \frac{q_{ij}^{(k)}}{\upsilon_j^{(k)} - L_j^{(k)}} \right) \ . \tag{2.91}$$

Finally, Problem (2.87) turns into:

$$\boxed{\begin{aligned} &\min_{\boldsymbol{\upsilon}} \tilde{\mathcal{F}}_0^{(k)}(\boldsymbol{\upsilon}) \ , \\ &\text{subject to: } \tilde{\mathcal{F}}_i^{(k)}(\boldsymbol{\upsilon}) \leq 0 \ , \qquad \text{for } i = 1, ..., M \ , \\ &\qquad\qquad \upsilon_j^{min} \leq \upsilon_j \leq \upsilon_j^{max}, \text{ for } j = 1, ..., N \ . \end{aligned}} \tag{2.92}$$

The convex approximating optimization problem (2.92) can be then solved by means of the Karush-Kuhn-Tucker (KKT) multipliers contained in vectors $\boldsymbol{\lambda}$, $\boldsymbol{\xi}$ and $\boldsymbol{\eta}$ [40, 47], and the new loss function to minimize can be expressed as:

$$L(\boldsymbol{\upsilon}, \boldsymbol{\lambda}, \boldsymbol{\xi}, \boldsymbol{\eta}) = \tilde{\mathcal{F}}_0(\boldsymbol{\upsilon}) + \sum_{i=1}^{M} \lambda_i \tilde{\mathcal{F}}_i(\boldsymbol{\upsilon}) + \sum_{j=1}^{N} \left(\xi_j \left(\upsilon_j^{min} - \upsilon_j \right) + \eta_j \left(\upsilon_j - \upsilon_j^{max} \right) \right) \ , \tag{2.93}$$

where not only the objective function, but also the lateral and additional constraints have been taken into account. The corresponding KKT conditions [40] are:

$$\frac{\partial L(\boldsymbol{\upsilon}, \boldsymbol{\lambda}, \boldsymbol{\xi}, \boldsymbol{\eta})}{\partial \upsilon_j} = 0 \ , \quad \text{for } j = 1, ..., N \qquad \text{(minimization)} \ , \tag{2.94}$$

$$\lambda_i \tilde{\mathcal{F}}_i(\boldsymbol{\upsilon}) = 0 \ , \quad \text{for } i = 1, ..., M \quad \text{(complimentary slackness)} \ , \tag{2.95}$$

$$\xi_j \left(\upsilon_j^{min} - \upsilon_j \right) = 0 \ , \quad \text{for } j = 1, ..., N \quad \text{(complimentary slackness)} \ , \tag{2.96}$$

$$\eta_j \left(\upsilon_j - \upsilon_j^{max} \right) = 0 \ , \quad \text{for } j = 1, ..., N \quad \text{(complimentary slackness)} \ . \tag{2.97}$$

This system of equations can be solved, for example, by applying a Newton-Rhapson method, and the implementation used throughout this Thesis can be found in [47].

2.3.2.2. Sensitivity analysis

Gradient-based optimization algorithms (such as the aforementioned MMA) require the obtaining of the sensitivities of the objective function $\mathcal{F}_0(\boldsymbol{\upsilon})$ with respect to each design variables. The finite difference method [48] involves solving the global system of equations (2.98) for a small variation of each parameter, and is hence a suitable approach given a small number of design variables (and high number of objective functions, if applicable). However, for TO problems where the number of optimization parameters is high (one

density per element), the adjoint method [48] can reduce significantly the computational cost in comparison to the aforementioned method, and is therefore explained below.

The standard adjoint method [48] can be used to obtain the gradient of $\mathcal{F}_0(\boldsymbol{\upsilon})$ with respect to the design variables υ_j. Given a standard finite element algebraic system (3.52) of the form:

$$\boldsymbol{\kappa}(\boldsymbol{\upsilon})\boldsymbol{\theta}(\boldsymbol{\upsilon}) = \mathbf{F} \ , \tag{2.98}$$

where $\boldsymbol{\kappa}$ contains the global matrices, the column vector $\boldsymbol{\theta}$ consists of the complex nodal solution (unknowns) of the problem, and the source term $\mathbf{F}$ does not vary with the design variables. The augmented objective function $\widehat{\mathcal{F}_0}$ can be defined at each iteration as follows (note that a suitable form for complex-variable problems has been adopted here):

$$\widehat{\mathcal{F}_0}\left(\boldsymbol{\theta}(\boldsymbol{\upsilon})\right) = \mathcal{F}_0\left(\boldsymbol{\theta}(\boldsymbol{\upsilon})\right) - \boldsymbol{\Upsilon}^T(\boldsymbol{\upsilon})\left(\boldsymbol{\kappa}(\boldsymbol{\upsilon})\boldsymbol{\theta}(\boldsymbol{\upsilon}) - \mathbf{F}\right) - \overline{\boldsymbol{\Upsilon}}^T(\boldsymbol{\upsilon})\left(\overline{\boldsymbol{\kappa}(\boldsymbol{\upsilon})\boldsymbol{\theta}(\boldsymbol{\upsilon}) - \mathbf{F}}\right) \ , \tag{2.99}$$

where $\boldsymbol{\Upsilon}(\boldsymbol{\upsilon})$ denotes the Lagrange multipliers column vector, and $\bar{\cdot}$ being the complex conjugate of $\cdot$. Differentiating Eq. (2.99) with respect to any design variable υ_j and reordering the terms yields:

$$\begin{aligned}\frac{\mathrm{D}\widehat{\mathcal{F}_0}}{\mathrm{D}\upsilon_j} = \frac{\partial\mathcal{F}_0}{\partial\upsilon_j} &+ \left(\frac{\partial\boldsymbol{\theta}_{\Re}}{\partial\upsilon_j}\right)^T\left(-\boldsymbol{\kappa}^T\boldsymbol{\Upsilon} - \overline{\boldsymbol{\kappa}^T\boldsymbol{\Upsilon}} \quad + \frac{\partial\mathcal{F}_0}{\partial\boldsymbol{\theta}_{\Re}}\right) \\ &+ \left(\frac{\partial\boldsymbol{\theta}_{\Im}}{\partial\upsilon_j}\right)^T\left(-j\boldsymbol{\kappa}^T\boldsymbol{\Upsilon} + j\overline{\boldsymbol{\kappa}^T\boldsymbol{\Upsilon}} + \frac{\partial\mathcal{F}_0}{\partial\boldsymbol{\theta}_{\Im}}\right) \\ &- \boldsymbol{\Upsilon}^T\left(\frac{\partial\boldsymbol{\kappa}}{\partial\upsilon_j}\boldsymbol{\theta}\right) - \overline{\boldsymbol{\Upsilon}}^T\left(\overline{\frac{\partial\boldsymbol{\kappa}}{\partial\upsilon_j}\boldsymbol{\theta}}\right) \ .\end{aligned} \tag{2.100}$$

Note that the vectors of sensitivities of the objective function with respect to the real and imaginary parts of the nodal solution $\partial\mathcal{F}_0/\partial\boldsymbol{\theta}_{\Re}$ and $\partial\mathcal{F}_0/\partial\boldsymbol{\theta}_{\Im}$ can be derived analytically from the definition of $\mathcal{F}_0$ for a given problem. However, the sensitivities of the nodal solution $\partial\boldsymbol{\theta}_{\Re}/\partial\upsilon_j$ and $\partial\boldsymbol{\theta}_{\Im}/\partial\upsilon_j$ cannot be easily obtained, and $\boldsymbol{\Upsilon}(\boldsymbol{\upsilon})$ is chosen so that:

$$-\boldsymbol{\kappa}^T\boldsymbol{\Upsilon} - \overline{\boldsymbol{\kappa}^T\boldsymbol{\Upsilon}} + \frac{\partial\mathcal{F}_0}{\partial\boldsymbol{\theta}_{\Re}} = 0 \ , \tag{2.101}$$

$$-j\boldsymbol{\kappa}^T\boldsymbol{\Upsilon} + j\overline{\boldsymbol{\kappa}^T\boldsymbol{\Upsilon}} + \frac{\partial\mathcal{F}_0}{\partial\boldsymbol{\theta}_{\Im}} = 0 \ . \tag{2.102}$$

Therefore, by multiplying Eq. (2.102) by $-j$ and adding Eq. (2.101), it is obtained [48]:

$$\boldsymbol{\Upsilon} = \frac{1}{2}\left(\boldsymbol{\kappa}^T(\boldsymbol{\upsilon})\right)^{-1}\left(\frac{\partial \mathcal{F}_0}{\partial \boldsymbol{\theta}_{\Re}} - j\frac{\partial \mathcal{F}_0}{\partial \boldsymbol{\theta}_{\Im}}\right) . \tag{2.103}$$

Finally, the sensitivities of the objective function are calculated as [48]:

$$\frac{\mathrm{D}\widehat{\mathcal{F}_0}}{\mathrm{D}\upsilon_j} = -2\Re\left\{\boldsymbol{\Upsilon}^T\left(\frac{\partial \boldsymbol{\kappa}}{\partial \upsilon_j}\boldsymbol{\theta}\right)\right\} \quad \text{for } j = 1, ..., N , \tag{2.104}$$

where $\Re$ is the real part operator. Note that $\boldsymbol{\Upsilon}$ is solved only once per iteration, and then all the sensitivities can be obtained in a straightforward way, hence reducing the computational cost with respect to the finite difference method.

2.3.2.3. Genetic algorithms

Genetic algorithms (GA) [49] are a type of population-based global search algorithms first developed by John Holland [49] in the 1960s, and probably the most popular type of non-gradient-based optimization algorithms. Together with evolution strategies [50] and evolutionary programming [51], they belong to a larger class called evolutionary algorithms (EA). GA try to mimic the whole process of biological evolution defined by Charles Darwin's theory of natural selection [52]. This theory states that all species develop via the natural selection of small, inheritated variations that can increase or decrease the ability of each individual to compete for the resources, survive, or find a mate to reproduce with. Thus, at any iteration (also known as generation) k, there is a population of s_{pop} individuals [53], each of which is described by the corresponding design vector (called chromosome) $\boldsymbol{\upsilon}_i^{(k)}$ whose entries (variables) $\{\upsilon_1, \upsilon_2, ..., \upsilon_N\}^T$ are called genes.

GA involve (i) the generation of an initial population of s_{pop} chromosomes by means of stochastic methods, (ii) the evaluation of the fitness function (objective function) for every chromosome of the population, (iii) the selection of those individuals that will produce the next generation (parents), (iv) the establishment of the new generation of individuals (offspring) by fitness-proportionate genetic operations, and (v) the replacing of the old population by the new one. Steps (iii-v) are then repeated for a number of generations until the stopping criterion is met [54]. The aforementioned genetic operators are:

- **Selection**. It selects the parents that will be employed in the establishment of the new generation by taking into account their fitness value. By default, MATLAB uses a scaling function where a line is divided in sections whose lengths L_i are inversely proportional to the rank of each individual ($L_i = 1$ for the fittest individual, $1/\sqrt{s_{pop}}$ for the following individuals). Then a stochastic algorithm jumps a fixed distance along the line, and each time it selects as a parent the individual it lands on [54].

- **Crossover**. It creates a pair of children as the combination of genes from two parents. The number of crossover children $s_{cross} = p_c\,(s_{pop} - s_{elit})$ is defined according to the crossover fraction p_c (which is usually high, e.g., within $[0.7, 1]$) and the elite count s_{elit}, i.e., the number of individuals with the lowest fitness value that are guaranteed to survive to the next generation (without mutation).

- **Mutation**. Finally, a number of mutation children $s_{mut} = s_{pop} - (s_{cross} + s_{elit})$ are obtained by applying random changes to a single individual in the current generation (parent) in order to create a child. The mutation probability p_m determines whether a gene will be flipped from its original value when transmitted to the child, and is usually small, in the interval $[0.001, 0.05]$, to prevent the algorithm from jumping around an optimal solution when this is near [54].

A graphical representation of the three aforementioned genetic operators is shown in Figure 2.5.

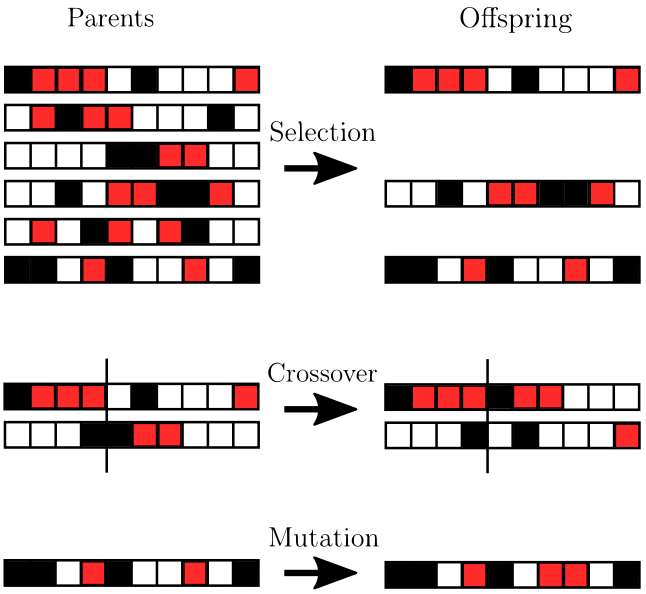

Figure 2.5: Selection, crossover, and mutation genetic operators. The design vectors corresponding to several individuals are represented above. Different numerical entries are depicted as colours black, red, and white for simplicity.

2.3.3. Topology optimization

Topology optimization (TO) is an optimization framework generally used to obtain the optimal topology (i.e., material distribution within a specific design domain) that minimizes a given objective function, via the parametrization of the material's properties in the continuum [37].

The traditional approach to TO considers as continuous variables the densities v_j of the material within each element of the design's domain [55]. These usually range from 0 (which corresponds to air elements) to 1 (which refers to the solid material). Additionally, several continuous material interpolation functions exist [37, 46, 56], which allow obtaining fictitious material properties for intermediate values of v_j, e.g., the solid isotropic material with penalization (SIMP) and the rational approximation of material properties (RAMP) penalty methods, which are further explained below.

2.3.3.1. Material interpolation schemes

Considering a TO problem in which the optimal material distribution is to be found, at each design point $\boldsymbol{v}^{(k)}$, material properties ϱ are interpolated within each element from those of the air (usually $\varrho_0 = 0$) to those of the solid material (usually $\varrho_s = 1$), depending on v_j. Several penalty approaches are suggested in the literature in order to penalize undesired intermediate values of v_j, such as the SIMP [55] method:

$$\varrho(v_j) = \varrho_0 + (\varrho_s - \varrho_0){v_j}^p \ , \tag{2.105}$$

where p is the penalty factor (usually $p = 3$) [56]. On the other hand, the RAMP method [46] can be applied by following:

$$\varrho(v_j) = \varrho_0 + (\varrho_s - \varrho_0)\phi\left(v_j\right) \ , \tag{2.106}$$

where the penalty function ϕ depends on the penalty factor, usually with $q = 4$:

$$\phi\left(v_j\right) = \frac{v_j}{1 + q(1 - v_j)} \ . \tag{2.107}$$

Additionally, a three-material RAMP scheme has been studied in Chapter 5 of this Thesis.

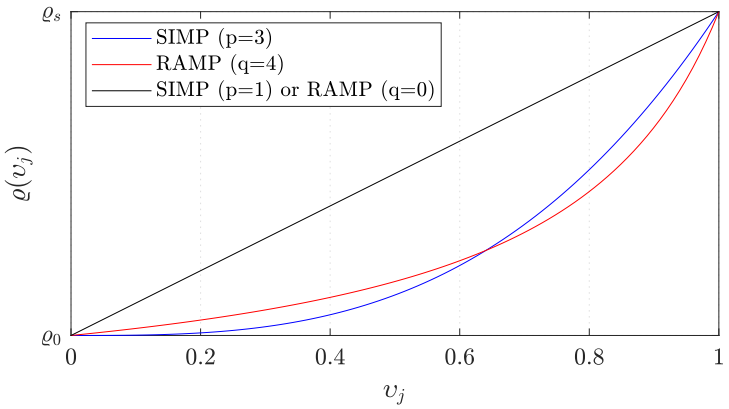

Figure 2.6: Comparison of SIMP and RAMP interpolation schemes.

In Figure 2.6 the two aforementioned penalty methods are compared to the linear interpolation of any material property ϱ.

Chapter 3

Acoustic optimization of dissipative and hybrid mufflers

Existing schemes for the acoustic optimization of automotive and any other type of mufflers can be classified into three groups: (i) the shape optimization of reactive mufflers refers to the obtaining of their optimal configuration (number of chambers, chamber partitions, extended inlet/outlet ducts, etc.) and the respective dimensions of each of the aforementioned elements; (ii) the shape optimization of dissipative mufflers involves the consideration of some additional variables, such as absorbent fibre type and bulk density into each dissipative chamber, as well as certain features of the perforated plate located between the chamber and the central air duct, such as porosity, thickness, etc. Usually it is feasible to perform low-dimensional problems such as (i) and (ii) by means of heuristic optimization algorithms like GA, due to the relatively small amount of design variables and high convergence speed. However, (iii) the topology optimization of reactive mufflers is performed by gradient-based methods, which allow the obtaining of more intricate partitions within the chambers.

Additionally, (iv) the topology optimization of dissipative and hybrid mufflers has been addressed in this Chapter, by allowing for non-uniform distributions of the absorbent material's bulk density within the chamber.

3.1. Introduction

Mufflers are passive devices which are connected to a noise source, and whose objective is to reduce the acoustic level downstream to an acceptable value. Nowadays there exist several muffler configurations, with designs ranging from a single expansion chamber to intricate set-ups including several cavities and resonators connected together. Generally speaking, mufflers are divided into two groups (reactive and dissipative), depending on the working principle [13].

3.1.1. Classification of mufflers

3.1.1.1. Reactive configuration

In a reactive muffler, a change of the duct's cross section and other geometric particularities make part of the acoustic energy to be reflected back to the source, causing a destructive wave interaction [13].

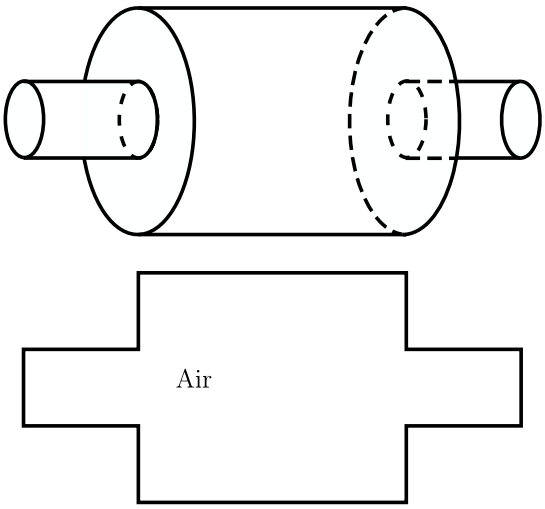

Figure 3.1: Reactive muffler consisting of one expansion chamber.

One particular type of reactive mufflers are resonators. These include cavities and geometric discontinuities, which at certain (natural) frequencies

can partially enter into resonance, thus absorbing most of the acoustic energy, and preventing it to be transmitted.

3.1.1.2. Dissipative configuration

In a dissipative muffler, attenuation is achieved by means of the use of absorbent materials with high specific area (normally fibres), which convert the acoustic energy into heat. The use of perforated surfaces and tubes can also lead to a reduction of the transmitted acoustic energy.

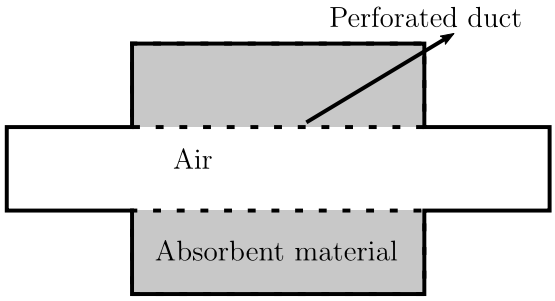

Figure 3.2: Dissipative muffler with absorbent material.

In addition to the absorbing material, some additional attenuation is achieved due to the reactive effects taking place at the expansion and contraction of the chamber. In a similar way, the flow of a real fluid along a reactive muffler produces some dissipation of acoustic energy, due to the aforementioned changes of the cross section of the tube.

Additionally, hybrid mufflers containing both reactive and dissipative chambers have also been studied in this Chapter.

3.1.2. Optimization of mufflers

3.1.2.1. Optimization of reactive mufflers

Reactive mufflers can provide good acoustic attenuation at low to mid frequencies, even with relatively reduced dimensions [13], and their acoustic behaviour can be improved, at target frequencies, by applying shape optimization to the components of the muffler, e.g., expansion chamber, extended

ducts, resonators, etc. Barbieri and Barbieri [57] found an optimized geometry of a circular reactive chamber with extended inlet and outlet ducts by employing the Zoutendijk's feasible directions method [58]. Chang and Chiu [59] performed sizing optimization to designs with perforated duct using GA (see Section 2.3.2). GA were also used by De Lima *et al.* [60] in order to conduct the parametric optimization of a reactive muffler with extended ducts, as well as the shape optimization of the duct's profile by the use of control points to approximate its boundary with cubic curves.

TO [61] can also be applied to reactive mufflers in order to distribute rigid material and create partitions inside the reactive chamber. The density approach is applied by employing material interpolation schemes, such as the RAMP [46] in order to make the acoustic properties associated with each element of the FE mesh to vary from those of the air to those of sound-hard material [62, 63]. The sensitivities of the objective function with respect to the element densities are normally filtered [41] in order to avoid numerical instabilities and mesh-dependent solutions. Lee [64] used the MMA [40] to create partitions in a reactive muffler and to increase the Transmission Loss (TL) at target frequencies, experimentally validating the results. Lee and Kim [62] used the RAMP model along with the MMA to create partitions in an expansion chamber. Yedeg *et al.* [63] also used the MMA to create internal walls within a perforated muffler, obtaining components that resembled cylindrical pipes and Helmholtz resonators. On the other hand, Azevedo *et al.* [65] used the discrete optimization approach by employing Bi-directional Evolutionary Structural Optimization (BESO) method to create barriers within an expansion chamber using discrete variables.

3.1.2.2. Optimization of dissipative and hybrid mufflers

Regarding dissipative mufflers, i.e., those containing absorbent material, they offer broadband attenuation essentially at mid and high frequencies [13]. Yoon [66] and Lee *et al.* [64] used the MMA to distribute elastic and poroelastic material elements (as well as air elements) within the muffler's reactive chamber by the use of a three-phase material scheme (air,porous,elastic). Furthermore, Selamet *et al.* [67, 68] studied the acoustic behaviour of dissipative mufflers containing several layers of material with different compaction densities.

Considerable attenuation can be obtained in a broad range of the spectrum by using the so-called hybrid muffler, that combines reactive and dissipative chambers [69]. Chiu [70] used GA to maximize the attenuation of a hybrid muffler in a target frequency range, by optimizing the dimensions and the amount of absorbent material within the dissipative chamber (hence its filling density).

3.2. Acoustic modelling of reactive and dissipative mufflers

3.2.1. Previous considerations: perforated ducts and absorbing materials

Perforated plates can be usually found in a muffler [13, 71–73], specially in order to separate the central air passage from the annular chambers. Their acoustic behaviour can be characterized by means of the corresponding impedance Z_p.

Likewise, the absorbent material can be modelled as an equivalent fluid by using the corresponding complex acoustic properties [22].

3.2.1.1. Characteristic impedance of a perforated surface

The impedance of a perforated plate is used to relate the pressure at both sides of the plate, and the velocity of the air across the orifices. It is defined as:

$$Z_p = \frac{P_{in} - P_{out}}{U_n} = R_0 + jX_0 \ , \tag{3.1}$$

where P_{in}, P_{out} and U_n are the acoustic pressure at both sides (inlet/outlet) of the orifice, and the mean acoustic velocity through the hole's section. The impedance can be expressed in terms of resistance R_0 and reactance X_0, as denoted in Equation (3.1).

The airflow across the holes involves several reflective and dissipative effects. The acoustic field in the vicinity of the perforated element can be relatively complex [74], and is studied in the literature in a simplified way [75–77], according to Equation (3.1).

(i) Reactive chamber and non-moving medium

The first case corresponds to a perforated plate separating two acoustic domains in absence of mean flow. A wide variety of impedance models can be found in the literature [71]. However, in this Section only the most common models are introduced, which will be hence used hereinafter in this Thesis.

The expression by Sullivan and Crocker can be found in references [72, 73]:

$$Z_p = \rho_0 c_0 \frac{6 \cdot 10^{-3} + jk_0 \left(t_p + 0.75 d_h\right)}{\sigma} \ , \tag{3.2}$$

d_h, t_p and σ being the diameter of the orifices, the thickness of the plate and the porosity, respectively.

(ii) Reactive chamber and mean flow along the central duct

In order to model the acoustic coupling at a perforated circular duct separating an air passage with grazing mean flow and a reactive chamber (with no absorbent material), the empirical impedance model presented by Lee and Ih [71] was found to show good correlation with experimental data [78] and is therefore used in this study. The dimensionless impedance ς_p for a perforated surface in the presence of mean flow is:

$$\varsigma_p = \frac{Z_p}{\rho_0 c_0} = \alpha + j\beta \ , \tag{3.3}$$

where the values of the real (resistance) and imaginary (reactance) parts depend on the geometric parameters of the perforated plate [15]:

$$\alpha = \frac{\alpha_0 \left(1 + \alpha_1 \left|f - f_{crit}\right|\right) \left(1 + \alpha_2 M_{mf}\right) \left(1 + \alpha_3 d_h\right) \left(1 + \alpha_4 t_p\right)}{\sigma} \ , \tag{3.4}$$

$$\beta = \frac{\beta_0 \left(1 + \beta_1 d_h\right) \left(1 + \beta_2 t_p\right) \left(1 + \beta_3 M_{mf}\right) \left(1 + \beta_4 f\right)}{\sigma} \ . \tag{3.5}$$

The coefficients for the evaluation of the resistance α_j and reactance β_j, as well as the valid range of values for the parameters involved in Eqs. (3.4)

and (3.5), are shown in Table 3.1 (note that some of these coefficients have dimensions, here in SI units) [71].

α_0	0.000394	β_0	-0.006
α_1	0.00784	β_1	194
α_2	14.9	β_2	432
α_3	296	β_3	-1.72
α_4	-127	β_4	-0.00662

Table 3.1: *Coefficients for the evaluation of the acoustic impedance.*

	Minimum	Maximum
f	60 Hz	4000 Hz
M_{mf}	0	0.2
d_h	0.002 m	0.009 m
t_p	0.001 m	0.005 m
σ	2.79 %	22.3 %

Table 3.2: *Valid range of the parameters*

The valid range of values for the parameters involved in Eqs. (3.4) and (3.5) is shown in Table 3.2. Also, the critical frequency f_{crit} is related to M_{mf} and d_h following the relation:

$$f_{crit} = \phi_1 \frac{1 + \phi_2 M_{mf}}{1 + \phi_3 d_h} \ , \tag{3.6}$$

with $\phi_1 = 412$, $\phi_2 = 104$ and $\phi_3 = 274$ [71].

(iii) Dissipative chamber

In case of a dissipative chamber, the effect of the fibrous material within the chamber should be captured, and good correlation with experimental results was found for Kirby and Denia's expression shown below [78]:

$$Z_p = Z_0 \left(\varsigma_p + \frac{j0.425 k_0 d_h \left(\rho_m / \rho_0 - 1 \right) F(\sigma)}{\sigma} \right) \ , \tag{3.7}$$

where the hole interaction factor $F(\sigma)$ has been approximated throughout this study by the mean value [77, 78] of the expressions given by Ingard [79] and Fok [80], denoted below by F_I and F_F, respectively:

$$F_I \left(\sigma \right) = 1 - 0.7\sqrt{\sigma} \ , \tag{3.8}$$

$$F_F \left(\sigma \right) = 1 - 1.41\sqrt{\sigma} + 0.34\sqrt{\sigma^3} + 0.34\sqrt{\sigma^5} \ . \tag{3.9}$$

3.2.1.2. Absorbent materials

Delany and Bazley's empirical model [81] has been used in this study to estimate the characteristic acoustic impedance Z_m and material wavenumber k_m (or equivalently the propagation constant) in terms of frequency f and steady airflow resistivity R.

Absorbent material characterization

First, R can be evaluated at room temperature (R_0) as a function of the filling or bulk density ρ_b by the expression [82]:

$$R_0 = A_1 \rho_b^{A_2} \ , \tag{3.10}$$

where coefficients $A_1 = 1.0831$ and $A_2 = 1.8279$ have been obtained from experimental data for the material considered throughout this Thesis, (Owens Corning texturized fibreglass roving) [69]: $R_0 = 4896$ Pa s/m^2 for $\rho_b = 100$ kg/m^3, and $R_0 = 17378$ Pa s/m^2 for $\rho_b = 200$ kg/m^3 [67]. This interpolation has been hereinafter considered valid for ρ_b between 50 kg/m^3 and 250 kg/m^3 [67–69], and any value of filling density between these two limits has been therefore considered suitable from a manufacturing point of view.

Additionally, Christie's power law [83] has been used in this study to evaluate R at high temperature:

$$R = R_0 \left(\frac{T + 273.15}{T_0 + 273.15} \right)^{0.6} \ , \tag{3.11}$$

with $T_0 = 25$ °C. Once R at the working conditions are known, Delany and Bazley's aforementioned expressions for Z_m and k_m are [81]:

$$Z_m = Z_0 \left(1 + a_5 \xi^{a_6} - j a_7 \xi^{a_8}\right) \ , \tag{3.12}$$

$$k_m = k_0 \left(1 + a_3 \xi^{a_4} - j a_1 \xi^{a_2}\right) \ , \tag{3.13}$$

Z_0 and k_0 being the acoustic characteristic impedance of the air and its wavenumber, while the dimensionless frequency parameter is defined as $\xi = \rho_0 f / R$. Coefficients and exponents a_i for the material under study are shown in Table 3.3, and have been kept constant with temperature [83–85]. Finally,

the complex equivalent density ρ_m and speed of sound c_m are expressed as:

$$\rho_m = \frac{Z_m}{c_m} \ , \tag{3.14}$$

$$c_m = \frac{\omega}{k_m} \ , \tag{3.15}$$

ω being the angular frequency of the acoustic excitation.

Texturized fibre glass	
a_1	0.189
a_2	-0.595
a_3	0.160
a_4	-0.577
a_5	0.095
a_6	-0.754
a_7	0.085
a_8	-0.732

Table 3.3: *Coefficients and exponents for the calculation of the equivalent acoustic properties.*

3.2.2. Finite element method

This Section describes the FE formulation of the acoustic problem and the role played by the design variables (such as the filling density ρ_b of each element or the chamber dimensions L_x and L_r) in the equations.

Figure 3.3 shows a sketch of the perforated dissipative muffler considered in this Chapter. It consists of a central air passage carrying a mean flow, and a surrounding annular chamber filled with absorbent material. Additionally, the perforated surface between the chamber and the central duct allows for acoustic interaction between them, while reducing back-pressure and preventing the absorbent material from being dragged out by the exhaust flow [15, 67–69, 86, 87].

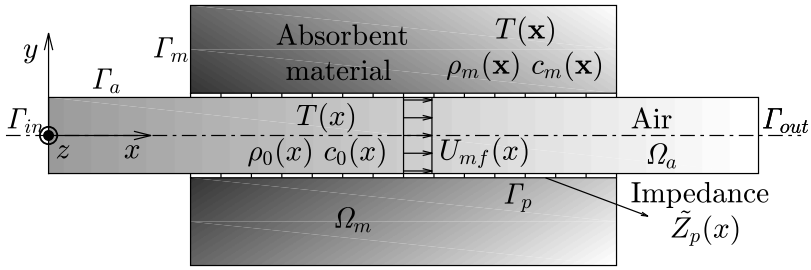

Figure 3.3: Perforated dissipative muffler with heterogeneous absorbent material.

The noise control device has been divided into two subdomains: the central passage, denoted by Ω_a, and the annular dissipative chamber, Ω_m. Γ_p denotes the perforated surface between them, Γ_a and Γ_m represent the rigid boundaries of the muffler (with normal velocity U_n equal to zero), while Γ_{in} and Γ_{out} stand for the inlet and outlet sections of the muffler.

Following the approach presented in [15], an axial temperature gradient has been considered at the central passage, which causes not only the acoustic properties of the air (density ρ_0 and speed of sound c_0) to vary with respect to the x coordinate, but also the mean flow speed U_{mf}. On the other hand, axial and radial temperature variations have also been considered inside the chamber. The fibrous medium can be modelled as an equivalent fluid, in terms of its position-dependent complex equivalent properties, $\rho_m(\mathbf{x})$ and $c_m(\mathbf{x})$, which can be expressed, for a given material, as a function of filling density $\rho_b(\mathbf{x})$, temperature $T(\mathbf{x})$ and acoustic frequency f. Finally, the perforated duct has been modelled by evaluating the acoustic impedance $\tilde{Z}_p(x)$.

The FE model described in [15] has been used throughout this Chapter and recalled below for the sake of completeness. Wave propagation has been formulated in terms of acoustic velocity potential within Ω_a, and in terms of acoustic pressure within Ω_m, as explained in Sections 3.2.2.1 and 3.2.2.2, whereas the coupling between them across the perforated surface is recalled in Section 3.2.2.3.

3.2.2.1. Wave propagation along the central passage domain Ω_a

An axial temperature gradient has been considered along the central passage. This implies the acoustic properties of the air $c_0(x)$ and $\rho_0(x)$ to vary axially within Ω_a. In addition, a mean axial flow may be considered, with velocity $\mathbf{U}_{mf}(x) = \{U_{mf}(x), 0, 0\}$. A convenient form of the wave equation for the described medium is the one formulated in terms of velocity potential ϕ in Eq. (2.38):

$$\nabla \cdot (\rho_0 \nabla \phi) - \rho_0 \frac{\mathrm{D}}{\mathrm{D}t}\left(\frac{1}{c_0^2}\frac{\mathrm{D}}{\mathrm{D}t}\phi\right) = 0 \ . \tag{3.16}$$

Acoustic velocity $\mathbf{u}$ and pressure p can be obtained from ϕ as [19]:

$$\mathbf{u} = \{u,\ v,\ w\}^T = \nabla\phi \ , \tag{3.17}$$

$$p = -\rho_0 \frac{\mathrm{D}\phi}{\mathrm{D}t} \ . \tag{3.18}$$

A harmonic time dependence of the acoustic magnitudes involved has been assumed, with $\phi(\mathbf{x}, t) = \Phi(\mathbf{x})e^{j\omega t}$ and $p(\mathbf{x}, t) = P(\mathbf{x})e^{j\omega t}$. Hence the total time derivative can be written as:

$$\frac{\mathrm{D}}{\mathrm{D}t} = \frac{\partial}{\partial t} + \mathbf{U}_{mf} \cdot \nabla = j\omega + U_{mf}\frac{\partial}{\partial x} \ , \tag{3.19}$$

j being the imaginary unit. By introducing Eq. (3.19) into Eq. (3.16), it is obtained [15]:

$$\begin{aligned}\nabla \cdot (\rho_0 \nabla \Phi) - \frac{\rho_0 U_{mf}^2}{c_0^2}\frac{\partial^2 \Phi}{\partial x^2} - \frac{2\rho_0 j\omega U_{mf}}{{c_0}^2}\frac{\partial \Phi}{\partial x} - \rho_0 U_{mf}^2 \frac{\partial\left(1/c_0^2\right)}{\partial x}\frac{\partial \Phi}{\partial x} \\ - \frac{\rho_0 U_{mf}}{c_0^2}\frac{\partial U_{mf}}{\partial x}\frac{\partial \Phi}{\partial x} - \rho_0 j\omega U_{mf}\frac{\partial\left(1/c_0^2\right)}{\partial x}\Phi + \frac{\rho_0\omega^2}{c_0^2}\Phi = 0 \ .\end{aligned} \tag{3.20}$$

The weighted residual statement (with weighting function Ψ) and the divergence theorem [35] are applied to Eq. (3.20). After further manipulation,

it yields [15]:

$$
\begin{aligned}
&-\int_{\Omega_a} \rho_0 \nabla^T \Psi \mathbf{M} \nabla \Phi \, \mathrm{d}\Omega \\
&\qquad + \int_{\Omega_a} \Psi \left(\frac{U_{mf}^2}{c_0^2} \frac{\partial \rho_0}{\partial x} + \frac{\rho_0 U_{mf}}{c_0^2} \frac{\partial U_{mf}}{\partial x} - \frac{2\rho_0 j\omega U_{mf}}{c_0^2} \right) \frac{\partial \Phi}{\partial x} \, \mathrm{d}\Omega \\
&+ \int_{\Omega_a} \Psi \left(-\rho_0 j\omega U_{mf} \frac{\partial \left(1/c_0^2\right)}{\partial x} + \frac{\rho_0 \omega^2}{c_0^2} \right) \Phi \, \mathrm{d}\Omega + \int_{\Gamma_a} \rho_0 \, \Psi \mathbf{n}^T \mathbf{M} \nabla \Phi \, \mathrm{d}\Gamma = 0 \ ,
\end{aligned}
\tag{3.21}
$$

where $\mathbf{n}$ is the outward normal unit vector to the boundary Γ, and $\mathbf{M}$ is the matrix defined by:

$$
\mathbf{M} = \begin{bmatrix} 1 - {M_{mf}}^2 & 0 & 0 \\ 0 & 1 & 0 \\ 0 & 0 & 1 \end{bmatrix} \ , \tag{3.22}
$$

$M_{mf}(x) = U_{mf}(x)/c_0(x)$ being the Mach number. The FE discretization given by Eqs. (3.23) and (3.24) is applied to Eq. (3.21), where $\mathbf{N}$ is the row vector of nodal shape functions, and $\tilde{\mathbf{\Phi}}$ and $\tilde{\mathbf{\Psi}}$ are the vectors containing the nodal values of Φ and Ψ:

$$
\Phi(\mathbf{x}) = \mathbf{N}(\mathbf{x}) \tilde{\mathbf{\Phi}} \ , \tag{3.23}
$$

$$
\Psi(\mathbf{x}) = \mathbf{N}(\mathbf{x}) \tilde{\mathbf{\Psi}} \ . \tag{3.24}
$$

The use of the Galerkin approach [35] leads to the following algebraic system, expressed here in compact notation [15]:

$$
\left(\mathbf{K}_a + j\omega \left(\mathbf{C}_{a1} + \mathbf{C}_{a2} \right) - \omega^2 \mathbf{M}_a \right) \tilde{\mathbf{\Phi}} = \mathbf{F}_a \ , \tag{3.25}
$$

where the stiffness, damping and mass matrices, as well as the force vector are respectively [15]:

$$\mathbf{K}_a = \sum_{e=1}^{N_a^e} \int_{\Omega_a^e} \rho_0 \left(\nabla \mathbf{N}\right)^T \mathbf{M} \nabla \mathbf{N} \, \mathrm{d}\Omega \ , \tag{3.26}$$

$$\mathbf{C}_{a1} = \sum_{e=1}^{N_a^e} \int_{\Omega_a^e} \frac{2\rho_0 U_{mf}}{c_0^2} \mathbf{N}^T \frac{\partial \mathbf{N}}{\partial x} \, \mathrm{d}\Omega \ , \tag{3.27}$$

$$\mathbf{C}_{a2} = \sum_{e=1}^{N_a^e} \int_{\Omega_a^e} \rho_0 U_{mf} \frac{\partial \left(1/c_0^2\right)}{\partial x} \mathbf{N}^T \mathbf{N} \, \mathrm{d}\Omega \ , \tag{3.28}$$

$$\mathbf{M}_a = \sum_{e=1}^{N_a^e} \int_{\Omega_a^e} \frac{\rho_0}{c_0^2} \mathbf{N}^T \mathbf{N} \, \mathrm{d}\Omega \ , \tag{3.29}$$

$$\begin{aligned} \mathbf{F}_a &= \sum_{e=1}^{N_a^e} \int_{\Gamma_a^e \cap \Gamma} \rho_0 \mathbf{N}^T \mathbf{n}^T \mathbf{M} \nabla \Phi \, \mathrm{d}\Gamma \\ &= \sum_{e=1}^{N_a^e} \int_{\Gamma_a^e \cap \Gamma_{bc}} \rho_0 \mathbf{N}^T \left(1 - M_{mf}^2\right) \frac{\partial \Phi}{\partial n} + \int_{\Gamma_a^e \cap \Gamma_p} \rho_0 \mathbf{N}^T \frac{\partial \Phi}{\partial n} \, \mathrm{d}\Gamma \ , \end{aligned} \tag{3.30}$$

N_a^e, Ω_a^e and Γ_a^e being the number of elements within Ω_a, as well as the domain and boundary of each of these elements in the summation term. A normal acoustic velocity to the boundaries may exist where the natural rigid wall condition is not satisfied [88], i.e., $\Gamma_{bc} = \Gamma_{in} \cup \Gamma_{out}$ (inlet/outlet sections) and Γ_p (perforated duct surface).

3.2.2.2. Wave propagation in the dissipative chamber Ω_m

In the absence of mean flow, and considering a heterogeneous medium, the simpler harmonic form of the wave equation expressed in terms of pressure (harmonic form of Eq.(2.28)) can be used [15, 19, 86, 87]:

$$\nabla \cdot \left(\frac{1}{\rho_m} \nabla P\right) + \frac{\omega^2}{\rho_m c_m^2} P = 0 \ . \tag{3.31}$$

The FE method has been applied to Eq. (3.31) in an analogous way to Section 3.2.2.1, yielding the following algebraic system, expressed here in compact form [15]:

$$\left(\mathbf{K}_m - \omega^2 \mathbf{M}_m\right) \tilde{\mathbf{P}} = \mathbf{F}_m \ , \tag{3.32}$$

where the matrices $\mathbf{K}_m$, $\mathbf{M}_m$ and the vector $\mathbf{F}_m$ are defined below: [15]

$$\mathbf{K}_m = \sum_{e=1}^{N_m^e} \int_{\Omega_m^e} \frac{1}{\rho_m} \left(\nabla \mathbf{N}\right)^T \left(\nabla \mathbf{N}\right) \, \mathrm{d}\Omega \ , \tag{3.33}$$

$$\mathbf{M}_m = \sum_{e=1}^{N_m^e} \int_{\Omega_m^e} \frac{1}{\rho_m c_m^2} \mathbf{N}^T \mathbf{N} \, \mathrm{d}\Omega \ , \tag{3.34}$$

$$\mathbf{F}_m = \sum_{e=1}^{N_m^e} \int_{\Gamma_m^e \cap \Gamma_p} \frac{1}{\rho_m} \mathbf{N}^T \frac{\partial P}{\partial n} \, \mathrm{d}\Gamma \ , \tag{3.35}$$

N_m^e, Ω_m^e and Γ_m^e being the number of elements within Ω_m, as well as the domain and boundary of each of these elements in the summation term. The equivalent acoustic properties of the poroelastic medium ρ_m and c_m have been calculated according to Eqs. (3.14) and (3.15). Note that, although just one variable ρ_b is assigned to each element, ρ_m and c_m might vary within Ω_m^e due to thermal effects.

3.2.2.3. Acoustic coupling at the perforated duct

The acoustic coupling between Ω_a and Ω_m has been modelled by means of an impedance associated with the perforated surface. This is defined as the ratio of the acoustic pressure drop between both sides of the plate to the acoustic velocity across the orifices U_n [13]:

$$Z_p = \frac{P_a - P_m}{U_n} \ , \tag{3.36}$$

where P_a and P_m are the pressures at both sides of the perforated screen. The reader is referred to Section 3.2.1.1 for the calculation of Z_p. On the other hand, recalling Eqs. (3.17 – 3.19) within Ω_a yields:

$$P_a = -\rho_0 \left(j\omega \Phi + U_{mf} \ \partial \Phi / \partial x\right) \ . \tag{3.37}$$

Assuming continuity of normal velocity across the perforated surface [78], $U_{n_a} = -U_{n_m}$, and substituting $\partial \Phi / \partial n = U_n$ from Eq. (3.36) into the second term of Eq. (3.30), the contribution of the perforated surface to $\mathbf{F}_a$ is obtained [15]:

$$\mathbf{F}_a^{Z_p} = \int_{\Gamma_a^e \cap \Gamma_p} \rho_0 \mathbf{N}^T \left(\frac{-\rho_0 \left(j\omega \Phi + U_{mf} \ \partial \Phi / \partial x\right)}{Z_p} - \frac{P_m}{Z_p} \right) \, \mathrm{d}\Gamma \ . \tag{3.38}$$

$\mathbf{F}_m^{Z_p}$ can be derived analogously, replacing the term $\partial P_m/\partial n = -\rho_m j\omega(-U_n)$ into Eq. (3.35), where U_{n_m} is obtained from Eq. (3.36) [15]:

$$\mathbf{F}_m^{Z_p} = \int_{\Gamma_a^e \cap \Gamma_p} \mathbf{N}^T \left(\frac{\rho_0 \omega^2 \Phi - \rho_0 j\omega U_{mf}\ \partial\Phi/\partial x}{Z_p} - \frac{j\omega P_m}{Z_p} \right) \mathrm{d}\Gamma \ . \tag{3.39}$$

No mesh continuity is required between both domains, although a conforming mesh has been used between Ω_a and Ω_m in order to simplify the computations, and shape functions at both sides of the perforated surface are therefore equal [15]. The force terms described in Eqs. (3.38) and (3.39) are moved to the left-hand side of the algebraic system, following the relations:

$$\mathbf{F}_a^{Z_p} = \left(-\mathbf{K}_{aa}^{Z_p} - j\omega \mathbf{C}_{aa}^{Z_p} \right) \tilde{\mathbf{\Phi}}_a - \mathbf{K}_{am}^{Z_p} \tilde{\mathbf{P}}_m \ , \tag{3.40}$$

$$\mathbf{F}_m^{Z_p} = \left(-j\omega \mathbf{C}_{ma}^{Z_p} + \omega^2 \mathbf{M}_{ma}^{Z_p} \right) \tilde{\mathbf{\Phi}}_a - j\omega \mathbf{C}_{mm}^{Z_p} \tilde{\mathbf{P}}_m \ , \tag{3.41}$$

obtaining the following new terms [15]:

$$\mathbf{K}_{aa}^{Z_p} = \sum_{e=1}^{N_a^e} \int_{\Gamma_a^e \cap \Gamma_p} \frac{\rho_0^2 U_{mf} \mathbf{N}^T}{\tilde{Z}_p} \frac{\partial \mathbf{N}}{\partial x} \, \mathrm{d}\Gamma \ , \tag{3.42}$$

$$\mathbf{K}_{am}^{Z_p} = \sum_{e=1}^{N_a^e} \int_{\Gamma_a^e \cap \Gamma_p} \frac{\rho_0 \mathbf{N}^T \mathbf{N}}{\tilde{Z}_p} \, \mathrm{d}\Gamma \ , \tag{3.43}$$

$$\mathbf{C}_{aa}^{Z_p} = \sum_{e=1}^{N_a^e} \int_{\Gamma_a^e \cap \Gamma_p} \frac{\rho_0^2 \mathbf{N}^T \mathbf{N}}{\tilde{Z}_p} \, \mathrm{d}\Gamma \ , \tag{3.44}$$

$$\mathbf{C}_{mm}^{Z_p} = \sum_{e=1}^{N_a^e} \int_{\Gamma_m^e \cap \Gamma_p} \frac{\mathbf{N}^T \mathbf{N}}{\tilde{Z}_p} \, \mathrm{d}\Gamma \ , \tag{3.45}$$

$$\mathbf{C}_{ma}^{Z_p} = \sum_{e=1}^{N_a^e} \int_{\Gamma_m^e \cap \Gamma_p} \frac{\rho_0 U_{mf} \mathbf{N}^T}{\tilde{Z}_p} \frac{\partial \mathbf{N}}{\partial x} \, \mathrm{d}\Gamma \ , \tag{3.46}$$

$$\mathbf{M}_{ma}^{Z_p} = \sum_{e=1}^{N_a^e} \int_{\Gamma_m^e \cap \Gamma_p} \frac{\rho_0 \mathbf{N}^T \mathbf{N}}{\tilde{Z}_p} \, \mathrm{d}\Gamma \ . \tag{3.47}$$

3.2.2.4. Boundary conditions at the outlet

TL computations require an anechoic termination [13]. This has been achieved by prescribing an acoustic impedance at the outlet section equal to

the characteristic impedance of the propagation medium:

$$Z = \frac{P}{U_n} = \frac{P}{\partial \Phi / \partial x} = Z_0 = \rho_0 c_0 \ . \tag{3.48}$$

Introducing P from Eq. (3.48) into Eq. (3.37), and solving for $\partial \Phi / \partial x$ leads to [15]:

$$\frac{\partial \Phi}{\partial x} = -\frac{j\omega\rho_0 \Phi}{Z_0 + \rho_0 U_{mf}} \ . \tag{3.49}$$

Eq. (3.49) is then introduced into the first term of Eq. (3.30), and the resultant expression is evaluated at the outlet section, obtaining:

$$\mathbf{F}_a^{Z_{out}} = -j\omega\rho_0^2 \frac{1 - M_{mf}^2}{Z + \rho_0 U_{mf}} \sum_{e=1}^{N_e^{out}} \int_{\Gamma_e \cap \Gamma_{out}} \mathbf{N}^T \Phi \ \mathrm{d}\Gamma \ . \tag{3.50}$$

Eq. (3.50) is moved to the left-hand side of Eq. (3.25). In compact form, $\mathbf{F}_a^{Z_{out}} = -j\omega \mathbf{C}_a^{Z_{out}} \tilde{\mathbf{\Phi}}_a$, with the new matrix $\mathbf{C}_a^{Z_{out}}$ given by:

$$\mathbf{C}_a^{Z_{out}} = \rho_0^2 \frac{1 - M_{mf}^2}{Z + \rho_0 U_{mf}} \sum_{e=1}^{N_e^{out}} \int_{\Gamma_e \cap \Gamma_{out}} \mathbf{N}^T \mathbf{N} \ \mathrm{d}\Gamma \ . \tag{3.51}$$

3.2.2.5. Final system of equations

The resulting global system of equations is:

$$\left(\begin{bmatrix} \mathbf{K}_a + \mathbf{K}_{aa}^{Z_p} & \mathbf{K}_{am}^{Z_p} \\ 0 & \mathbf{K}_m \end{bmatrix} + j\omega \begin{bmatrix} \mathbf{C}_{a1} + \mathbf{C}_{a2} + \mathbf{C}_a^{Z_{out}} + \mathbf{C}_{aa}^{Z_p} & 0 \\ \mathbf{C}_{ma}^{Z_p} & \mathbf{C}_{mm}^{Z_p} \end{bmatrix} - \omega^2 \begin{bmatrix} \mathbf{M}_a & 0 \\ \mathbf{M}_{ma}^{Z_p} & \mathbf{M}_m \end{bmatrix} \right) \begin{Bmatrix} \tilde{\mathbf{\Phi}}_a \\ \tilde{\mathbf{P}}_m \end{Bmatrix} = \begin{Bmatrix} \mathbf{F}_a^{in} \\ 0 \end{Bmatrix} \ . \tag{3.52}$$

However, in the present study excitation at the inlet section has been modelled by means of Dirichlet boundary conditions, with $\Phi = 1$ on Γ_{in} for simplicity, following [89]. Additionally, $\mathbf{F}_a^{in} = \mathbf{0}$.

3.3. Objective Function: Transmission loss

Acoustic attenuation of the muffler can be measured in terms of Transmission Loss (TL), which is defined as the ratio of the incident power on the noise

control device to the one transmitted through the outlet section (considering an anechoic end). It can be expressed as [13]:

$$TL\left(\boldsymbol{v}\right) = 10\log\left(\frac{\left|P_{in}^{+}\right|^{2} S_{in}\left(1+M_{in}^{2}\right)/\left(2\rho_{in}c_{in}\right)}{\left|P_{out}^{+}\right|^{2} S_{out}\left(1+M_{out}^{2}\right)/\left(2\rho_{out}c_{out}\right)}\right) , \tag{3.53}$$

where P^{+}, S and M denote the amplitude of the progressive wave, the cross-section area of the tube and the Mach number, respectively (subscripts *in* and *out* denote the inlet and outlet sections). By assuming that the inlet and outlet ducts are long enough to avoid three-dimensional effects at Γ_{in} and Γ_{out} (generated at the expansion and contraction of the muffler chamber), plane wave propagation is guaranteed for the frequencies analyzed (up to 3200 Hz), and the progressive wave at the inlet section is $P_{in}^{+} = \left(P_{in} + Z_0 U_{in}\right)/2$, whereas the lack of regressive wave at the outlet tube leads to $P_{out}^{+} = P_{out}$ [87]. Given Eqs. (3.17–3.19), it leads to:

$$P_{in}^{+} = \frac{1}{2}\left(-\rho_{in}\left(j\omega\ \Phi|_{n_1^{in}} + U_{mf}^{in}\left.\frac{\partial\Phi}{\partial x}\right|_{n_1^{in}}\right) + Z_0\left.\frac{\partial\Phi}{\partial x}\right|_{n_1^{in}}\right) , \tag{3.54}$$

$$P_{out}^{+} = -\rho_{out}\left(j\omega\ \Phi|_{n_3^{out}} + U_{mf}^{out}\left.\frac{\partial\Phi}{\partial x}\right|_{n_3^{out}}\right) , \tag{3.55}$$

where n_1^{in} and n_3^{out} are the central nodes of Γ_{in} and Γ_{out}, respectively. The computation of $\partial\Phi/\partial x$ at n_1^{in} and n_3^{out} can be carried out, for example, through the nodal solution of Φ at additional nodes n_2^{in}, n_3^{in}, n_1^{out} and n_2^{out} within the corresponding elements (see Figure 3.4).

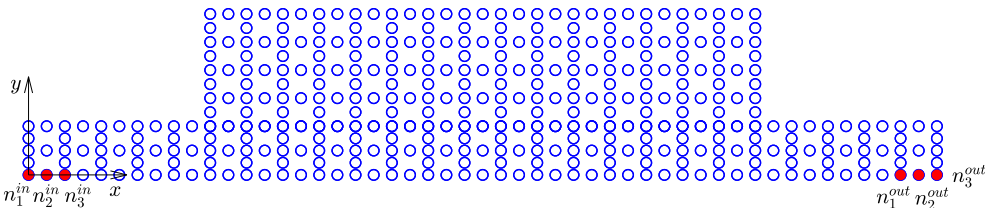

Figure 3.4: Nodes of the finite element mesh of a dissipative muffler.

3.4. Optimization problem

The optimization problem of designing a muffler target frequency to operate in the frequency range $[f_0, f_1]$ can be stated as:

$$\begin{aligned} &\max_{\boldsymbol{\upsilon}} \mathcal{F}_0\left(\tilde{\boldsymbol{\Phi}}_a(\boldsymbol{\upsilon})\right) = \frac{1}{f_1 - f_0}\int_{f_0}^{f_1} TL(\tilde{\boldsymbol{\Phi}}_a(\boldsymbol{\upsilon}), f)\ \mathrm{d}f\ , \\ &\text{subject to: } \mathcal{F}_i\left(\boldsymbol{\upsilon}\right) \leq 0\ , \qquad \text{for } i = 1, ..., M\ , \\ &\qquad\qquad \upsilon_j^{min} \leq \upsilon_j \leq \upsilon_j^{max}, \qquad \text{for } j = 1, ..., N\ , \end{aligned} \tag{3.56}$$

i.e., optimizing a set of N design variables υ_j, in order to maximize the mean TL in the target frequency range, while satisfying the M constraints $\mathcal{F}_i(\boldsymbol{\upsilon})$. Note that $\boldsymbol{\upsilon}$ is a general representation of the design variables. In general, $\boldsymbol{\upsilon}$ contains the bulk densities corresponding to the elements of the chamber. However in Section 3.5.3 it may contain some additional variables such as the dimensions of the dissipative and reactive chambers. A weight W constraint has been included to limit the maximum amount of fibre:

$$\mathcal{F}_1(\boldsymbol{\upsilon}) = W(\boldsymbol{\upsilon}) - W_0 \leq 0\ , \tag{3.57}$$

W_0 being the maximally allowed weight. Simpson's numerical integration rule [90] with frequency spacing Δf of 5 Hz has been used in this study to approximate the integral in (3.56). The optimization problem has been solved at each iteration by the use of the gradient-based MMA [40] recalled in Section 2.3.2.1 due to the high number of design variables. However, it has not been proven that the problem is convex, hence it is not possible to state that the solution reached after meeting the stopping criterion is the optimal design. The computation of the sensitivities of $\mathcal{F}_0$ with respect to a perturbation of the design variables can be sped up (with respect to the finite difference method) by using the standard adjoint method [48] (see Section 2.3.2.2), and no filtering of sensitivities has been performed.

Opposite to standard TO approaches, which look for material-void designs, the proposed method also allows for intermediate values of filling density, since obtaining areas with these filling density values is possible from a manufacturing point of view. Hence intermediate values of ρ_b are not penalized (as via SIMP or RAMP interpolation schemes).

3.5. Results

The acoustic model described in Section 3.2 has been implemented in MATLAB®for the axisymmetric case in order to optimize the density layout of the absorbent material within the dissipative chamber.

Given a muffler geometry, temperature distribution and Mach number at the inlet, computations have been carried out with a view to maximize acoustic attenuation performance in the target frequency range. The TO method described in Section 3.4 is applied below to two different muffler configurations: a dissipative muffler with one chamber and perforated tube, as well as a hybrid muffler containing a dissipative chamber with perforated tube, and a reactive chamber with extended outlet tube. The effect of temperature gradients on the design of the noise control device has been included, as described in Section 3.5.1, as well as the simultaneous design of the density layout and the muffler's geometry given a constant temperature within it.

3.5.1. Temperature distribution

The temperature distribution within the muffler depends on the muffler configuration, as well as the engine load and speed, and affects the sound propagation properties of both the air and fibrous mediums. The effect of the absorbent material filling density on the temperature function has not been included in this study, and therefore temperature can be expressed as a function of position $T = T(x, r)$ at all stages of optimization: a linear axial variation has been assumed along the perforated section $T_{duct}(x)$, whereas temperatures at the inlet T_{in} and outlet tubes T_{out} are considered constant due to their short length with respect to the total length of the muffler, in accordance with reference [15].

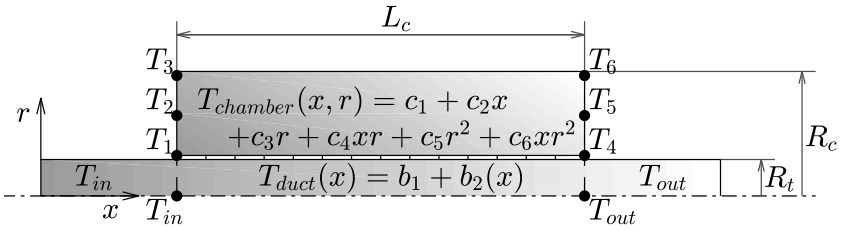

Figure 3.5: Axisymmetric temperature distribution studied.

Regarding the temperature function at the annular chamber, $T_{chamber}(x, r)$, a quadratic variation along the radial direction has been added in order to approximate the logarithmic temperature function through a cylindrical domain. The example cases studied are shown in Table 3.4 [15].

	T_{in}	T_{out}	T_1	T_2	T_3	T_4	T_5	T_6	T_{avg}
Case T-I	25	25	25	25	25	25	25	25	25
Case T-II	300	200	300	235	200	200	135	100	181
Case T-III	181	181	181	181	181	181	181	181	181

Table 3.4: *Definition of the temperature field (°C).*

3.5.2. Multi-frequency topology optimization of a dissipative muffler

The configuration to optimize is shown in Fig. 3.6. The muffler consists of a single dissipative chamber, filled with Owens Corning texturized fibreglass roving [69] (see properties in Table 3.3). Its dimensions are: inner radius $R_t = 0.0268$ m, outer radius $R_c = 0.0886$ m, and chamber length $L_c = 0.3$ m. The perforated duct properties are: thickness $t_p = 0.001$ m, porosity $\sigma = 20\%$, and orifice diameter $d_h = 0.0035$ m.

Ω_a and Ω_m have been meshed using 8-node quadrilateral elements, whose maximum length has been set to 0.005 m (the wavelength of 3200 Hz sounds in the air is 0.108 m at 25°C, i.e., a minimum of 21 elements per wavelength is considered in this study). 780 elements are obtained within Ω_m (therefore, 780 design variables are considered), with maximum and minimum element filling density values set to 50 and 250 kg/m^3 respectively. Initially, a homogeneous filling density of 120 kg/m^3 has been assigned to every finite element

of the chamber, using 0.8066 kg of absorbent material. This initial weight has been defined as the maximum admissible weight: $W_0 = W(\boldsymbol{v}_0)$. Finally, the maximum change in each variable per iteration has been restricted to 10% of the range.

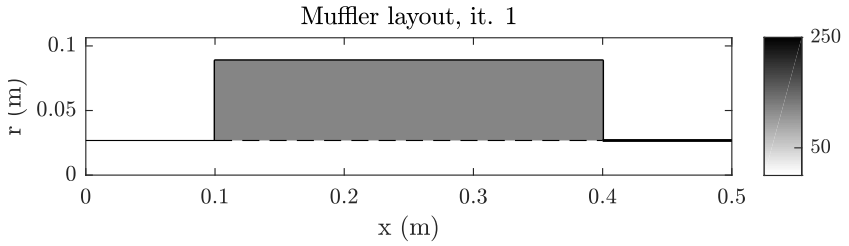

Figure 3.6: Initial design.

3.5.2.1. Design 1. Cold condition optimization. Low frequency range

First, the TO process has been carried out for the case T-I described in Table 3.4 (cold condition). Mach number at the inlet section is 0.05. The target frequency range where TL is to be improved has been set to $[100, 200]$ Hz. The acoustic analysis has been performed by employing 4500 degrees of freedom, and the sensitivities of $\mathcal{F}_0$ have been obtained for each of the 101 frequencies of the Simpson's quadrature, with $\Delta f = 5$ Hz. The MMA method has been then used to optimize the material distribution by using gradient information.

The stopping criterion has been defined as the relative variation (in absolute value) in each design variable being below 1% of its range. Figure 3.7 shows the muffler design after meeting the stopping criterion at iteration 27.

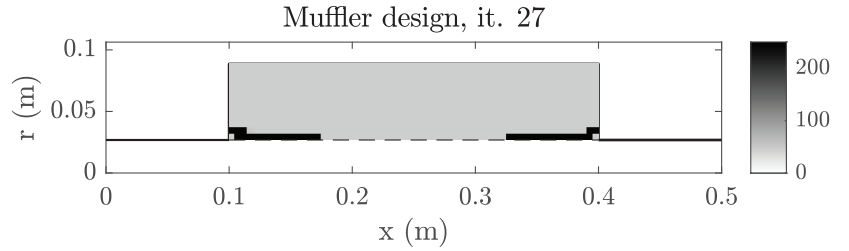

Figure 3.7: Optimized topology. Design 1.

As shown in Figure 3.7, the improved design has the minimum density associated with most of the elements of Ω_m. Therefore the final design uses only 0.3656 kg of absorbent material. In accordance with Selamet *et al.* in [67], a slight improvement in TL at low frequencies can be achieved by using low filling density, even though this may result in a worse attenuation in the rest of the frequency range, as shown in Figure 3.9.

Even if this optimized muffler could be difficult or expensive to manufacture, the TO process yields basic ideas to construct a high-performance manufacturable muffler for these specific working conditions. In particular, optimization indicates the need of including an extended duct.

3.5.2.2. Design 1a. Manufacturable muffler with $\rho_b = 50$ kg/m^3 and extended ducts

Design 1 shown in Figure 3.7 shows maximum density in two thin regions at both sides of the perforated surface. Although Design 1 is difficult to obtain by standard fabrication methods, it can give some guidelines in order to generate new designs. The increase in bulk density up to the maximum value next to the perforated duct tends to form acoustically independent subdomains, similar to an extended duct separating the central passage and the outer chamber. Therefore, it is suggested that Design 1 can be replaced by a muffler with homogeneous minimum filling density in the chamber and duct extensions (Design 1a). Figure 3.8 shows the easily manufacturable design with a homogeneous ρ_b of 50 kg/m^3 and extended ducts of length 0.075 m each, as suggested by Figure 3.7.

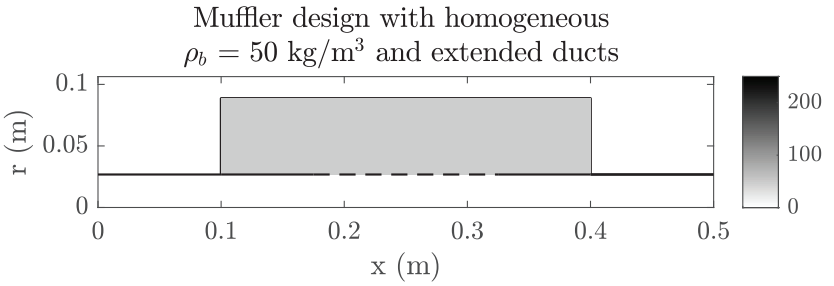

Figure 3.8: Manufacturable design. Design 1a.

3.5.2.3. Results discussion. Designs 1 and 1a

The attenuation performance of the optimized topology shown in Figure 3.7 (Design 1) and the manufacturable muffler shown in Figure 3.8 (Design 1a) are compared with the initial topology. As shown in Figure 3.9, the manufacturable design provides an improvement in terms of TL which is similar to the optimized design in the target frequency range, with respect to the initial design. In addition, both Designs 1 and 1a show worse attenuation with respect to the initial topology, for frequencies out of the attenuation range. The addition of the extended ducts does affect the TL prediction for higher frequencies: the manufacturable design shows better performance up to 1000 Hz with respect to the optimized design, while it provides worse attenuation in the range from 1000 to 3200 Hz.

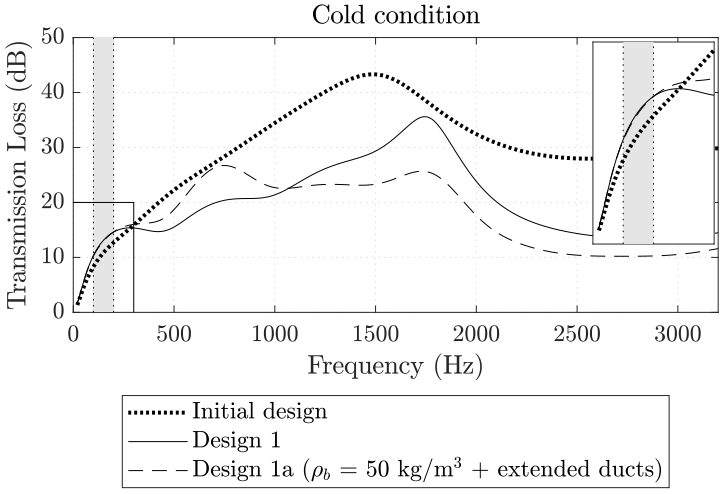

Figure 3.9: TL for the initial and optimized topologies (Design 1 and 1a).

3.5.2.4. Design 2. Cold condition optimization. Mid frequency range

Next, the target frequency range has been switched to $[500, 1000]$ Hz. The TO process is repeated for the same temperature case (T-I in Table 3.4). Figure 3.10 shows an intermediate design of the optimization process, after 9

iterations. At this stage of the process, the design still includes many areas with intermediate values of density.

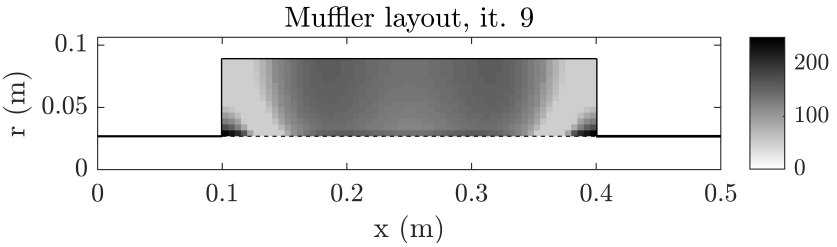

Figure 3.10: Optimized topology. Design 2 at iteration 9.

Figure 3.11 shows that $\mathcal{F}_0$ improves at every iteration, from the starting value of 28.39 dB to 35.65 dB at iteration 43. However, the value of the weight constraint $\mathcal{F}_1$ oscillates until converging to a value near zero. This implies that the optimized design shown in Figure 3.13 (once optimization finishes at iteration 43) uses 0.8066 kg of material, as much as the initial one.

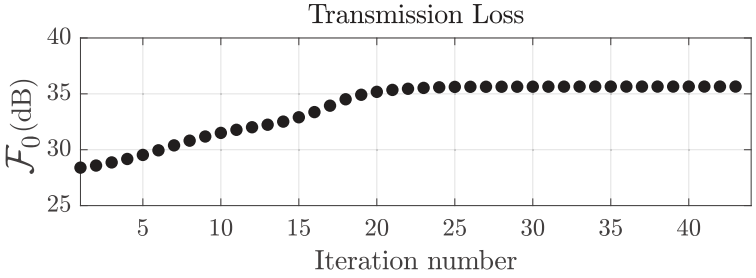

Figure 3.11: Case 2. Evolution of $\mathcal{F}_0(\boldsymbol{v})$.

This suggests that better attenuation at mid frequencies could be obtained by the use of a higher amount of fibrous material, in accordance with reference [67].

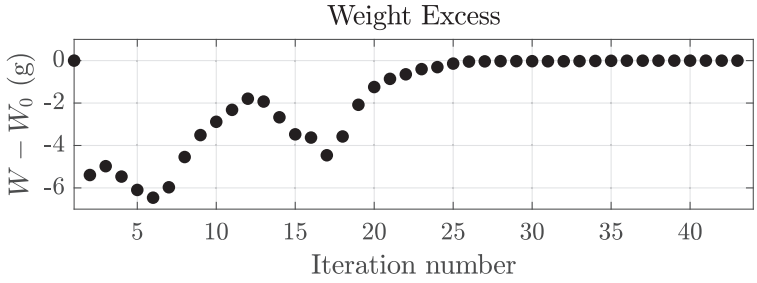

Figure 3.12: Case 2. Evolution of $\mathcal{F}_1(\boldsymbol{v})$.

The resultant design resembling a configuration with five rings with alternating maximum and minimum filling densities [68], is shown in Figure 3.13. As for Design 1 presented in Section 3.5.2.1, TO suggests the use of extended inlet/outlet duct (of 4 elements of length).

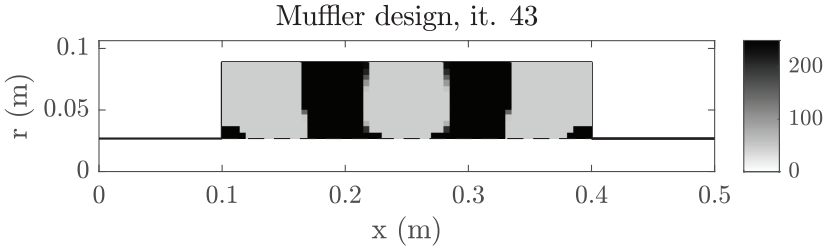

Figure 3.13: Optimized topology. Design 2.

3.5.2.5. Design 2a. Manufacturable muffler with a ring design

Analogously to Case study 1, the optimized topology shown in Figure 3.13 is not easily manufacturable. Additionally, a ring configuration consisting of 5 rings of material with filling densities of 50 and 250 kg/m^3 has been studied, as TO suggests. The rings are 0.065 m and 0.0525 m wide respectively, as shown in Figure 3.14, in order to maintain the amount of dissipative material used.

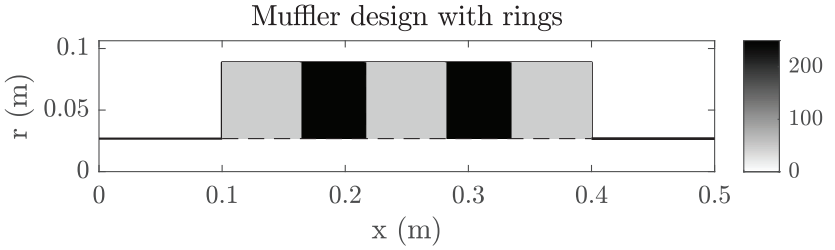

Figure 3.14: Manufacturable design. Design 2a.

3.5.2.6. Design 2b. Manufacturable muffler with a ring design and extended ducts

Design 2 shown in Figure 3.13 includes small regions of dissipative material with high density over both sides of the perforated surface, reducing the acoustic coupling between the subdomains Ω_a and Ω_m in these sections of the tube. Figure 3.10 shows that these areas tend to adopt the maximum bulk density faster than any other region in the chamber. As shown in the literature [77], the use of extended inlet/outlet ducts can help to increase attenuation at certain ranges of frequency. Therefore, an additional design including extended tubes with 0.02 m of length (equal to the axial length of 4 finite elements within Ω_m) has been studied (sketched in Figure 3.15). The acoustic performance provided by Designs 2, 2a and 2b is shown in Figures 3.17 and 3.18, and results are discussed below in this section.

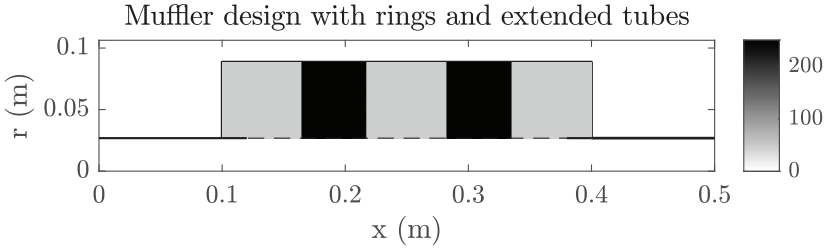

Figure 3.15: Manufacturable design. Design 2b.

3.5.2.7. Design 3. Operating (hot) condition optimization. Middle frequency range

The effect of temperature over the TO process has been studied in this Section. The TL provided by a given muffler can differ substantially when

considering thermal effects. Also, peaks in TL can shift to different frequencies [15, 87, 91]. Additionally, by considering mufflers with large dimensions and fibre volume, high temperature and highly resistive fibres [91], it is likely that the topologies obtained by cold and hot TO could exhibit differences in some cases.

The effect of temperature on the TO process has been studied by considering the operating temperature case T-II described in Table 3.4, while maintaining the frequency range of interest in $[500 - 1000]$ Hz. The initial density distribution is the one used in previous sections (see Fig. 3.6). The improved topology after stopping criterion is met at iteration 39 is plotted in Fig. 3.16.

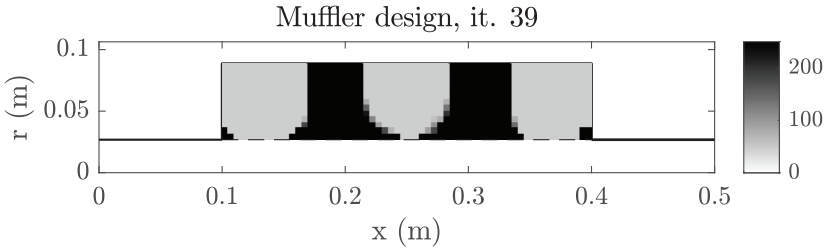

Figure 3.16: Optimized topology. Design 3.

As shown in Figure 3.16, by considering the high-temperature effect, a similar optimized topology to Design 2a (resultant of the cold TO) has been obtained. It consists of 5 rings alternating minimum and maximum ρ_b. The final weight is again 0.8066 kg.

3.5.2.8. Results discussion. Designs 2, 2a, 2b and 3

The initial design as well as Designs 2, 2a, 2b and 3 have been evaluated at the cold temperature case T-I described in Table 3.4. The initial homogeneous topology of 120 kg/m^3 provides a mean TL in the target frequency range of 28.65 dB. As it can be seen in Figure 3.17, the result of TO for the cold working condition (Design 2), shows good acoustic attenuation improvement in terms of TL (35.65 dB). Design 2a, consisting of 5 rings inferred from Design 2, provides a similar mean TL of 34.80 dB. However, Design 2b with rings and extended ducts improves noise mitigation up to 37.02 dB.

This suggests that the small regions with maximum ρ_b that appear at both sides of the perforated surface have a physical meaning: the algorithm increases filling density in these small areas in order to reduce the acoustic coupling between the duct and the chamber in these regions of the perforated duct, similar to duct extensions. As shown in Figure 3.10, at iteration 9 of the TO, these small regions already show maximum ρ_b, whereas the rest of the finite elements within Ω_m are associated with intermediate filling densities. Therefore, removing the acoustic coupling at these regions by means of extended ducts increases attenuation in the problem under analysis. Finally, Design 3 shows worse attenuation than Design 2 at target frequencies (mean TL of 35.12 dB). Nonetheless, the differences in material performance observed in the literature [85, 91] can justify the use of the complete model, which considers thermal effects.

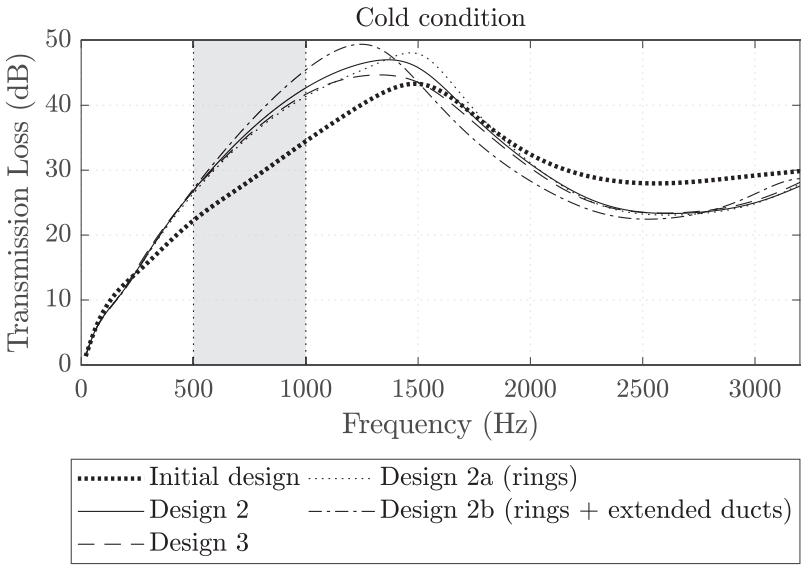

Figure 3.17: TL for the initial and optimized topologies. Designs 2, 2a, 2b and 3.

On the other hand, the topologies obtained with the different working conditions have been tested considering the high temperature field T-II defined in Table 3.4. Results are shown in Figure 3.18. The initial topology with uniform ρ_b of 120 kg/m^3 provides a mean TL at the target frequency range of 27.65 dB. Design 2, resultant of the cold TO (case T-I of Table 3.4), provides a mean TL of 36.72 dB in the target frequency range.

Design 3, obtained by considering T-II temperature case, provides a good improvement in TL in the target frequency range, up to 37.35 dB. This proves that higher attenuation can be achieved with the same amount of material, by considering the appropriate operating conditions. Figure 3.18 shows a peak in attenuation with 60 dB at around 1200 Hz for this last design.

Design	Description	mean TL (cold eval.) [dB]	mean TL (hot eval.) [dB]
Initial	$\rho_b = 120$ kg/m^3	28.65	27.65
2	Cold (T-I) TO	35.65	36.72
2a	Rings	34.80	35.30
2b	Rings + ext. ducts	37.02	37.42
3	Hot (T-II) TO	35.12	37.35

Table 3.5: *Results summary. TL evaluation for the range* $[500, 1000]$ *Hz.*

Design 2a, consisting of rings, shows a mean TL of 35.30 dB, which is worse than Designs 2 and 3, but still better than the initial design. However, the addition of the extended ducts improves the mean TL up to 37.42 dB, however, their length is larger than the length suggested by Design 3 (see Figure 3.16).

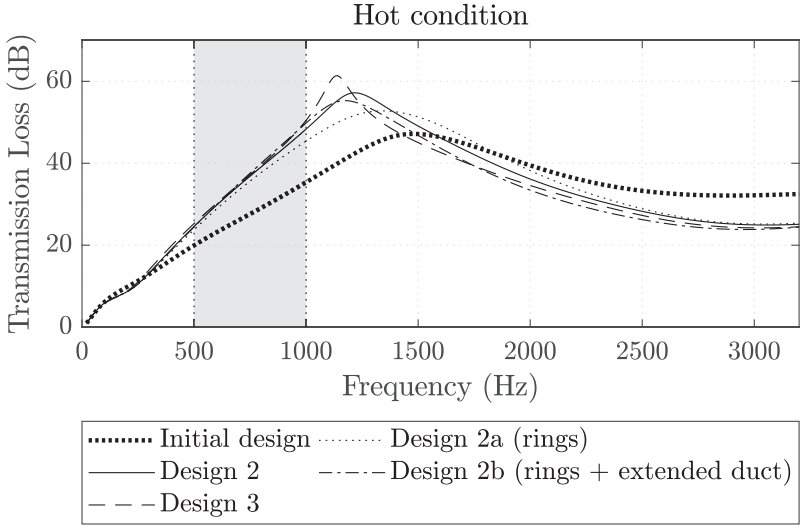

Figure 3.18: TL for the initial and optimized topologies. Designs 2, 2a, 2b and 3.

For both cold and hot evaluations, all the optimized designs show worse TL than the initial design from around 1500 to 3200 Hz, proving that optimization in one range of frequencies can lead in some cases to worse attenuation at other frequencies.

3.5.3. Multi-frequency shape optimization of a hybrid muffler with multiple constraints

3.5.3.1. Design 4. Broad frequency range

A hybrid muffler, which consists of a dissipative chamber and a reactive one with an extended outlet duct, has been considered in this Section in order to maximize the attenuation in a wide range of frequencies. A baffle with 0.005 m in thickness has been added between both chambers. In order to obtain potentially manufacturable designs, and taking into account the optimized topology obtained in previous cases, 5 annular rings with constant filling density have been defined, each one containing several elements of the FE mesh, hence reducing the number of design variables.

The dimensions of these rings have also been considered design variables v_j, as shown in Figure 3.19. The maximum and minimum values of each design variable can be checked in Table 3.6. The sensitivities of $\mathcal{F}_0$ with respect to these dimensions are also required at each iteration. Temperature gradients are neglected in this case for simplicity, and the operating uniform-temperature case T-III, detailed in Table 3.4, has been considered. The target frequency range has been set to $[500, 2000]$ Hz.

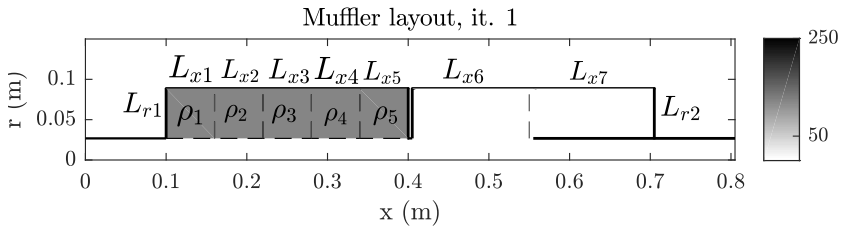

Figure 3.19: Initial design and design variables.

The model has been meshed in a similar way to the dissipative muffler, 8146 nodes have been obtained. Additional constraints have been added in

this case in order to keep the muffler under 1 m in length and both chambers with the same radii. The mean Mach number at the inlet has been set to zero. The optimization has stopped after 22 iterations producing the result shown in Figure 3.20.

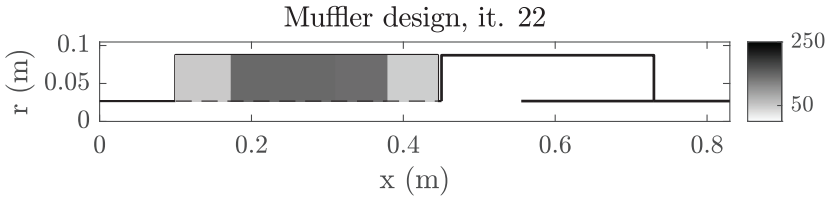

Figure 3.20: Optimized topology. Design 4.

3.5.3.2. Results discussion. Design 4

Figure 3.20 shows the optimized design. The left dissipative chamber contains two lateral rings with minimum ρ_b and three central rings with around 150 kg/m^3. This chamber resembles the muffler configuration with two short lateral chambers and a central dissipative region, already studied in reference [92]. Also, an overall length increase of the dissipative chamber has been observed, increasing the perforated surface length (and hence the area of acoustic coupling). The reactive chamber has decreased in length while containing a longer extended tube. Results are shown in detail in Table 3.6. The optimized design uses 0.8054 kg of absorbent material, and both additional constraints are satisfied (the muffler length is 0.838 m and both chambers have the same radius, 0.0872 m).

The mean TL increase along the range of frequencies under study can be checked in Figure 3.21. The optimized design shows higher mean attenuation in the target frequency range (63.84 dB) than the initial design (56.31 dB), although it might be lower at some specific frequencies. Also, the peaks in TL shift to the left in Figure 3.21 as a result of the increase in the extended duct length.

v_j	v_j^{min}	v_j^{max}	v_j^0	v_j^{opt}
ρ_1 (kg/m^3)	50	250	120	51.07
ρ_2 (kg/m^3)	50	250	120	145.81
ρ_3 (kg/m^3)	50	250	120	148.27
ρ_4 (kg/m^3)	50	250	120	141.17
ρ_5 (kg/m^3)	50	250	120	50.00
L_{x1} (m)	0.0420	0.7800	0.0600	0.0733
L_{x2} (m)	0.0420	0.7800	0.0600	0.0686
L_{x3} (m)	0.0420	0.7800	0.0600	0.0685
L_{x4} (m)	0.0420	0.7800	0.0600	0.0685
L_{x5} (m)	0.0420	0.7800	0.0600	0.0664
L_{r1} (m)	0.0433	0.0803	0.0618	0.0604
L_{x6} (m)	0.1050	0.1950	0.1500	0.1050
L_{x7} (m)	0.1050	0.1950	0.1500	0.1747
L_{r2} (m)	0.0433	0.0803	0.0618	0.0604

Table 3.6: *Optimization summary. Design parameter v_j, minimum v_j^{min} and maximum v_j^{max} limits, initial v_j^0 and optimized v_j^{opt} values. Design 4.*

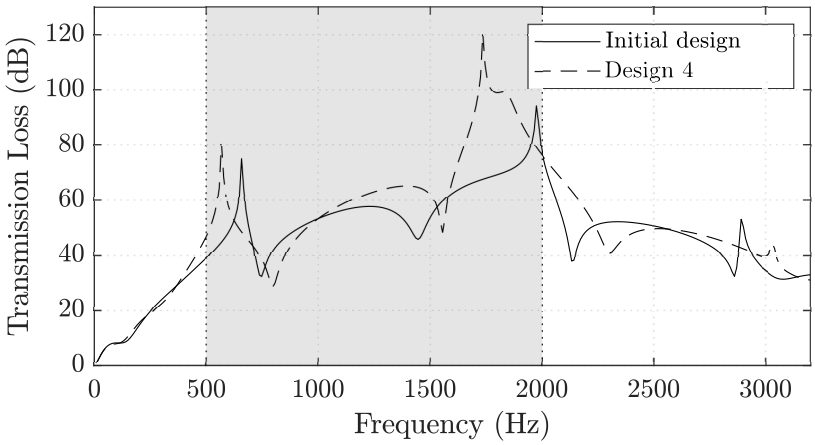

Figure 3.21: TL for the initial and optimized designs. Design 4.

3.6. Conclusions

This Chapter presents a combination of geometry and topology optimization methods to effectively increase the attenuation of dissipative and hybrid mufflers at certain frequency ranges.

The evaluation of the TL has been performed using a FE hybrid acoustic model valid for mufflers with heterogeneous absorbent material layout and perforated duct, in the presence of mean flow and temperature gradients. The optimization problem has been solved by the use of the iterative algorithm MMA, which requires the gradient of both the objective function and the restrictions with respect to all design variables at each design step. The adjoint method, along with the analytical derivation of the global matrices with respect to each design variable, allows for calculating efficiently the sensitivities of the objective function.

For low frequencies, TO results in a reduction of the amount of dissipative material used in the dissipative chamber and a slight improvement in TL at target frequencies, which can worsen the acoustic behaviour at mid to high frequencies. Regarding the optimization at mid frequencies, the optimization scheme has been set up for two case studies with different thermal gradients, obtaining the optimized absorbent material layout in each case. Although little discrepancy in the optimized material distribution has been observed, results show the importance of considering temperature in the optimization process. The proposed methodology is able to provide a predesign for building manufacturable mufflers. These have been inferred from the topologies proposed by the optimization algorithm and keep most of the improvement in acoustic performance at target frequencies. This fact enables the proposed methodology to be a powerful tool for engineers and designers to build efficient mufflers for practical applications.

Finally, an optimization of a hybrid muffler has been carried out. The density layout obtained from the previously optimized dissipative mufflers has been combined with the shape optimization of the reactive chamber and the size of the dissipative rings. The optimization has also been carried out by using the MMA. Significant TL increase at target frequencies has been achieved in every case under study.

Chapter 4

Acoustic optimization of exhaust aftertreatment devices

In this Chapter, the existing modelling techniques for the acoustic behaviour of exhaust devices including monoliths, such as catalytic converters (CC) and diesel particulate filters (DPF), have been recalled. Taking advantage of the fact that, in many cases, these aftertreatment devices have an arbitrary but axially-uniform cross section, a hybrid numerical-analytical approach has been reviewed in order to efficiently simulate their acoustic behaviour via modal expansion, which has a notable effect on the global TL provided by the exhaust system.

The mode matching (MM) method allows the efficient evaluation of the sound attenuation performance through TL computation. This method is based on the decomposition of the acoustic pressure field into a set of transversal and axial modes within each subdomain. First, the transversal modes have been solved through a 2D FEM approoach, whereas axial compatibility conditions of the acoustic fields within the device have been later applied analytically.

Finally, a GA-based optimization scheme has been set-up in order to determine the best configuration of several devices with different working requirements, including the optimization of the lengths and cross section of the lengths and geometry of the chambers involved, the type of monolith, as well as the location of the inlet and outlet ducts.

4.1. Introduction

As expressed in Section 1.1, air pollutants produced by internal combustion engines, such as unburned hydrocarbons (HC), carbon monoxide (CO), nitrogen oxides (NOx) and particulate matter (PM) [8, 93], are a major environmental problem in most of today's cities. The actual environmental regulations have made the use of CC and DPF to become widespread in the automotive industry. Although the use of these aftertreatment devices is based on environmental reasons, they have an effect on the exhaust system's overall attenuation, and their acoustic performance should be hence evaluated.

Meanwhile, whereas the acoustic modelling of CC and DPF has been addressed [17, 94–99], their acoustic optimization appears not to have been addressed previously in the literature. In this Chapter, a genetic algorithm has been applied to the former acoustic model [99] in order to perform not only a longitudinal sizing optimization of the chamber and the monolith, but also the arbitrary cross section (given a predefined shape) and the position of the inlet and outlet ducts, with a view to maximizing the TL.

4.2. Acoustic modelling of aftertreatment devices

Figure 4.1 shows a simplified scheme of an exhaust aftertreatment device. It is composed by two inlet and outlet cylindrical ducts and the main chamber that contains the monolith (CC or DPF). In the case under study, the configuration has an arbitrary axially-uniform cross section [17, 87, 100].

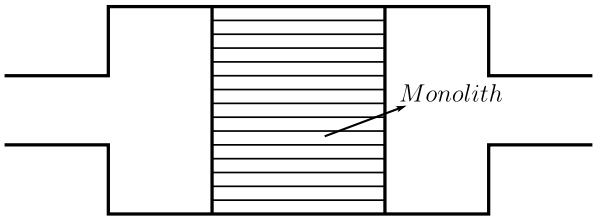

Figure 4.1: Scheme of an automotive exhaust device with monolith.

This allows for the modal expansion method to be used [17,87,100], where for each duct, the acoustic pressure solution can be obtained by means of the superposition of evanescent and propagating transversal pressure modes. Additionally, sound propagation within the monolith can be replaced by a four-pole transfer matrix, which relates the acoustic fields of both the inlet and outlet sections of the monolith. This is in agreement with the actual acoustic phenomena taking place within the long capillary ducts. Further information can be found in the works [96–98].

Subsections 4.2.1 and 4.2.2 are dedicated to the acoustic characterization of the monolith (CC and DPF) via four-pole transfer matrices.

4.2.1. Catalytic converter

A catalytic converter usually consists of an expansion, a monolith and a contraction prior to the exhaust muffler(s), as shown in Figure 4.2a. The catalyst substrate is composed of multiple cells which have a density from $5 \cdot 10^5$ up to 10^6 capillaries per square meter [96].

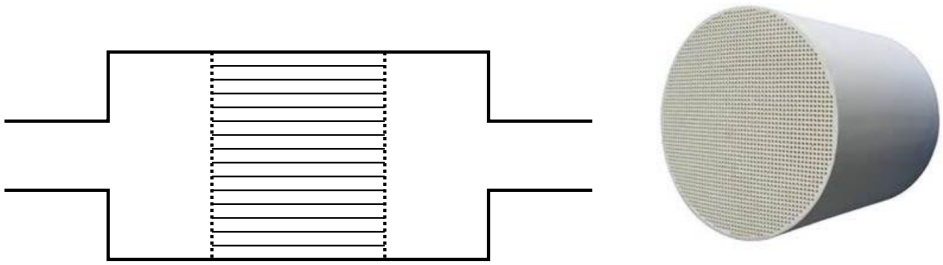

(a) Simplified view. **(b)** Monolith.

Figure 4.2: Catalytic converter

4.2.1.1. 1-D acoustic modelling of the monolith

The acoustic modelling of the monolith involves the consideration of viscosity and heat transfer effects. In the present Thesis, the model introduced by Allard [22] has been used in absence of mean flow. This model was successfully applied by Selamet *et al.* [96]. Resistivity R is used here as the principal factor in order to characterize the monolith. On the other hand, the model developed by Dokumaci can be used in presence of mean flow, and the reader is referred to [94, 101] for its derivation.

In absence of mean flow, a set of capillaries can be acoustically modelled by means of the equivalent density and speed of sound [22]. Both parameters are complex, frequency-dependent, and can be expressed as a function of resistivity R. By taking into account viscous and heat transfer effects, continuity, dynamic equilibrium and energy equations are [102]:

$$\frac{\partial \rho_m}{\partial t} + \rho_0 \nabla \mathbf{u}_m = 0 \ , \tag{4.1}$$

$$\nabla p_m + \rho_0 \frac{\partial \mathbf{u}_m}{\partial t} - \mu \left(\nabla^2 \mathbf{u}_m + \frac{1}{3} \nabla \left(\nabla \mathbf{u}_m \right) \right) = 0 \ , \tag{4.2}$$

$$\frac{\partial T_m}{\partial t} - \frac{1}{\rho_0 C_p} \frac{\partial p_m}{\partial t} = \frac{\kappa}{\rho_0 C_p} \nabla^2 T_m \ , \tag{4.3}$$

ρ_0 and ρ_m being the air density and the equivalent density within the monolith, κ the thermal conductivity, C_p the specific heat at constant pressure, and μ the viscosity. Subscript m denotes the acoustic variables within the monolith.

After assuming a fully developed laminar flow along the capillaries (their transversal dimensions are significantly small with respect to their length and the wavelength) [95], Eq. (4.2) can be rewritten as:

$$\nabla p_m + \rho_0 \frac{\partial \mathbf{u}_m}{\partial t} + \mathscr{R}\mathbf{u}_m = 0 \ , \tag{4.4}$$

and a harmonic solution $\mathbf{u}_m = \mathbf{U}_m e^{j\omega t}$ is assumed, yielding:

$$\nabla p_m + \rho_m \frac{\partial \mathbf{u}_m}{\partial t} = 0 \ , \tag{4.5}$$

the equivalent density ρ_m being:

$$\rho_m = \rho_0 + \frac{\mathscr{R}}{j\omega} \ , \tag{4.6}$$

where $\mathscr{R}$ depends on the frequency and on the cross section of the capillary, and can be calculated as [22]:

$$\mathscr{R} = R\phi G_c\left(s\right) \ , \tag{4.7}$$

where R and ϕ are the stationary resistance and the monolith's porosity. Function G_c is defined as:

$$G_c\left(s\right) = \frac{-\frac{s}{4}\sqrt{-j}\frac{J_1\left(s\sqrt{-j}\right)}{J_0\left(s\sqrt{-j}\right)}}{1 - \frac{2}{s\sqrt{-j}}\frac{J_1\left(s\sqrt{-j}\right)}{J_0\left(s\sqrt{-j}\right)}} \ , \tag{4.8}$$

J_0 and J_1 being the zeroth-order and first order Bessel functions of the first kind, respectively. On the other side, s is the tangential wavenumber, which can be expressed as:

$$s = \alpha\sqrt{\frac{8\omega\rho_0}{R\phi}} \ , \tag{4.9}$$

where α in Eq. (4.9) depends on the capillary's cross section shape. Table 4.1 shows the value of α for several capillary section's geometries [99].

Cross-section	α
Circle	1
Square	1.07
Equilateral triangle	1.14
Rectangle	0.78

Table 4.1: *Value of α for different capillary cross section's shape.*

The equivalent speed of sound c_m can be obtained from the equivalent density ρ_m and bulk modulus K_m, defined as [22]:

$$K_m = \frac{\gamma P_0}{\gamma - (\gamma - 1)\, F} \ , \tag{4.10}$$

γ and P_0 being the specific heat ratio and the mean environment pressure, and F being defined by:

$$F = \frac{1}{1 + \dfrac{R\phi}{jPr\ \omega\rho_0} G_c\left(\sqrt{Pr}\ s\right)} \ , \tag{4.11}$$

where the Prandtl number is $Pr = \mu C_p/\kappa$. Finally, c_m can be expressed as:

$$c_m = \sqrt{\frac{K_m}{\rho_m}} = \frac{c_0}{\sqrt{\left(1 + \dfrac{R\phi}{j\omega\rho_0} G_c\left(s\right)\right)\left(\gamma - (\gamma - 1)\, F\right)}} \ , \tag{4.12}$$

where $c_0 = \sqrt{\gamma P_0/\rho_0}$.

Once the monolith is characterized by means of c_m and ρ_m, plane wave models can be used with a view to replace the monolith by a four-pole transfer matrix, in a similar way to Section 2.1.5.2. For a monolith of longitude L_m, it yields:

$$\begin{Bmatrix} P_1 \\ U_1 \end{Bmatrix} = \begin{bmatrix} \cos\left(k_m L_m\right) & jZ_m \sin\left(k_m L_m\right) \\ \dfrac{j}{Z_m} \sin\left(k_m L_m\right) & \cos\left(k_m L_m\right) \end{bmatrix} \begin{Bmatrix} P_2 \\ U_2 \end{Bmatrix} \ , \tag{4.13}$$

where the equivalent wavenumber and characteristic impedance are $k_m = \omega/c_m$ and $Z_m = \rho_m c_m$, respectively, and subscripts 1 and 2 denote the inlet and outlet sections. The four-pole matrix presented in Eq. (4.13) is of great importance in this Chapter and has been used later in Eq. (4.40) of Section 4.2.4.2 when considering catalytic converters.

4.2.2. Diesel particulate filters

Diesel particulate filters (DPF) are commonly used on the exhaust line to reduce the harmful emissions of soot particles. Due to their characteristics,

they also affect the overall acoustic behaviour of the exhaust system.

As Figure 4.3a shows, DPF capillaries are characterized by channel ends alternatively plugged to force the flow through the porous walls. The air enters an inflow channel, which is closed at the outlet, hence being forced to pass through the porous walls of the filter to the four outflow neighbouring channels, which are open downstream. In order to increase the amount of soot it can absorb, the DPF unit is placed within a chamber, which allows to increase its size. Moreover, for typical engines a regeneration is needed each 500-1000 km in order to prevent the soot layer to create an undesired high back-pressure, what increases fuel consumption [97].

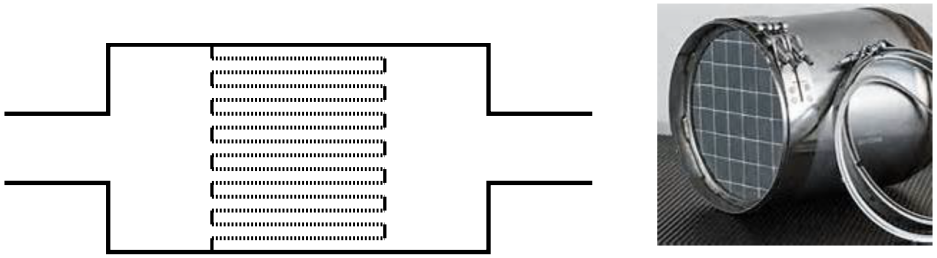

(a) Simplified view. **(b)** Filter element.

Figure 4.3: Diesel particulate filter.

The model used throughout this Thesis for the modelling of the DPF has been the one developed by Allam and Åbom [97], which has been recalled in Sections 4.2.2.1 – 4.2.2.3. This method described the DPF as a system of coupled channels carrying plane waves. It also assumes that the mean Mach number is small ($M_{mf} < 0.1$), and neglects the temperature and mean flow speed gradients in the axial direction, as well as the chemical reaction effects. The coupling through the porous walls is described via the Darcy's law [102].

4.2.2.1. The 1-D wave model

According to Fig. 4.4, a DPF unit cell can be divided into 5 sections: the inlet cross section (IN), a first short region with impermeable walls (I), the filter area with porous walls (II), another short impermeable duct (III), and the outlet cross section (OUT) [97]. In the plane wave range, each section can be modelled via two-port transfer matrices $\mathbf{T}$. The resulting transfer matrix

is:

$$\mathbf{T}_{DPF} = \mathbf{T}_{IN}\mathbf{T}_{I}\mathbf{T}_{II}\mathbf{T}_{III}\mathbf{T}_{OUT} \ , \tag{4.14}$$

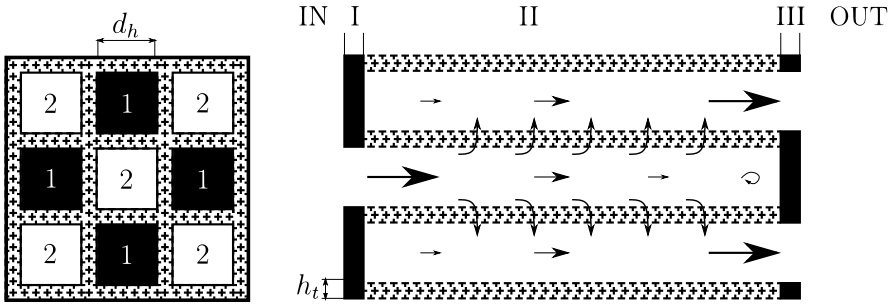

Figure 4.4: Cross-section of the DPF cells. Flow path through the filter.

4.2.2.2. The in- and oulet sections (IN+I and III+OUT)

According to Eq. (4.14), two-port models are also needed for the short straight pipe sections (I and III). Since their length is very small, they can be modelled as an additional mass plug (end correction) to the inlet and outlet sections (IN and OUT) [98]. A lumped impedance model can be used, as proposed in Reference [97]:

$$\mathbf{T}_X = \begin{bmatrix} 1 & Z_X \\ 0 & 1 \end{bmatrix} \ , \tag{4.15}$$

where $X =$ IN+I or III+OUT, and the associated lumped impedance is defined as:

$$Z_x = r_x + jY_X = r_x + \frac{j\rho_X \omega l_X}{d_h^2 N} \ , \tag{4.16}$$

r_X and Y_X being the acoustic resistance and the mass plug impedance, and l_X and N being the end correction and the number of open channels [97]. By considering conservation of energy at the inlet, and conservation of momentum at the outlet (due to flow separation) [13,25], the following expressions for Z_X are obtained [98]:

$$Z_X = \begin{cases} Z_{IN} M_{IN} \left(1/m_{IN}^2 - 1\right) + jY_I \ , \\ 2Z_{OUT} M_{OUT} \left(1 - 1/m_{OUT}\right) + jY_{III} \ , \end{cases} \tag{4.17}$$

where $Z_{IN} = \rho_{IN} c_{IN}/A_{IN}$, $Z_{OUT} = \rho_{OUT} c_{OUT}/A_{OUT}$, and m_{IN} and m_{OUT} are the open area ratios at the inlet and outlet, respectively.

4.2.2.3. The filter section (II)

The continuity (2.1) and momentum (2.3) equations can be linearized in 1-D for a DPF cell, assuming a homogeneous mean flow, yielding [103]:

$$\frac{\partial \rho_j}{\partial t} + U_j^{mf}\frac{\partial \rho_j}{\partial x} + \rho_{0j}\frac{\partial u_j}{\partial x} = (-1)^j \frac{4\rho_w}{d_{hj}} u_w \ , \tag{4.18}$$

$$\rho_{0j}\left(\frac{\partial}{\partial t} + U_j^{mf}\frac{\partial}{\partial x}\right) u_j = -\frac{\partial p_j}{\partial x} - \alpha_j u_j \ , \tag{4.19}$$

where $j = \{1, 2\}$ refer to the inflow and outflow channels of square cross section (see Figure 4.4), U^{mf}, u_w and ρ_w are the time-average flow speed along the capillary, the particle velocity fluctuation through the wall and the gas density at the wall, whereas the pressure drop factor is defined as $\alpha_j = \mu\varepsilon/d_h^2$, where μ is the dynamic viscosity and ε is the channel pressure drop factor [97].

On the other hand, the steady-state flow resistance R_w is defined by the Darcy's law:

$$R_w = \frac{\mu_w h_t}{\sigma_w} \ , \tag{4.20}$$

where σ_w and μ_w is the permeability of the wall and the dynamic viscosity of the fluid. R_w can be used to relate the acoustic fields:

$$R_w u_w = (p_1 - p_2) \ . \tag{4.21}$$

A fluctuating solution $(e^{j\omega t})$ to the problem defined in Eqs. (4.18) and (4.19) is assumed, whose amplitudes are:

$$P_j(z) = \hat{P}_j e^{-jKz} \ , \quad U_j(z) = \hat{U}_j e^{-jKz} \ , \tag{4.22}$$

$$\hat{P}_j = c_j^2 \hat{\rho}_j \ , \qquad \hat{P}_j = Z_j \hat{U}_j \ , \tag{4.23}$$

where $\hat{\cdot}$ denote complex variables, whereas K, c and Z represent the wavenumber, speed of sound and wave impedance inside the channels. Further manipulation of Eqs. (4.18) and (4.19) yields a system of differential equations [97], whose eigenvalue solution is:

$$\begin{Bmatrix} P_1(z) \\ P_2(z) \end{Bmatrix} = \sum_{n=1}^{4} \hat{a}_n e^{-jK_n z} \mathbf{e}_n \ , \tag{4.24}$$

where for each mode $n = 1, 2, 3, 4$, $\hat{a}_n$ and $\mathbf{e}_n$ are the modal amplitudes and eigenvectors corresponding to the free wave of wavenumber K_n. Additionally,

the volume flow can be expressed as:

$$\begin{Bmatrix} Q_1(z) \\ Q_2(z) \end{Bmatrix} = \sum_{n=1}^{4} \hat{a}_n e^{-jK_n z} \mathbf{e}'_n \ , \tag{4.25}$$

where $\mathbf{e}'_n = \mathbf{e}_n d_h^2 / Z_{j,n}$. For the no flow case $U_1^{mf} = U_2^{mf} = 0$, the solution can be found analytically, yielding [97]:

$$K_1 = -K_2 = k \ , \qquad \mathbf{e}_1 = \mathbf{e}_2 = \begin{Bmatrix} 1 \\ 1 \end{Bmatrix} \ , \tag{4.26}$$

$$K_3 = -K_4 = k\sqrt{1 - 8jB/k} \ , \quad \mathbf{e}_3 = \mathbf{e}_4 = \begin{Bmatrix} 1 \\ -1 \end{Bmatrix} \ , \tag{4.27}$$

with $B = c\rho_w / (d_{hj} R_w)$. By defining matrix $\mathbf{H}(z)$ as:

$$\begin{Bmatrix} P_1(z) \\ P_2(z) \\ Q_1(z) \\ Q_2(z) \end{Bmatrix} = \mathbf{H}(z) \begin{Bmatrix} \hat{a}_1 \\ \hat{a}_2 \\ \hat{a}_3 \\ \hat{a}_4 \end{Bmatrix} = \begin{bmatrix} e^{-jK_1 z}\mathbf{e}_1 & e^{-jK_2 z}\mathbf{e}_2 & e^{-jK_3 z}\mathbf{e}_3 & e^{-jK_4 z}\mathbf{e}_4 \\ e^{-jK_1 z}\mathbf{e}'_1 & e^{-jK_2 z}\mathbf{e}'_2 & e^{-jK_3 z}\mathbf{e}'_3 & e^{-jK_4 z}\mathbf{e}'_4 \end{bmatrix} \begin{Bmatrix} \hat{a}_1 \\ \hat{a}_2 \\ \hat{a}_3 \\ \hat{a}_4 \end{Bmatrix} , \tag{4.28}$$

p and q at the inlet of the filter section can be related with those at the outlet via the four-port matrix $\mathbf{S} = \mathbf{H}(0)\mathbf{H}^{-1}(L)$:

$$\begin{Bmatrix} P_1(0) \\ P_2(0) \\ Q_1(0) \\ Q_2(0) \end{Bmatrix} = \mathbf{S} \begin{Bmatrix} P_1(L) \\ P_2(L) \\ Q_1(L) \\ Q_2(L) \end{Bmatrix} \ . \tag{4.29}$$

Finally, by applying the rigid wall boundary condition at the corresponding plugged side of each channel, $Q_1(L) = Q_2(0) = 0$, the transfer matrix corresponding to one DPF unit is obtained:

$$\begin{Bmatrix} P_1(0) \\ Q_1(0) \end{Bmatrix} = \mathbf{T} \begin{Bmatrix} P_2(L) \\ Q_2(L) \end{Bmatrix} = \begin{bmatrix} S_{12} - S_{42}S_{11}/S_{41} & S_{14} - S_{44}S_{11}/S_{41} \\ S_{32} - S_{42}S_{31}/S_{41} & S_{34} - S_{44}S_{31}/S_{41} \end{bmatrix} \begin{Bmatrix} P_2(L) \\ Q_2(L) \end{Bmatrix} . \tag{4.30}$$

With a view to obtaining the transfer matrix of the whole filter $\mathbf{T}_{II}$ (see Eq. (4.14)), the volume flows of all channels NQ_1 and NQ_2 should be considered. It yields:

$$\mathbf{T}_{II} = \begin{bmatrix} T_{11} & T_{12}/N \\ NT_{21} & T_{22} \end{bmatrix} \ . \tag{4.31}$$

The four-pole matrix presented in Eq. (4.14) is of great importance in this Chapter and has been used later in Eq. (4.40) of Section 4.2.4.2 when considering diesel particulate filters.

4.2.3. Modal expansion method

As aforementioned, in this study only uniform cross section devices have been considered [17, 87, 100]. In Figure 4.5, a device is presented containing an axially-uniform cross section.

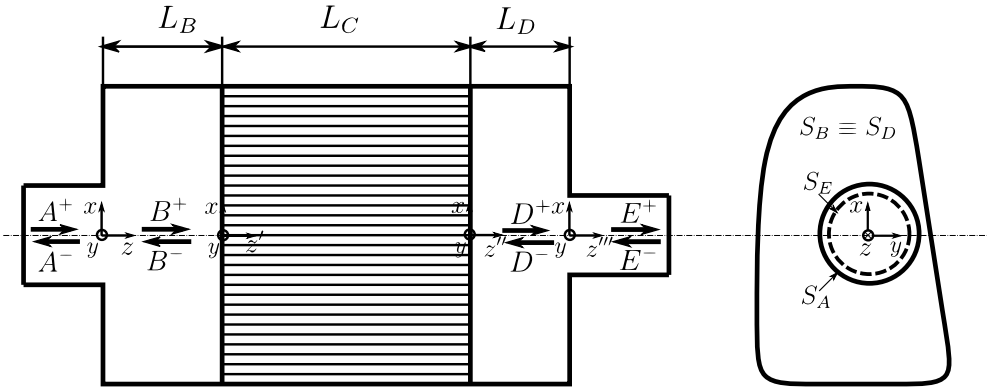

Figure 4.5: Scheme of an exhaust aftertreatment device with a monolith inside the chamber.

Thus, the sound propagation inside the rigid-wall inlet duct A (and analogously the rest of ducts and chambers) can be expressed in terms of the following modal expansion [13, 78, 100]:

$$P_A(x,y,z) = \sum_{n=1}^{\infty} \left(A_n^+ e^{-jk_{A,n}z} + A_n^- e^{jk_{A,n}z} \right) \psi_{A,n}(x,y) \ , \tag{4.32}$$

$$U_A(x,y,z) = \frac{1}{\rho_0 \omega} \sum_{n=1}^{\infty} k_{A,n} \left(A_n^+ e^{-jk_{A,n}z} - A_n^- e^{jk_{A,n}z} \right) \psi_{A,n}(x,y) \ , \tag{4.33}$$

where $\psi_{A,n}$ are the transversal pressure modes of the cross section S_A, A_n^+ and A_n^- are the complex amplitudes of the progressive and regressive waves (unknowns of the problem) respectively, and $k_{A,n}$ the corresponding wavenumber for each mode. Expressions for the acoustic pressure and velocity can be obtained for ducts B, D and E analogously to Eqs. (4.32) and (4.33).

4.2.4. Mode matching technique

4.2.4.1. Mode matching at the device expansion

Regarding the geometric expansion between ducts A and chamber B, continuity of acoustic pressure and axial velocity is imposed. The following relations are satisfied:

$$P_A(x,y,z=0) = P_B\left(x,y,z'=-L_B\right) \quad (x,y) \in S_A \ , \tag{4.34}$$

$$U_A(x,y,z=0) = U_B\left(x,y,z'=-L_B\right) \quad (x,y) \in S_A \ . \tag{4.35}$$

The rigid wall boundary condition is applied at the left plate of the chamber, with zero axial velocity:

$$U_B\left(x,y,z'=-L_B\right) = 0 \quad (x,y) \in S_B - S_A \ . \tag{4.36}$$

A weighted integration of Eqs. (4.34) and (4.35) is performed, using the transversal pressure modes as the weight functions. Note that expressions for the acoustic pressure and velocity defined in Eqs. (4.32) and (4.33) are truncated by using a number N_A of transversal modes within the inlet duct, N_M for the chamber's cross section, and N_E at the outlet duct.

Multiplying Eq. (4.34) by each mode $\psi_{A,i}$, and integrating over the cross section, it yields:

$$\int_{S_A} P_A\left(x,y,z=0\right)\psi_{A,i}\left(x,y\right)\ \mathrm{d}S = \int_{S_A} P_B\left(x,y,z'=-L_B\right)\psi_{A,i}\left(x,y\right)\ \mathrm{d}S \ . \tag{4.37}$$

Applying the aforementioned truncation, as well as the orthogonality properties of the transversal modes ($\int_{S_A}\psi_{A,i}\psi_{A,j}\ \mathrm{d}S = 0$, for $i \neq j$) [100], N_A equations of the following form are obtained:

$$\left(A_i^+ + A_i^-\right)\int_{S_A}\psi_{A,i}^2\left(x,y\right)\ \mathrm{d}S = \sum_{n=1}^{N_M}\left[\left(B_n^+ e^{-jk_{B,n}(-L_B)} + B_n^- e^{jk_{B,n}(-L_B)}\right)\int_{S_A}\psi_{B,n}\left(x,y\right)\psi_{A,i}\left(x,y\right)\ \mathrm{d}S\right] \ , \quad \text{for } i = 1,...,N_A \ . \tag{4.38}$$

Next, Eqs. (4.35) and (4.36) are multiplied by $\psi_{B,i}$, with $i = 1,...,N_M$, and integrated over the corresponding areas. After summing both equations,

it is obtained [100]:

$$\sum_{n=1}^{N_A}\left[k_{A,n}\left(A_n^+ - A_n^-\right)\int_{S_A}\psi_{A,n}\left(x,y\right)\psi_{B,i}\left(x,y\right)\,\mathrm{d}S\right] = k_{B,i}\left(B_i^+ e^{-jk_{B,i}(-L_B)} - B_i^- e^{jk_{B,i}(-L_B)}\right)\int_{S_B}\psi_{B,i}^2\left(x,y\right)\,\mathrm{d}S\ , \quad \text{for } i = 1,...,N_M\ . \tag{4.39}$$

Integrals in Eq. (4.39) can be evaluated analytically for simple geometries, e.g., circular or square cross sections. However, the 2D FE formulation is used in case of arbitrary cross sections, hence reducing the computational cost.

4.2.4.2. Transfer matrix of the monolith

1-D propagation is assumed along each capillary of the monolith, and the acoustic pressure and velocity can be related at both sides of it via a transfer matrix **T**:

$$\begin{Bmatrix} P_B(x,y,z'=0) \\ U_B(x,y,z'=0) \end{Bmatrix} = \begin{bmatrix} T_{11}^m & T_{12}^m \\ T_{21}^m & T_{22}^m \end{bmatrix} \begin{Bmatrix} P_D(x,y,z''=0) \\ U_D(x,y,z''=0) \end{Bmatrix} \quad (x,y) \in S_B \equiv S_D\ , \tag{4.40}$$

where the computation of **T** is explained for both catalytic converter and diesel particulate filter in Sections 4.2.1 and 4.2.2, respectively. The same aforementioned approach based on mode matching with weighted integration is applied to the previous System of equations (4.40), multiplying it by the modes $\psi_{B,i} \equiv \psi_{D,i}$, with $i = 1,...,N_M$. Further manipulation of the resulting equations [100] yields:

$$B_i^+ + B_i^- = T_{11}^m\left(D_i^+ + D_i^-\right) + T_{12}^m\frac{k_{D,i}}{\rho_0\omega}\left(D_i^+ + D_i^-\right)\ , \quad \text{for } i = 1,...,N_M\ , \tag{4.41}$$

$$\frac{k_{B,i}}{\rho_0\omega}\left(B_i^+ - B_i^-\right) = T_{21}^m\left(D_i^+ + D_i^-\right) + T_{22}^m\frac{k_{D,i}}{\rho_0\omega}\left(D_i^+ + D_i^-\right)\ , \quad \text{for } i = 1,...,N_M\ . \tag{4.42}$$

The orthogonality of all modes allows the obtaining of a direct relation of modal amplitudes, with no coupling between different-order modes. Additionally, the equation is independent of the cross-sectional geometry.

4.2.4.3. Mode matching at the device contraction

The same process implemented for the geometric expansion can be applied to the contraction involving chamber D and duct E, by considering the compatibility conditions:

$$P_D\left(x,y,z''=L_D\right)=P_E\left(x,y,z'''=0\right)\quad (x,y)\in S_E\ , \tag{4.43}$$

$$U_D\left(x,y,z''=L_D\right)=U_E\left(x,y,z'''=0\right)\quad (x,y)\in S_E\ , \tag{4.44}$$

$$U_D\left(x,y,z''=L_D\right)=0\quad (x,y)\in S_D-S_E\ . \tag{4.45}$$

For the pressure continuity expressed in Eq. (4.43), N_E equations are obtained:

$$\sum_{n=1}^{N_M}\left[\left(D_n^+e^{-jk_{D,i}L_D}+D_n^-e^{jk_{D,i}L_D}\right)\int_{S_E}\psi_{D,n}\left(x,y\right)\psi_{E,i}\left(x,y\right)\ \mathrm{d}S\right]=$$
$$\left(E_i^++E_i^-\right)\int_{S_E}\psi_{E,i}^2\left(x,y\right)\ \mathrm{d}S\ ,\quad \text{for } i=1,...,N_E\ , \tag{4.46}$$

whereas for the acoustic velocity continuity, and the rigid-wall condition, expressed respectively in Eqs. (4.44) and (4.45), N_M equations are obtained:

$$k_{D,i}\left(D_i^+e^{-jk_{D,i}L_D}-D_i^-e^{jk_{D,i}L_D}\right)\int_{S_D}\psi_{D,i}^2\left(x,y\right)\ \mathrm{d}S=$$
$$\sum_{n=1}^{N_E}\left[k_{E,n}\left(E_n^+-E_n^-\right)\int_{S_E}\psi_{E,n}\left(x,y\right)\psi_{D,i}\left(x,y\right)\ \mathrm{d}S\right]\ ,\quad \text{for } i=1,...,N_M\ . \tag{4.47}$$

4.2.4.4. Final system of equations

$N_A+4N_M+N_E$ equations (4.38, 4.39, 4.41, 4.42, 4.46, 4.47) are obtained by using the mode matching method. With a view to solving for the modal amplitudes $\{A_1^\pm,...,A_{N_A}^\pm,\ B_1^\pm,...,B_{N_M}^\pm,\ D_1^\pm,...,D_{N_M}^\pm,\ E_1^\pm,...,E_{N_E}^\pm\}$, additional boundary conditions at the inlet and outlet are needed. An incident plane wave is considered at the inlet, with $A_1^+=1, A_n^+=0$ for $n>1$; whereas the anechoic termination involves no regressive waves at the outlet ($E_n^-=0\ \forall\ n$).

4.3. Objective function: Transmission loss

For the frequency range (up to 3200 Hz) and the dimensions of the outlet duct considered in this Thesis, higher order modes transmitted along the outlet duct E will decay rapidly with distance, hence assuming plane wave propagation at the outlet section. Therefore TL is given by [100]:

$$TL\left(\boldsymbol{\upsilon}\right) = 10\log\left(\frac{\left|P_{in}^{+}\right|^{2} S_{in}}{\left|P_{out}^{+}\right|^{2} S_{out}}\right) = -20\log\left(\frac{r_E}{r_A}\left|E_1^{+}\right|\right) \ , \tag{4.48}$$

where r_A and r_E are the radii of the inlet and outlet ducts, respectively. Contrary to Chapter 3, the objective function $\mathcal{F}_0$ to maximize in Section 4.4 will be defined as the mean TL minus its standard deviation, in order to obtain a more uniform attenuation, while reducing the possible appearance of strong resonant peaks at local frequencies, and also to prove the versatility of the method.

4.4. Optimization problem

The acoustic optimization problem of designing an aftertreatment device targeted to operate in the frequency range $[f_0, f_1]$ can be stated as:

$$\boxed{\begin{array}{c} \max\limits_{\boldsymbol{\upsilon}} \mathcal{F}_0\left(\boldsymbol{\upsilon}\right) = \mu\left(TL(\boldsymbol{\upsilon})\right) - \sigma\left(TL(\boldsymbol{\upsilon})\right) \ , \\ \text{subject to: } \upsilon_j^{min} \leq \upsilon_j \leq \upsilon_j^{max}, \quad \text{for } j = 1, ..., N \ , \end{array}}$$

where μ and σ are the mean and standard deviation of TL within the frequency range, by using a set of samples equally spaced by 10 Hz.

4.5. Results

To obtain the results, the scheme defined in Section 4.2 has been implemented in MATLAB®. The number of modes to evaluate the TL is $N_A =$

$N_E = 10$ at the inlet/outlet ducts and $N_M = 20$ at the chamber. The use of the mode matching technique has been simplified by the use of conforming meshes to evaluate mode cross multiplications relative to the chamber and the inlet/outlet ducts (see Eqs. (4.38, 4.39, 4.46, 4.47)). An additional tool has been implemented in MATLAB®to generate the analyzed geometries (consisting of S_A, $S_B \equiv S_C \equiv S_D$ and S_E, see Figures 4.8 and 4.11) and to mesh them with a maximum element length of 0.005 m.

Finally, a GA has been used to find the global maximum of $\mathcal{F}_0$. For all case studies, an initial population of 50 individuals is chosen, and the maximum number of generations is set to 300.

4.5.1. Design 1. Shape optimization of a catalytic converter

In this example, the acoustic behaviour of a catalytic converter with a circular cross section such as the one shown in Figure 4.6 is to be optimized.

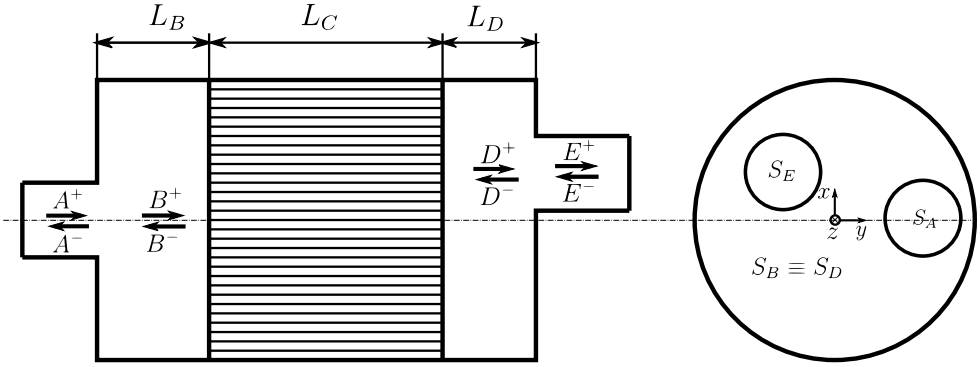

Figure 4.6: Scheme of the optimization.

The radius of the chamber r_C has been fixed to 0.1275 m, as well as the radii of the inlet and outlet ducts $r_A = r_E = 0.0258$ m. Hence, the variables under consideration are: lengths of the chambers L_B and L_D, and the monolith L_C, the porosity σ of the latter, the resistivity of the capillaries R and their shape factor α (1 for circular, 1.07 for square and 1.14 for triangular cross section, see Section 4.2.1). Additionally, the position $\{x, y\}$ of the inlet

and outlet ducts (A and E) is also to be optimized.

Optimization has been carried out at 25 °C and $M_{in} = 0$. Table 4.2 shows the admissible range $\left\{v_j^{min}, v_j^{max}\right\}$ for every design variable, as well as their optimal value for the frequency range $[10, 3200]$ Hz (see Design 1).

v_j	v_j^{min}	v_j^{max}	Design 1	Design 1a	Design 1b
L_B (m)	0.05	0.15	0.0535	0.0535	0.0535
L_C (m)	0.1	0.3	0.3	0.3	0.3
L_D (m)	0.05	0.15	0.0674	0.0674	0.0674
R (Pa·s/m^2)	500	1000	1000	1000	1000
σ	0.7	0.9	0.9	0.9	0.9
α	$\{1, 1.07, 1.14\}$		1.14	1.14	1.14
x_A (m)	-0.1	0.1	-0.0778	0	0
y_A (m)	-0.1	0.1	0.0111	0	0
x_E (m)	-0.1	0.1	0.0026	-0.0778	0
y_E (m)	-0.1	0.1	-0.008	0.0111	0

Table 4.2: *Optimization summary. Range for each variable v_i. Optimal values for Designs 1 (offset inlet, nearly centered outlet), 1a (centered inlet, offset outlet) and 1b (centered inlet and outlet).*

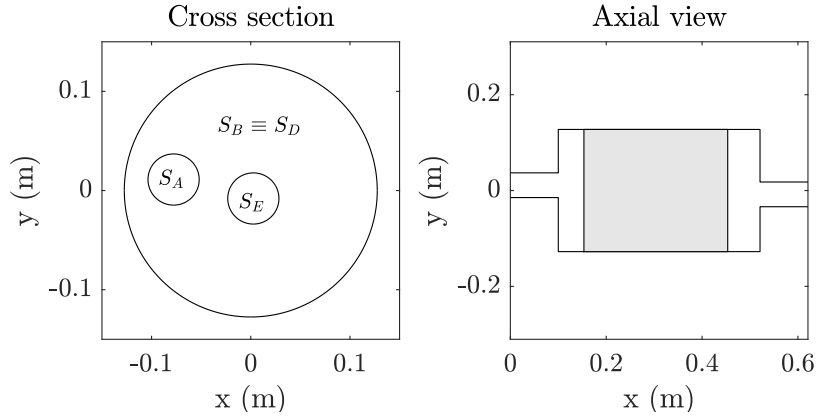

Figure 4.7: Optimized catalytic converter. Design 1.

As expected, optimization maximized L_C and R [99] (see Design 1). Triangular capillaries also increased attenuation, in line with [99]. Additionally, it

can be seen that a set-up with a nearly centered outlet (duct E) and an offset inlet (duct A) contributes beneficially to attenuation. Concretely, an offset of 0.0778 m (or equivalently 0.616 r_C) has been obtained, as depicted in Figure 4.7. This phenomenon has been explained in Section 4.5.1.1, and to this aim two additional designs have been analysed: Design 1a (with a centered inlet and offset outlet), and Design 1b (with centered inlet and outlet).

Finally, the FE mesh used for the optimal S_A, $S_B \equiv S_C \equiv S_D$ and S_E are shown below. Note that they are conforming at S_A and S_E.

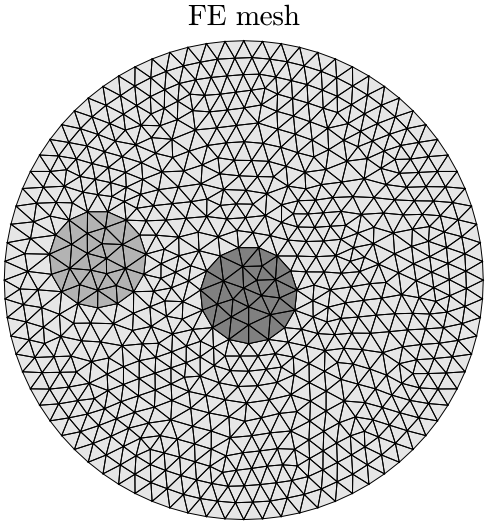

Figure 4.8: S_A, $S_B \equiv S_C \equiv S_D$ and S_E FE meshes. Design 1.

4.5.1.1. Influence of duct offsets

Figure 4.9 shows the first 20 transversal pressure modes considered for the acoustic propagation within the central chamber.

As suggested in [99, 104, 105], the inlet and outlet ducts should be positioned in such a way that the modes most excited by the inlet do not propagate their acoustic energy to the outlet duct. As it has been found by GA, an offset inlet duct by 0.616 r_C can effectively improve attenuation within the studied frequency range since it matches the nodal line of Mode 6 (at 1626.5 Hz, see Figure 4.9). Additionally, the centered outlet matches the nodal line of the other non-constant pressure Modes 2, 3, 4 and 5 which, although they are

indeed excited by the inlet, do not propagate acoustic energy to the outlet duct.

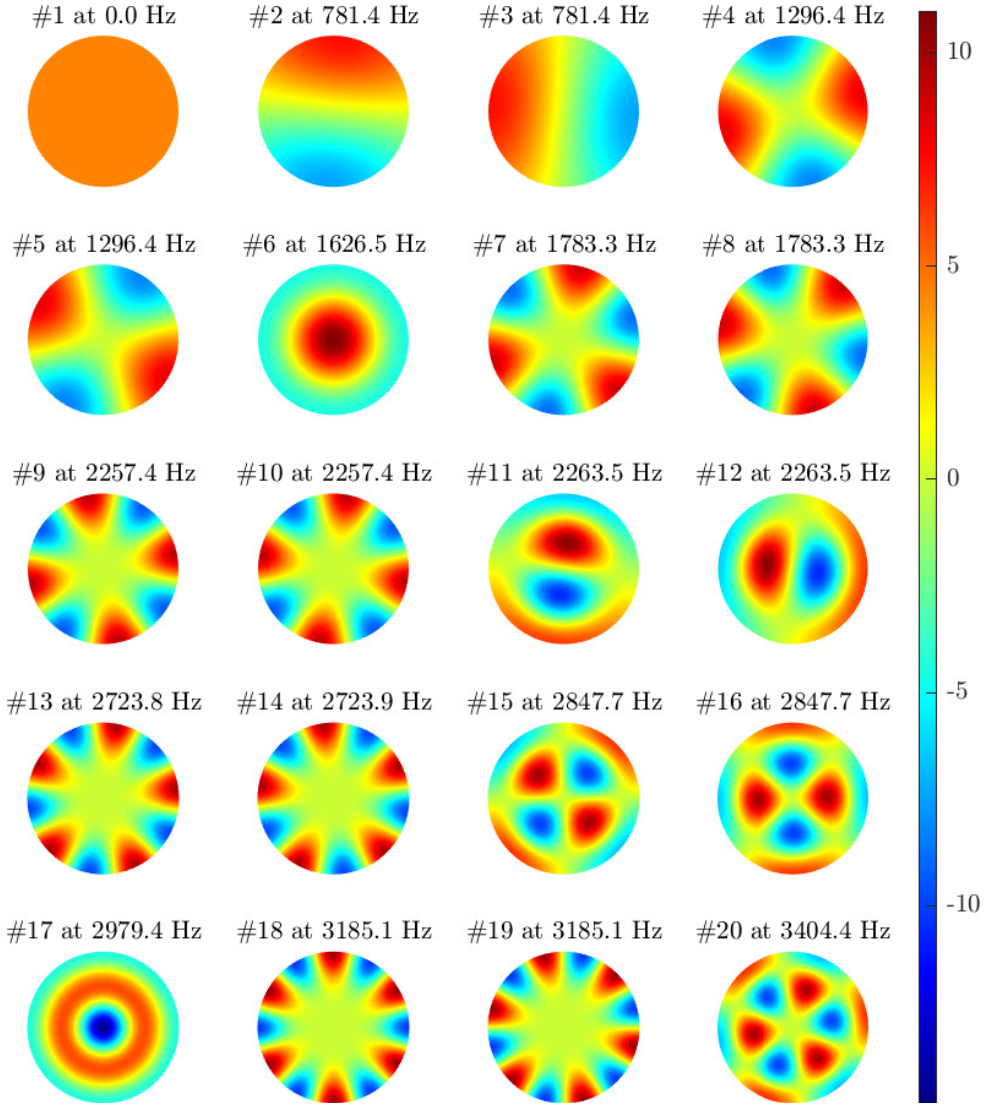

Figure 4.9: Pressure modes of circular section $S_B \equiv S_D$, here sorted by increasing natural frequency (they can also be classified into radial and circumferential modes, or a combination of both).

Similarly, due to reciprocity, the same effect can be obtained by offsetting the outlet by the same distance (and centering the inlet). This design will be hereinafter referred to as Design 1a. An additional configuration with both ducts centered has also been studied and will be referred to as Design 1b (see Table 4.2).

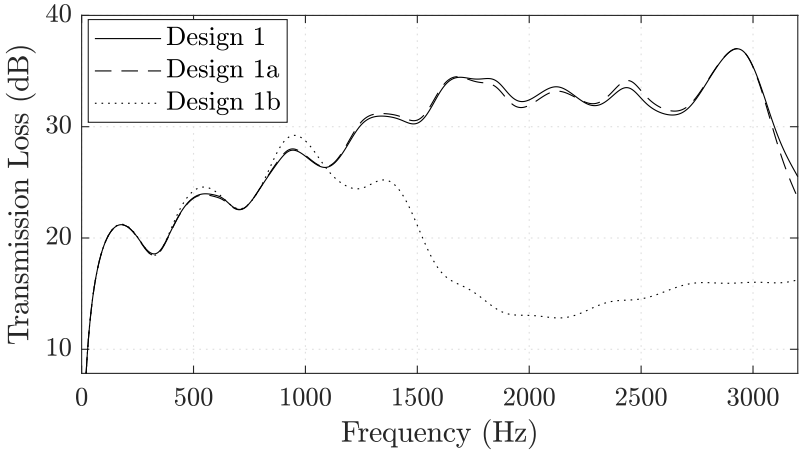

Figure 4.10: TL for Designs $\boldsymbol{v}^{opt}$, $\boldsymbol{v}^1$ and $\boldsymbol{v}^2$.

TL has been evaluated for Designs 1, 1a and 1b; and results are shown in Figure 4.10. It has been obtained that the performance of Design 1b (with centered inlet and outlet ducts) degrades with respect to Designs 1 (with offset inlet) and 1a (with offset outlet) for frequencies from 1100 Hz up, due to the propagation of axisymmetric Mode 6. However, for Designs 1 and 1a with one offset duct, TL exhibits a regular behaviour until higher-order modes play a role in acoustic propagation.

4.5.2. Design 2. Shape optimization of a diesel particulate filter

Next, a DPF with triangular cross section has been optimized. The equilateral triangle's sides measure 0.35 m, and its height is hence $h = 0.3031$ m. Additionally, it is chamfered with a chamfer's radius of 0.0310 m. For the sake of computational speed, the inlet and outlet ducts have a fixed position, allowing the use of the same FE mesh along all iterations (see Figure 4.11).

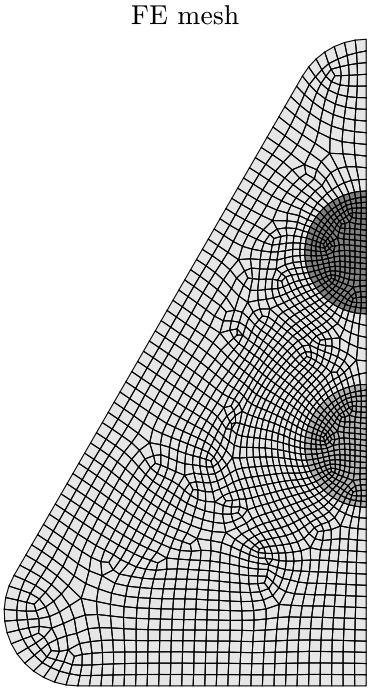

Figure 4.11: S_A, $S_B \equiv S_D$ and S_E FE meshes. Design 2.

The inlet duct is positioned at the center of the equilateral triangle, whereas the outlet duct is placed 0.1824 m above the triangle's base, i.e., $0.602h$, in order to match the nodal line of the higher order mode at 1228 Hz (see Figure 4.12) [99]. The radius of the inlet and outlet ducts is $r_A = r_E = 0.0258$ m. Finally, optimization has been carried out for TL at a supposed working temperature of 501.85 °C [99] and $M_{in} = 0.02$.

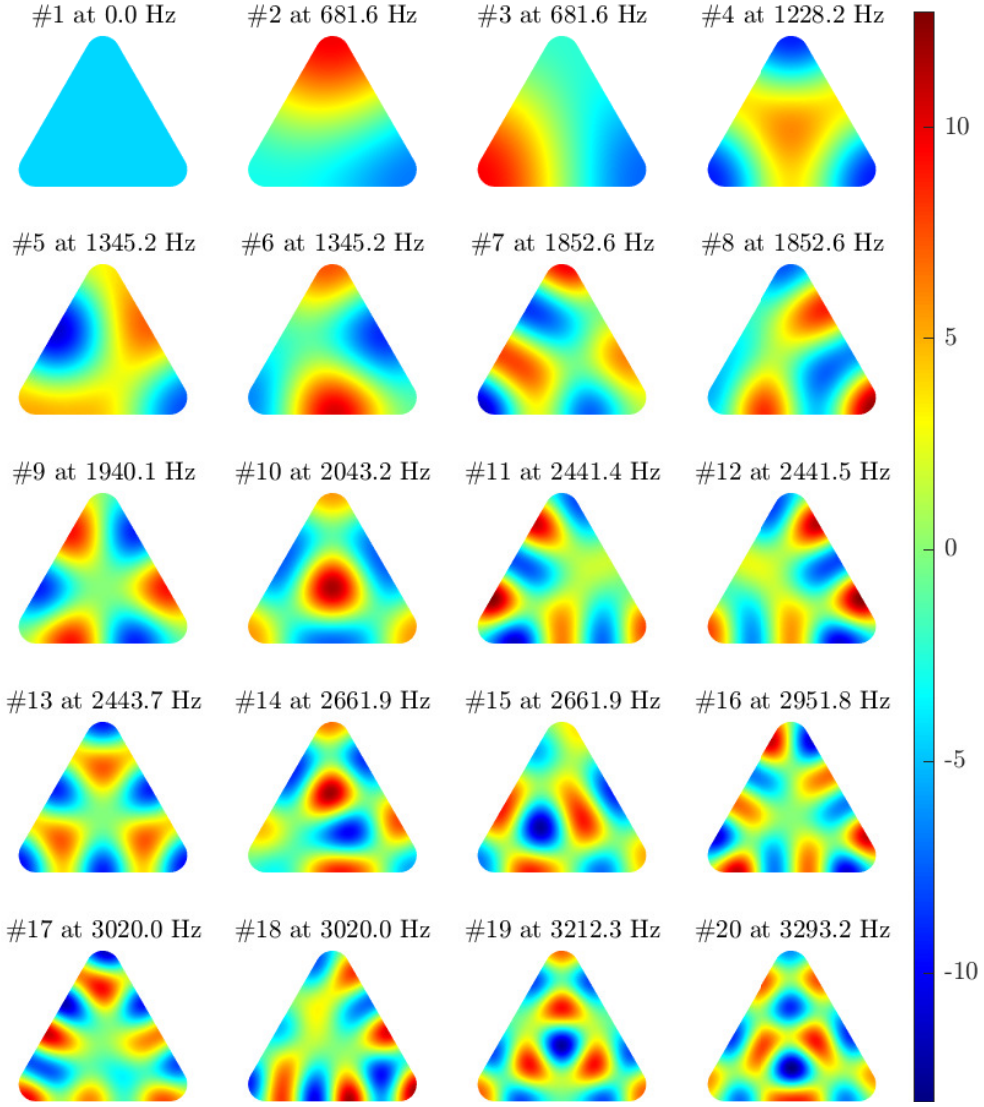

Figure 4.12: Pressure modes of triangular section $S_B \equiv S_D$.

On the other hand, four DPF cell types have been found in the literature [97]. Data for their characterization is shown below in Table 4.3. Additionally, the length of the channel plug has been supposed to be $l_I = l_{III} = 0.005$ m for both the inlet and outlet of the capillary ducts.

	Filter name	d_h [m]	h_t [m]	σ_w [m^2]	channels ($2N$) [1/m^2]
1	EX 200/14	1.44×10^{-3}	3.55×10^{-4}	2.5×10^{-13}	3.10×10^5
2	EX 100/17	2.11×10^{-3}	4.30×10^{-4}	2.5×10^{-13}	1.55×10^5
3	RC 200/12	1.50×10^{-3}	3.04×10^{-4}	25×10^{-13}	3.87×10^5
4	RC 200/20	1.30×10^{-3}	5.08×10^{-4}	25×10^{-13}	2.48×10^5

Table 4.3: *Data for the DPF units under study.*

GA have been applied to the DPF design problem, optimizing the lengths of the chambers and monolith, as well as the type of DPF unit employed. The optimal designs for two target frequency ranges $[20 - 3200]$ Hz and $[20 - 1000]$ Hz are shown in Table 4.4, named Designs 2 and 2a respectively.

υ_j	υ_j^{min}	υ_j^{max}	Design 2	Design 2a
L_B (m)	0.05	0.15	0.15	0.15
L_C (m)	0.1	0.3	0.3	0.1
L_D (m)	0.05	0.15	0.0926	0.15
DPF type	{EX 200/14, EX 100/17, RC 200/12, RC 200/20}		EX 200/14	EX 100/17

Table 4.4: *Optimization summary. The range for each variable υ_j. Optimal values for Designs 2 (optimized at $[20 - 3200]$ Hz), and 2a (optimized at $[20 - 1000]$ Hz).*

Table 4.4 shows that lengths L_B and L_D of the chambers tend to their maximum bound for the low-frequency range as expected (Design 2a). However, it has been found by the GA optimization that the shortest possible DPF monolith increases attenuation in this case.

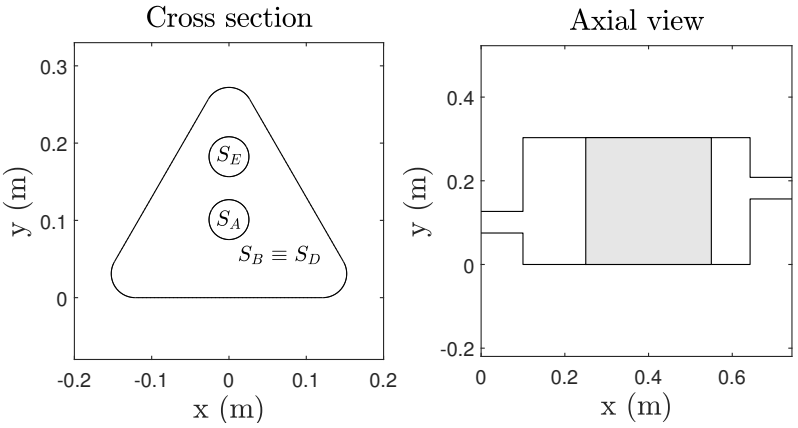

Figure 4.13: Optimized diesel particulate filter. Design 2.

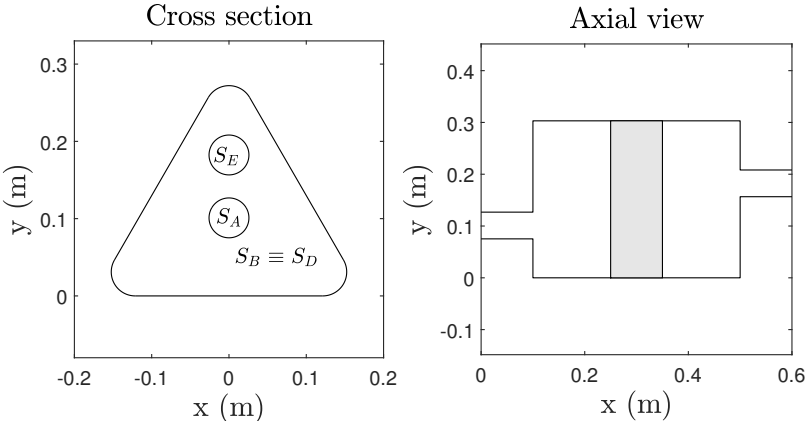

Figure 4.14: Optimized diesel particulate filter. Design 2a.

On the contrary, for the full frequency range, i.e., $[20 - 3200]$ Hz, the length of the monolith increases to the maximum value, and the downstream chamber length L_D decreases (see Design 2 in Table 4.4).

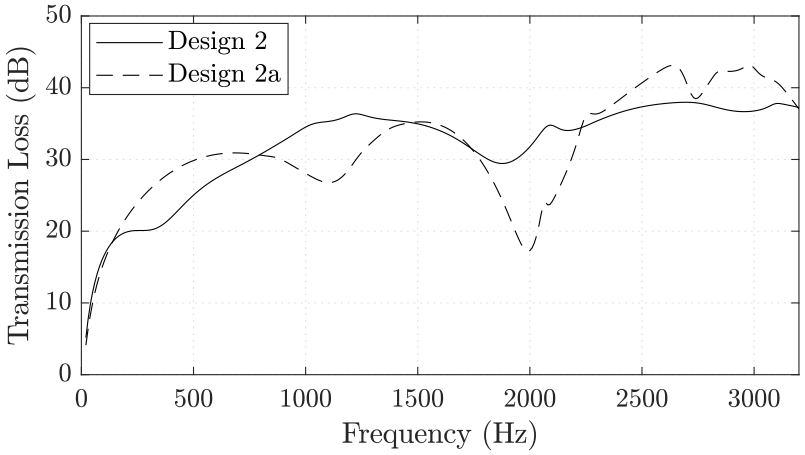

Figure 4.15: TL for Designs 2 and 2a.

Table 4.5 shows the results of the TL evaluation for both Designs 2 and 2a. In line with Chapter 3, results show the importance of considering the right target (working) frequencies during the optimization process, since the optimization of TL within a narrow frequency range can result in a worse performance at frequencies outside it. For example, Design 2a improves $\mathcal{F}_0$ in the low-frequency range only by 2 dB with respect to Design 2 (see Table 4.5), whereas it delivers a TL around 15 dB lower at 2000 Hz (see Figure 4.15).

$\boldsymbol{v}$	$\mathcal{F}_0$ (dB) at [20,3200] Hz	$\mathcal{F}_0$ (dB) at [20,1000] Hz
Design 2	25.59	18.26
Design 2a	24.09	20.13

Table 4.5: *Optimization summary. Objective function $\mathcal{F}_0$ for Designs $\boldsymbol{v}^{opt,1}$ and $\boldsymbol{v}^{opt,2}$, evaluated at both the whole and low frequency ranges.*

4.6. Conclusions

This Chapter presents a shape optimization methodology to effectively increase the attenuation of aftertreatment devices including a monolith (such as catalytic converters and diesel particulate filters). The evaluation of the TL has been performed via a hybrid analytical-numerical model which allows the

consideration of arbitrary (axially uniform) cross sections for the chamber, as well as offset inlet/outlet ducts.

The combination of modal expansion and mode matching methodologies allows the efficient calculation of the TL for a wide set of frequencies, once the chamber's transversal pressure modes are obtained.

Due to the low number of design variables, the optimization problem has been solved by the use of genetic algorithms, which also permit applying lateral constraints, while performing a more global search in comparison with gradient-based algorithms.

Results showed that for a given cross section, the influence of the position of the inlet/outlet ducts, as well as the length of the monolith, is crucial, and important increases in TL can be accomplished by strategically placing both ducts in different positions so that the acoustic energy associated with the incident modes is not transmitted to the outlet.

Chapter 5

Topology optimization of fluid-structure problems

Transport-related noise is one of today's main sources of acoustic pollution. In this context, the obtaining of optimized lightweight structures with low acoustic emission is of great importance. Thus, one way to perform this would be to extend the application of the aforementioned algorithms to the vibroacoustic problem. Topology optimization has been successfully applied to both elasticity and acoustic problems in order to obtain non-intuitive air-material designs that minimize an objective function. As we know, the concept of shape is disregarded in this method, and the equation to solve is the same within the whole design domain of the proposed problem, whether (i) the linear elasticity equation, or (ii) the linear sound wave (Helmholtz) equation; with different properties being assigned to each element, depending on their respective state value, which continuously ranges from 0 (air) to 1 (material).

However, for vibroacoustic problems where the equation to solve is different for both the fluid and structural domains, topology optimization algorithms do not seem appropriate due to the nature of the mentioned method. In this Chapter, the mixed displacement/pressure formulation [33] is recalled. This approach allows the modelling of both the fluid and solid phases by means of a single equation. However, the use of this costly formulation is limited here to a small area of the problem's domain. Finally, a three-material interpolating scheme is set up in order to obtain designs consisting of solid and porous parts.

5.1. Introduction

The obtaining of algorithms that allow the design of resistant lightweight structural parts with high acoustic isolation performance is of great importance in today's transport. For example, railway rolling noise can be reduced by the use of wheel perforations [4], the modification of the wheel's web geometry [5], or the use of lower train fairings.

Previous literature provides several ways for solving the vibroacoustic TO problem: some studies disregard the elasticity of the structure, i.e., only the wave equation is solved in the whole domain. Hence, the acoustic impedance Z of each element is interpolated as a function of density υ_j, ranging from the characteristic impedance of the air Z_0 to a very large value $Z_s >> Z_0$ which imitates the behaviour of rigid walls. Thus, solid partitions can be introduced via the standard iterative process by evaluating the sensibilities of $\mathcal{F}_0$ (often defined as the acoustic pressure's amplitude at a chosen location). In [106], an optimized horn was obtained with a view to minimizing the amplitude of the reflected wave going back into the waveguide. In [42], the shape of a room ceiling was optimized by TO to reduce the noise at a target location. In [43], a dissipative highway noise barrier was obtained by adopting a three-material interpolating scheme, with air, solid, and porous material. In this Chapter, the use of three-material schemes, which require defining a pair of design variables per element, has been studied.

Another way to proceed is to account for the elasticity of the structural part, without modifying the fluid-structure boundary: only inner components are designed by TO. In [107], an enclosure was stiffened by applying TO to reduce the interior low-frequency noise. In [108], a bi-material surface was optimized with the aim of reducing sound emission under a harmonic load. The shell of a hearing instrument was stiffened by TO methods in reference [109], minimizing the sound pressure at certain microphone locations.

The coupling boundary can be modified by using an alternative algorithm to the conventional density-based TO method. The level-set method [110] and the bi-directional evolutionary structural optimization (BESO) [111] have effectively been used along with a two-phase scheme in order to optimize noise barriers while solving the sound propagation and linear elasticity equations

within the acoustic and solid subdomains Ω_a and Ω_s, respectively. However, the final shape depends on the initial guess, e.g. number of initial holes, which is not always easily obtainable in an intuitive way for complex problems such as the acoustic topology optimization (ATO).

With the aim of considering both the elastic and acoustic parts, and not having to define the coupling boundary at every iteration, the displacement/pressure ($\mathbf{u}/p$) mixed formulation has been proposed. In [33], the $\mathbf{u}/p$ formulation [34, 41] was employed to design a noise barrier within a duct by means of TO algorithms.

In the present study, the three-material scheme (air, solid and porous material) [43] has been considered by introducing a pair of variables per element: $\{\upsilon_{j,1}, \upsilon_{j,2}\}$. The porous medium is modelled as an equivalent fluid, which does not provide structural stiffness [112], and therefore the wave equation has been solved within it [45]. In addition, this work proposes to limit the use of the costly $\mathbf{u}/p$ formulation to only Ω_d, which usually comprises a small portion of the problem's total domain; whereas the wave propagation equation in terms of p is solved in the remaining acoustic domain.

5.2. Vibroacoustic modelling of a fluid-structure interaction problem

The scheme of the standard vibroacoustic domain has been introduced in Figure 2.4, where the problem domain has been split into structural (solid elastic) Ω_s and acoustic (air) Ω_a subdomains. Figure 5.1 shows a modified definition of the vibroacoustic problem where the design subdomain Ω_d can contain solid, porous and air elements, since the mixed $\mathbf{u}$/p formulation is employed here; whereas the acoustic subdomain Ω_a is meshed with standard pressure elements:

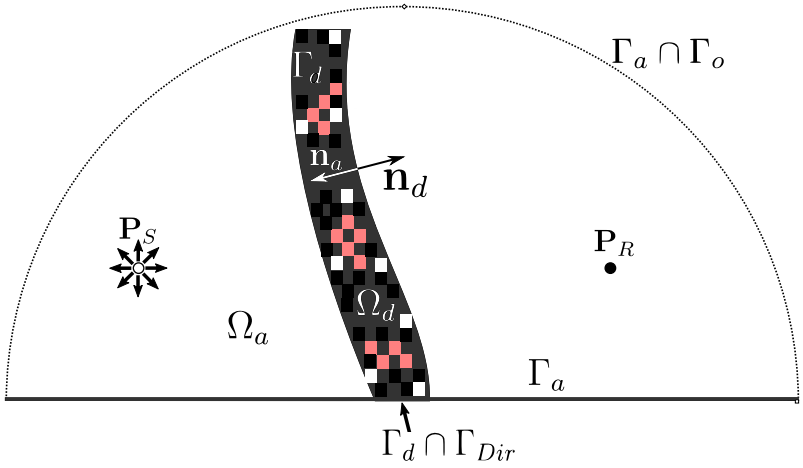

Figure 5.1: Modified fluid-structure interaction problem scheme.

where P_S and P_R denote the position of the noise source (emitter) and receiver (at which the noise level is to be reduced), Γ_a and Γ_d refer to the respective boundaries of Ω_a and Ω_d, $\mathbf{n}_a$ and $\mathbf{n}_d$ are their corresponding outward unit vectors, and Γ_o and Γ_{Dir} denote the absorbing boundary and the boundary where Dirichlet conditions are applied.

5.2.1. Mixed finite element method in Ω_d

The FE discretization [33] is applied to the two-dimensional weak form of the mixed $\mathbf{u}$/p formulation Eqs. (2.85) and (2.86), recalled in Section 2.2. In order to fulfill the Inf-Sup condition [34], first and second-order shape functions are used for pressure and displacement degrees of freedom, respectively. This leads to the following system of equations [33, 34, 56]:

$$\begin{bmatrix} \mathbf{K}_d^{uu} - \omega^2 \mathbf{M}_d^{uu} & \mathbf{C}_d^{up} \\ (\mathbf{C}_d^{up})^T & \mathbf{D}_d^{pp} \end{bmatrix} \begin{bmatrix} \tilde{\mathbf{U}}_d \\ \tilde{\mathbf{P}}_d \end{bmatrix} = \begin{bmatrix} \mathbf{F}_u \\ 0 \end{bmatrix} , \tag{5.1}$$

where vectors $\tilde{\mathbf{U}}_d$ and $\tilde{\mathbf{P}}_d$ contain the unknown nodal values of displacements and pressure, and subscript d refers to the design subdomain Ω_d, where a set of solid, air and porous elements is expected. Matrices present in Eq. (5.1)

are assembled as:

$$\mathbf{K}_d^{uu} = \sum_{e=1}^{N_d} \int_{\Omega_e} 2G\mathbf{B}_u^T\mathbf{D}_d\mathbf{B}_u \, \mathrm{d}\Omega \, , \tag{5.2}$$

$$\mathbf{M}_d^{uu} = \sum_{e=1}^{N_d} \int_{\Omega_e} \rho\mathbf{N}_u^T\mathbf{N}_u \, \mathrm{d}\Omega \, , \tag{5.3}$$

$$\mathbf{C}_d^{up} = \sum_{e=1}^{N_d} - \int_{\Omega_e} \mathbf{B}_u^T\mathbf{m}\mathbf{N}_p \, \mathrm{d}\Omega \, , \tag{5.4}$$

$$\mathbf{D}_d^{pp} = \sum_{e=1}^{N_d} - \int_{\Omega_e} \frac{1}{K}\mathbf{N}_p^T\mathbf{N}_p \, \mathrm{d}\Omega \, , \tag{5.5}$$

$$\mathbf{F}_u = \sum_{e=1}^{N_d} \int_{\Gamma_e \cap \Gamma_d} \mathbf{N}_u^T \left(\boldsymbol{\sigma}\mathbf{n}_d\right) \, \mathrm{d}\Gamma \, , \tag{5.6}$$

where N_d is the number of elements within Ω_d; $\mathbf{N_p}$ and $\mathbf{N_u}$ denote the matrices containing the nodal values of the corresponding shape functions; $\mathbf{B}_u$ refers to the strain-displacement relation; and $\sum$ represents the usual FE matrix assembly operator.

5.2.2. Helmholtz equation in Ω_a

The acoustic field within Ω_a (see Figure 2.4) can be easily obtained by extending the mixed formulation described in Section 5.2.1. However, the computational cost can be sensibly reduced by adopting here the standard pressure formulation. In order to illustrate this, Problem 1 (see Section 5.6.2) will be adopted here as an example. Figure 5.2 shows both approaches in order to mesh the problem, by using square elements in all domains (0.01 m x 0.01 m here for simplicity). Figure 5.2a shows the resulting nodes by extending the mixed $\mathbf{u}/p$ formulation to both Ω_d and Ω_a [33, 41]. In contrast, the approach proposed in this study is shown in Figure 5.2b: Helmholtz equation is solved within Ω_a by means of the standard p formulation in order to reduce the number of total degrees of freedom (d.o.f.).

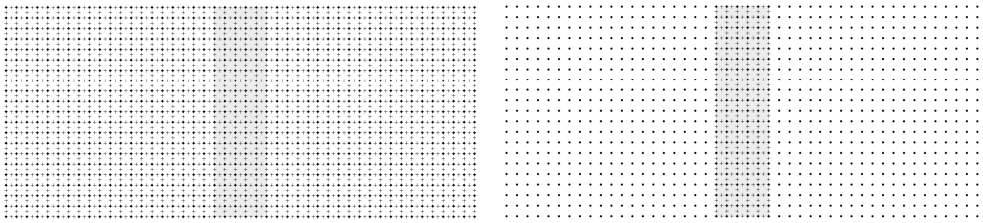

(a) Mixed formulation extended to both Ω_a and Ω_d.

(b) Mixed formulation limited to Ω_d.

Figure 5.2: Position of p (•) and $\mathbf{u}$ (+) nodes. Case study 1.

The proposed methodology allows to speed up the computation of the problem. This advantage becomes of special importance in case that Ω_d represents a small extension of the whole domain, such as in the ATO problem. Table 5.1 shows the size of the resulting FE mesh, and the computation time for the aforementioned case study, by using 0.001 x 0.001 m square elements in Problem 1 (see Section 5.6.2):

	Extended $\mathbf{u}$/p formulation	$\mathbf{u}$/p in Ω_d p in Ω_a
No. of p nodes	90651	90651
No. of $\mathbf{u}$ nodes	271301	30501
No. of d.o.f.	633253	151653
Computation time (s)	158.28	15.27

Table 5.1: *Formulation comparison for Problem 1 of Section 5.6.2. An Intel® Xeon® CPU with a 16 GB memory was used to perform the calculations.*

The standard FE method for the acoustic problem will be hence briefly recalled next for the sake of completeness. In the homogeneous non-moving medium corresponding to Ω_a, sound propagation can be described by Eq. (2.30). By applying the FE discretization [35], it yields the following system of equations [113]:

$$\left(\mathbf{K}_a - \omega^2 \mathbf{M}_a\right) \tilde{\mathbf{P}}_a = \mathbf{F}_a \ , \tag{5.7}$$

$\tilde{\mathbf{P}}_a$ being the pressure value at the nodes of Ω_a. The stiffness, mass and force terms are given by:

$$\mathbf{K}_a = \sum_{e=1}^{N_a} \int_{\Omega_e} \mathbf{B}_p^T \mathbf{B}_p \, \mathrm{d}\Omega \ , \tag{5.8}$$

$$\mathbf{M}_a = \frac{1}{c_0^2} \sum_{e=1}^{N_a} \int_{\Omega_e} \mathbf{N}_p^T \mathbf{N}_p \, \mathrm{d}\Omega \ , \tag{5.9}$$

$$\mathbf{F}_a = \sum_{e=1}^{N_a} \int_{\Gamma_e \cap \Gamma_a} \mathbf{N}_p^T \frac{\partial P}{\partial n_a} \, \mathrm{d}\Gamma \ , \tag{5.10}$$

where N_a is the number of elements within Ω_a, and $\mathbf{B}_p = \nabla \mathbf{N}_p$.

5.2.3. Subdomain coupling

In order to couple subdomains Ω_d and Ω_a, Eqs. (2.77) and (2.78) are considered. The pressure gradient normal to the boundary $\Gamma_{coup} = \Gamma_d \cap \Gamma_a$ induced by the vibration of the structure can be expressed as:

$$\frac{\partial P}{\partial n_a} = {\mathbf{n}_a}^T \nabla P = \mathbf{n}_a^T \omega^2 \rho_0 \mathbf{U} \ , \tag{5.11}$$

and by evaluating this in Eq. (5.10), the effect of the structure on the surrounding air is obtained:

$$\mathbf{F}_a^{coup,1} = \sum_{e=1}^{N_a} \int_{\Gamma_e \cap \Gamma_{coup}} \mathbf{N}_p^T \mathbf{n}_a^T \omega^2 \rho_0 \mathbf{U} \, \mathrm{d}\Gamma = \omega^2 \rho_0 \sum_{e=1}^{N_a} \int_{\Gamma_e \cap \Gamma_{coup}} \mathbf{N}_p^T \mathbf{n}_a^T \mathbf{N}_u \, \mathrm{d}\Gamma \, \tilde{\mathbf{U}}_d \ . \tag{5.12}$$

This term is then moved to the left-hand side of Eq. (5.7) by means of an additional mass term following the relation $\omega^2 \mathbf{M}_a^{coup} \tilde{\mathbf{U}}_d = \mathbf{F}_a^{coup,1}$, yielding:

$$\mathbf{M}_a^{coup} = \rho_0 \sum_{e=1}^{N_a} \int_{\Gamma_e \cap \Gamma_{coup}} \mathbf{N}_p^T \mathbf{n}_a^T \mathbf{N}_u \, \mathrm{d}\Gamma \ . \tag{5.13}$$

On the other hand, the acoustic pressure over the surface Γ_{coup} is introduced into Eq. (5.6) to obtain:

$$\mathbf{F}_a^{coup,2} = \sum_{e=1}^{N_d} \int_{\Gamma_e \cap \Gamma_{coup}} \mathbf{N}_u^T \left(-P \mathbf{n}_d\right) \, \mathrm{d}\Gamma = -\sum_{e=1}^{N_d} \int_{\Gamma_e \cap \Gamma_{coup}} \mathbf{N}_u^T \mathbf{n}_d \mathbf{N}_p \, \mathrm{d}\Gamma \, \tilde{\mathbf{P}}_a \ . \tag{5.14}$$

Further manipulation leads to a new term in Eq. (5.1):

$$\mathbf{K}_d^{coup} = \sum_{e=1}^{N_d} \int_{\Gamma_e \cap \Gamma_{coup}} \mathbf{N}_u^T \mathbf{n}_d \mathbf{N}_p \, \mathrm{d}\Gamma \ . \tag{5.15}$$

Finally the global system of equations can be written as:

$$\begin{bmatrix} \mathbf{K}_d^{uu} - \omega^2 \mathbf{M}_d^{uu} & \mathbf{C}_d^{up} & \mathbf{K}_d^{coup} \\ (\mathbf{C}_d^{up})^T & \mathbf{D}_d^{pp} & 0 \\ -\omega^2 \mathbf{M}_a^{coup} & 0 & \mathbf{K}_a - \omega^2 \mathbf{M}_a \end{bmatrix} \begin{bmatrix} \tilde{\mathbf{U}}_d \\ \tilde{\mathbf{P}}_d \\ \tilde{\mathbf{P}}_a \end{bmatrix} = \begin{bmatrix} \mathbf{F}_u \\ 0 \\ \mathbf{F}_a \end{bmatrix} \ . \tag{5.16}$$

5.2.4. Absorbing boundary Γ_o

Absorbing boundaries Γ_o will be modelled in Sections 5.6.2–5.6.4. Note that they should be placed at a minimum distance of 2 wavelengths of any geometric singularity in order to ensure that the wave front of the wave incoming is parallel to them. This boundary condition can be expressed by:

$$\mathbf{n}_a \cdot \nabla P + jk_a p = 2jk_a P_e \ , \tag{5.17}$$

where the excitation's amplitude P_e is zero for the anechoic outlet [33, 87].

5.3. Two-material interpolation schemes of vibroacoustic properties

According to the **u**/p formulation explained in Section 2.2.1, the vibroacoustic behaviour within the air, solid and porous elements of Ω_d can be characterized by their bulk and shear moduli, denoted by K and G respectively, and density ρ. For the structural material, K_s and G_s are related to Young's modulus E and Poisson's ratio ν. In the case of two-dimensional plane strain [33]:

$$K_s = \frac{E}{2(1+\nu)(1-2\nu)} \ , \tag{5.18}$$

$$G_s = \frac{E}{2(1+\nu)} \ , \tag{5.19}$$

whereas for the non-structural/acoustic media, K is related to ρ and c, and $G = 0$ [33]:

$$K_0 = \rho_0 c_0^2 \ , \quad K_p = \rho_p c_p^2 \ , \tag{5.20}$$

$$G_0 = 0 \ , \qquad G_p = 0 \ , \tag{5.21}$$

where subscripts $(\cdot)_0$ and $(\cdot)_p$ refer to the air and porous medium, respectively. $G = 0$ implies that System (5.1) turns into the Helmholtz sound wave propagation equation [33,112]. Note that c_p and ρ_p are complex and frequency-dependent properties in order to account for the acoustic energy dissipation within the sound-absorbing porous material.

The use of gradient-based algorithms requires continuous models for any material property ϱ, which in this three-material study should be evaluated as a function of the element's variable pair $\{\upsilon_{1,j},\ \upsilon_{2,j}\}$. Following the standard RAMP method [33, 108] described in Section 2.3.3.1, it is obtained:

$$\varrho(\upsilon_{1,j}, \upsilon_{2,j}) = \varrho_0 + (\varrho_s - \varrho_0)\phi\left(\upsilon_{1,j}\right) + (\varrho_p - \varrho_0)\phi\left(\upsilon_{2,j}\right) \ , \tag{5.22}$$

where ϱ_0, ϱ_s and ϱ_p denote any vibroacoustic property (K, G) for the selected air, solid and porous materials. Expression (5.22) implies that $\{\upsilon_{1,j}, \upsilon_{2,j}\}$ equals $\{0, 0\}$ for air elements, $\{1, 0\}$ for the structure and $\{0, 1\}$ for the porous medium. However, a correction is needed so that solid and absorbent materials do not appear at once for the pair $\{1, 1\}$. A new pair of design variables $\{\psi_{1,j}, \psi_{2,j}\}$ is then considered [108] for the RAMP approach:

$$\psi_{1,j} = \upsilon_{1,j} \ , \tag{5.23}$$

$$\psi_{2,j} = \upsilon_{2,j}(1 - \upsilon_{1,j}) \ . \tag{5.24}$$

The interpolation scheme of vibroacoustic properties is therefore:

$$K(\psi_{1,j}, \psi_{2,j}) = K_0 + (K_s - K_0)\,\phi(\psi_{1,j}) + (K_p - K_0)\,\phi(\psi_{1,j}, \psi_{2,j}) \ , \tag{5.25}$$

$$G(\psi_{1,j}) = G_s \phi_1(\psi_{1,j}) \ , \tag{5.26}$$

ϕ being the RAMP penalty function [33, 108], as explained in Section 2.3.3.1:

$$\phi(\psi_{i,j}) = \frac{\psi_{i,j}}{1 + (1 - \psi_{i,j})q} \quad \text{for } i = \{1, 2\} \ , \tag{5.27}$$

where a penalty factor q of value 3 [33, 108] has been used throughout this Chapter to penalize intermediate values of $\{\upsilon_1, \upsilon_2\}$. On the other side, however, density is interpolated linearly without penalizing intermediate values [33], following:

$$\rho(\psi_{1,j}, \psi_{2,j}) = \rho_0 + (\rho_s - \rho_0)\psi_{1,j} + (\rho_p - \rho_0)\psi_{2,j} \ . \tag{5.28}$$

5.4. Objective function

As observed in [33], the process of acoustically optimizing a structure at a certain frequency f is equivalent to modifying its design so that its natural frequencies lay further from f (so the response of the structure is low at this frequency). Thus, the consideration of high frequencies can result in optimized structures consisting of a very high mass suspended by thin walls (the lower natural frequencies will be shifted to the left, i.e., will become lower), which are not feasible from the structural point of view. In [33], this problem is circumvented by including sensitivities obtained for a lower excitation frequency of $f/3$. In this Chapter, the aforementioned problem has been solved by considering a standard linear-elasticity TO problem, where a realistic load case has been regarded in each case. Then, the objective function has been built by weighing both contributions with corresponding weights w_1 and w_2, respectively:

$$\mathcal{F}_0\left(\boldsymbol{\upsilon}\right) = w_1 \frac{\mathcal{F}_0^{(1)}\left(\boldsymbol{\upsilon}\right)}{\mathcal{F}_0^{(1)}\left(\boldsymbol{\upsilon}_0\right)} + w_2 \frac{\mathcal{F}_0^{(2)}\left(\boldsymbol{\upsilon}\right)}{\mathcal{F}_0^{(2)}\left(\boldsymbol{\upsilon}_0\right)} \ , \tag{5.29}$$

where $\mathcal{F}_0^{(1)}$ and $\mathcal{F}_0^{(2)}$ refer to the objective functions corresponding to the aforementioned acoustic and elastic problems (defined in Sections 5.4.1 and 5.4.2, respectively), and $\boldsymbol{\upsilon}_0$ refers to the initial design.

5.4.1. Acoustic contribution

As stated in Section 5.2.4, the acoustic domain is extended in every problem by means of a distant absorbing boundary Γ_o so that no wave reflections

take place. Hence, the integral of the acoustic amplitude along Γ_o can give a hint of the total noise radiation to the surroundings. For the frequency range of interest $[f_0, f_1]$, this yields:

$$\mathcal{F}_0^{(1)}(\boldsymbol{v}) = \frac{1}{f_1 - f_0} \int_{f_0}^{f_1} \int_{\Gamma_o} |P(\boldsymbol{v})| \, \mathrm{d}\Omega \, \mathrm{d}f \, . \tag{5.30}$$

5.4.2. Static load case

As aforementioned, a standard static structural TO problem [56] is considered with a view to avoiding unrealistic designs , and by considering only Ω_d (the stiffness of the air elements is negligible), the compliance c is defined as:

$$\mathcal{F}_0^{(2)}(\boldsymbol{v}) = c(\boldsymbol{v}) = \int_{\Omega_d} \mathbf{U}^T \mathbf{K} \mathbf{U} \, \mathrm{d}\omega \, , \tag{5.31}$$

after solving $\mathbf{KU} = \mathbf{F}$ where $\mathbf{K}$ is the stiffness matrix, and $\mathbf{U}$ and $\mathbf{F}$ are the nodal displacement and force vectors, which contain prescribed entries.

5.5. Optimization problem

The multi-objective optimization problem stated in Section 5.4 is formally expressed below:

$$\boxed{\begin{aligned} &\min_{\boldsymbol{v}} \mathcal{F}_0(\boldsymbol{v}) \, , \\ &\text{subject to: } \mathcal{F}_i(\boldsymbol{v}) \leq 0 \, , && \text{for } i = 1, ..., M \, , \\ &\qquad\qquad v_1^{min} \leq v_{1,j} \leq v_1^{max}, && \text{for } j = 1, ..., N_d \, , \\ &\qquad\qquad v_2^{min} \leq v_{2,j} \leq v_2^{max}, && \text{for } j = 1, ..., N_d \, , \end{aligned}} \tag{5.32}$$

where subscripts 1 and 2 denote the solid and porous material variable pair for each elements. Two additional constraints $\mathcal{F}_i(\boldsymbol{v})$ are added in order not to use a higher amount $W^{(i)}$ of material than the allowed one $W_0^{(i)}$ both for solid $(i = 1)$ and porous $(i = 2)$:

$$\mathcal{F}_1(\boldsymbol{v}) = W^{(1)}(\boldsymbol{v}) - W_0^{(1)} \leq 0 \, , \tag{5.33}$$

$$\mathcal{F}_2(\boldsymbol{v}) = W^{(2)}(\boldsymbol{v}) - W_0^{(2)} \leq 0 \, . \tag{5.34}$$

As in Chapter 3, the optimization problem is solved at each iteration by the use of the gradient-based MMA [40] due to the high number of design variables, which involves that it is not possible to state that the solution reached after meeting the stopping criterion is the global optimal design. The computation of the sensitivities of $\mathcal{F}_0$ with respect to the design variables is performed by using the standard adjoint method [48]. Additionally, no filtering of sensitivities is performed.

5.5.1. Stopping criteria

Contrary to Chapter 3.5 where intermediate values of υ_j were acceptable in terms of manufacturability, in this Chapter, the final design should consist of air, solid and porous elements (respectively black/white/red in the following figures), and therefore all variable pairs $\{\upsilon_{1,j}, \upsilon_{2,j}\}$ should be either 0 or 1. In order to speed up calculations, the optimization process will be stopped when a certain amount of grey (intermediate values of $\upsilon_{i,j}$) is achieved, with $\mathcal{F}_{grey} \leq 0.02$ for Problems 1–3, where $\mathcal{F}_{grey}$ is defined below:

$$\mathcal{F}_{grey}(\boldsymbol{\upsilon}) = \frac{2}{N_d} \sum_{i=1}^{2} \sum_{j=1}^{N_d} \upsilon_{i,j} \left(1 - \upsilon_{i,j}\right) \ . \tag{5.35}$$

5.6. Results

5.6.1. Material properties

The aim of this study is to obtain acoustically optimized bi-material structures consisting of solid and porous parts. A plastic polymer with $E_s = 1.6$ GPa, $\rho_s = 920$ kg/m^3 and $\nu_s = 0.4$ has been considered hereinafter in this Section. Additionally, a polyurethane foam of low flow resistivity (R =5000 Pa·s/m^2) has been considered as a porous material. The equivalent acoustic impedance Z_p and wavenumber k_p are provided by the Delany-Bazley equations [81], recalled in Section 3.2.1.2:

$$Z_p = Z_0 \left(1 + a_5 \sigma^{a_6} - j a_7 \sigma^{a_8}\right) \ , \tag{5.36}$$

$$k_p = k_0 \left(1 + a_3 \sigma^{a_4} - j a_1 \sigma^{a_2}\right) \ , \tag{5.37}$$

where $\sigma = f\rho_0/R$ and $a_1 = 0.168$, $a_2 = -0.715$, $a_3 = 0.136$, $a_4 = -0.491$, $a_5 = 0.114$, $a_6 = -0.369$, $a_7 = 0.0985$, $a_8 = -0.758$ were empirically obtained for the aforementioned material [114]. Finally, the impedance and wavenumber of the air are $Z_0 = \rho_0 c_0$, $k_0 = 2\pi f/c_0$, assuming $\rho_0 = 1.225$ kg/m^3 and $c_0 = 340$ m/s . The reader is referred to Section 5.3 for the obtaining of the vibroacoustic properties K and G.

5.6.2. Design 1. Duct screen

A first problem has been performed to illustrate the behaviour of the implemented methodology and compare it with similar results in the literature [33], where only air and material have been considered. The flexible duct partition shown in Figure 5.3 is optimized, in order to minimize the integral of the pressure's absolute value at the outlet section Γ_o. The excitation is modelled via a 500 Hz incoming wave through the left boundary Γ_e, whereas Γ_o is an anechoic termination. Both boundary conditions can be expressed by Eq. (5.17), where the excitation's amplitude P_e is chosen to be 1 Pa; whereas it is zero for the anechoic outlet [33, 87]. The domain has been meshed using 0.001 m square elements, obtaining 10000 elements within Ω_d.

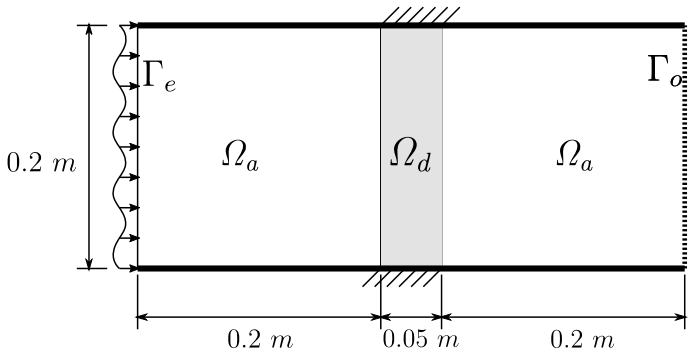

Figure 5.3: Problem 1 scheme.

Optimization has been set up with initial $\{v_{1,j} = 0.4, v_{2,j} = 0.6\}$ for $j = 1, ..., N_d$; obtaining $W_0^{(1)} = 0.4$ and $W_0^{(2)} = 0.36$, whereas a volume fraction of 0.24 has been obtained for the air. The weight of the acoustic analysis w_1 has been set to 1, whereas no structural TO problem has been considered ($w_2 = 0$), based on a preliminary test, and since the optimization frequency

is relatively low (see Figure 5.5). After 20 iterations, the stopping criterion is met. The optimized topology $\boldsymbol{v}^{opt}$ has been shown in Figure 5.4.

Figure 5.4: Optimized topology of Ω_d. Design 1.

As depicted in Figure 5.4, a chain-like solid structure has been obtained (similar to the one obtained in [33]), with porous material inside. The partition's acoustic performance for both initial (Fig. 5.3) and optimized (Fig. 5.4) topologies have been evaluated in a wide range of frequencies. Results are shown in Figure 5.5:

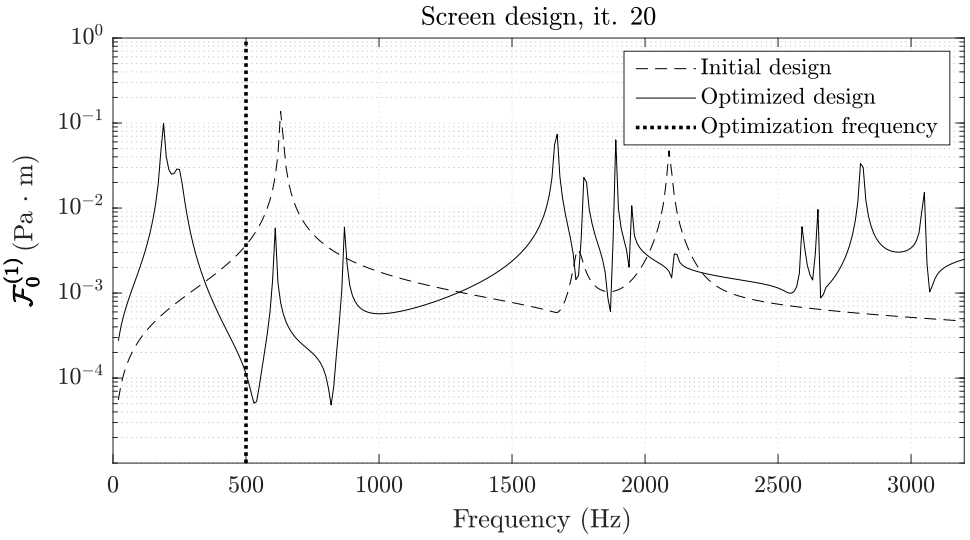

Figure 5.5: $\mathcal{F}_0^{(1)}$ provided by the initial and optimized topologies. Design 1.

It was expected that by optimizing at 500 Hz, the first natural frequency of the structure (initially at around 600 Hz) would be normally shifted right (i.e, moved away from the optimization frequency). However, for the optimized structure a new natural frequency has appeared at around 200 Hz. In any case, $\mathcal{F}_0^{(1)}$ decreases at 500 Hz from $3.660{\cdot}10^{-3}$ Pa·m to $1.124{\cdot}10^{-4}$ Pa·m.

5.6.3. Design 2. Duct shielding

Second, a ventilation duct's shielding has been optimized at 4000 Hz. A 2D simplified scheme of the problem is shown in Figure 5.6a (only one quarter of the domain is modelled due to biaxial symmetry). In order to model the sound source, a pressure value P_E of 1 Pa is prescribed at the centre of the duct. As in Problem 1 (see Section 5.6.2), the pressure's absolute value has been integrated along Γ_o in order to obtain $\mathcal{F}_0^{(1)}(\boldsymbol{v})$. However, an additional elastic problem has been introduced in order to guarantee the structural continuity for the solid material. A distributed force p_{int} of 1 Pa/m has been considered along the inner boundary of the duct (see Figure 5.6b).

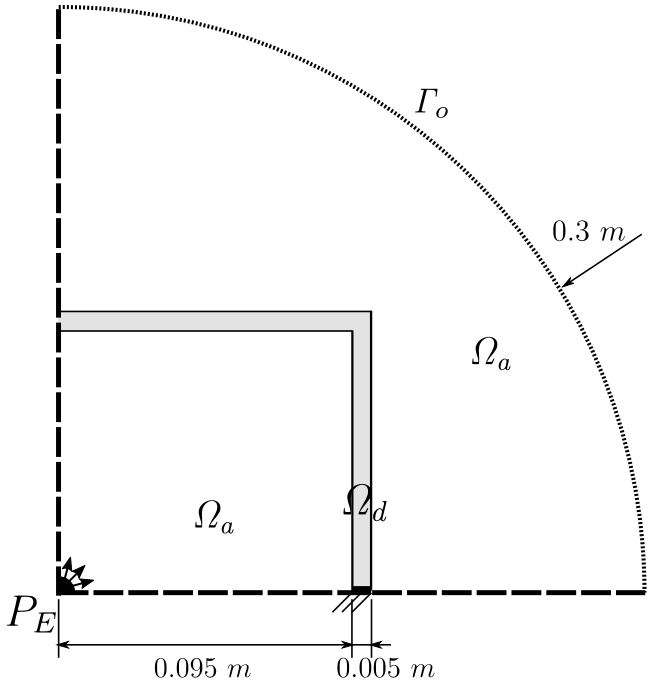

(a) Fluid-structure problem.

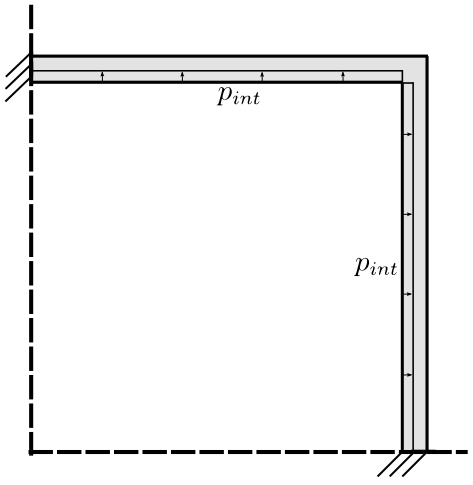

(b) Elastic problem.

Figure 5.6: Problem 2 scheme.

By setting $w_1 = 1$ (acoustic problem) and $w_2 = 0.4$ (elastic problem), and after 40 iterations, the optimized topology is shown in Figure 5.7, and it can be seen that a structure with holes has been obtained again for the solid phase. The duct contains solid material in both the inner and outer faces, i.e., it is structurally convenient, thanks to the contribution of the elastic TO problem shown in Figure 5.6b.

Figure 5.7: Optimized topology of Ω_d. Design 2.

The acoustic performance of both initial and optimized topologies has been evaluated and is shown in Figure 5.8. $\mathcal{F}_0^{(1)}$ at 4000 Hz effectively drops from $4.528{\cdot}10^{-3}$ Pa·m (initial design) to $2.174{\cdot}10^{-3}$ Pa·m (for the optimized design). Additionally, the compliance of the structure under the inner pressure decreases from $1.495{\cdot}10^{-2}$ J (for the initial topology) to $5.872{\cdot}10^{-4}$ J (after optimization).

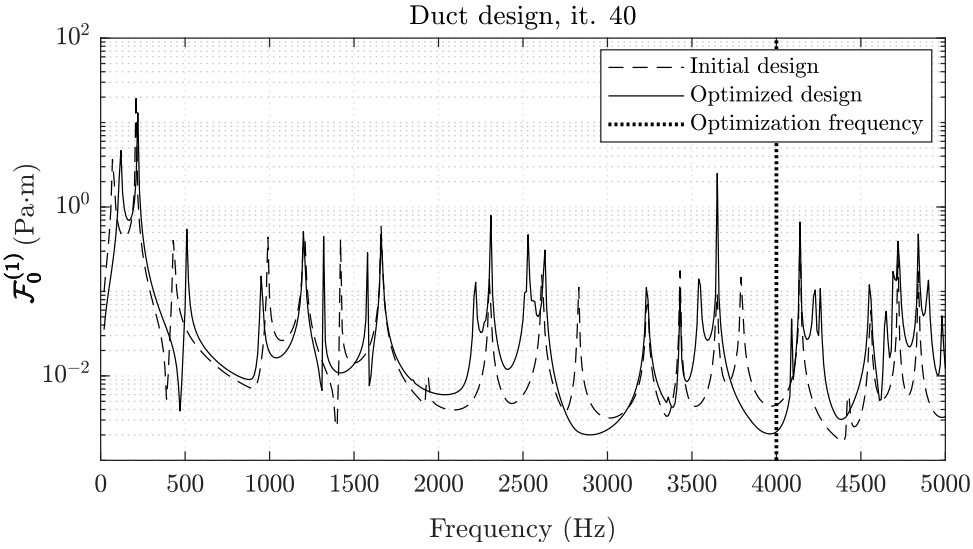

Figure 5.8: $\mathcal{F}_0^{(1)}$ provided by the initial and optimized topologies. Design 2.

Finally, Figure 5.9 shows the distribution of acoustic pressure within Ω_a for both topologies.

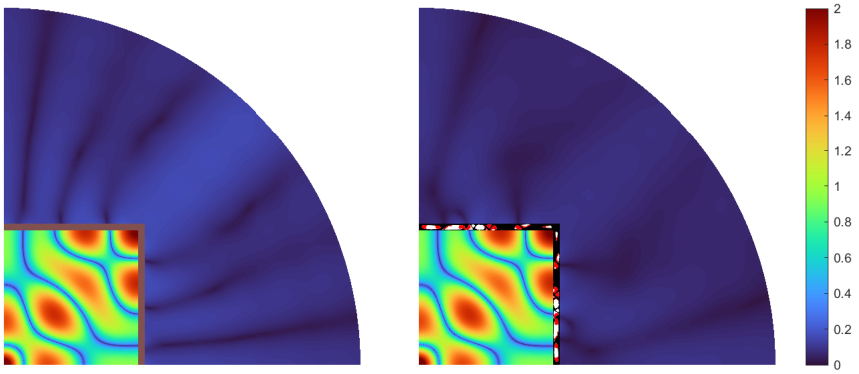

(a) Initial topology. **(b)** Optimized topology.

Figure 5.9: Amplitude of pressure oscillation $|p|$. Design 2.

5.6.4. Design 3. Train fairing

Finally, a train fairing has been optimized in order to reduce the rolling noise radiated to the environment. In order to show the ability of the method to consider a wide variety of excitation types, the response of the wheel studied in [115] to a 400 Hz excitation is obtained and plugged as a displacement field U perpendicular to the wheel's surface $\Gamma_e \subset \Gamma_a$ by following Eq. (5.11). An additional static problem is considered, based on a preliminary test, in order to guarantee the structural continuity of the optimized topology. A distributed force f_d with a resultant of 1 N is applied at the lower tip of the fairing (see Figure 5.10b).

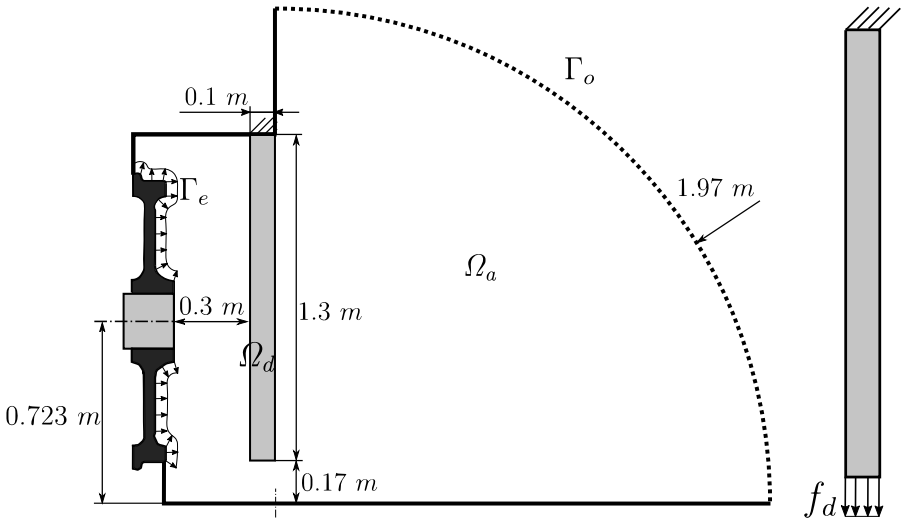

(a) Fluid-structure problem. **(b)** Elastic problem.

Figure 5.10: Problem 3 scheme.

By setting coefficients $w_1 = 1$ (acoustic problem) and $w_2 = 0.4$ (elastic problem), and after 19 iterations, the optimized topology is shown in Figure 5.11. Regarding the solid material, a design resembling a chain with holes has been obtained again, whereas the porous material design consists of equally spaced bands.

Figure 5.11: Optimized topology of Ω_d. Design 3.

The acoustic performance of both initial and optimized topologies has been evaluated and is shown in Figure 5.12. The acoustic objective function $\mathcal{F}_0^{(1)}$ at 400 Hz decreases from 4.193 Pa·m (for the initial topology) to 0.9400 Pa·m (for the optimized design). Figure 5.13 shows the distribution of acoustic pressure within Ω_a for both topologies.

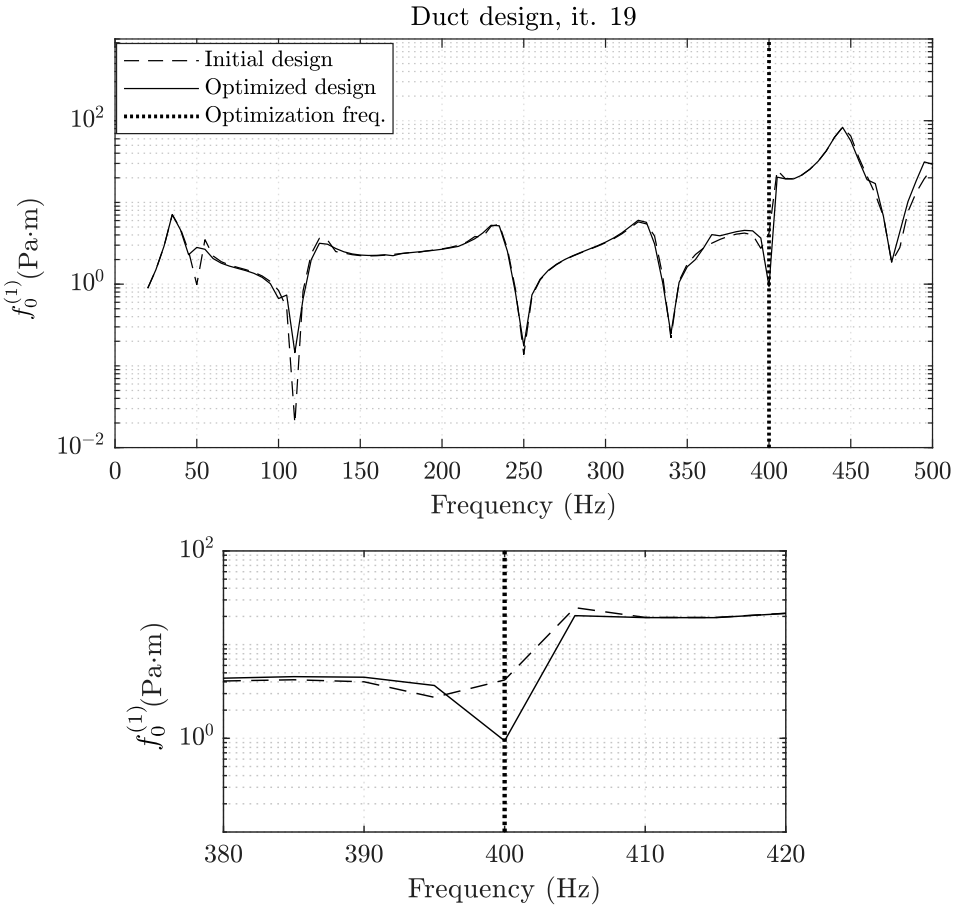

Figure 5.12: $\mathcal{F}_0^{(1)}$ provided by the initial and optimized topologies. Design 3.

Additionally, the compliance of the structure $\mathcal{F}_0^{(2)}$ under the load case depicted in Figure 5.10b halves from 0.03160 J to 0.01679 J after optimization.

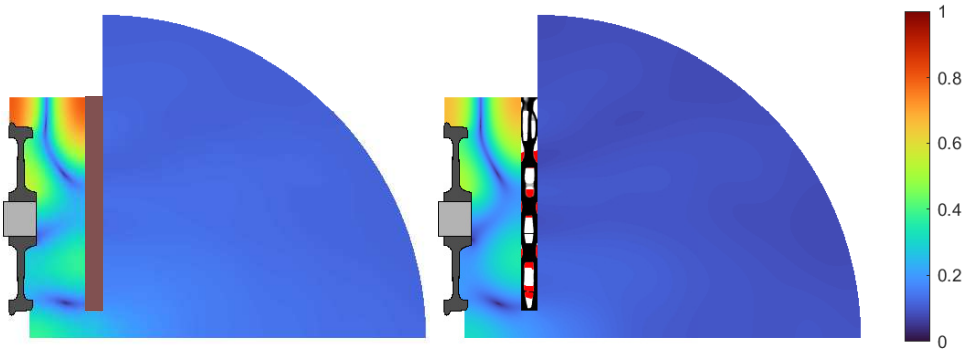

(a) Initial topology. **(b)** Optimized topology.

Figure 5.13: Amplitude of pressure oscillation $|p|$. Design 3.

5.7. Conclusions

This Chapter presents a topology optimization method to effectively increase the attenuation of elastic screens by applying the $\mathbf{u}$/p mixed formulation in the vibroacoustic area whereas the standard pressure formulation is employed in the rest of the problem's domain, hence decreasing computational cost.

A three-material interpolation scheme is also introduced in this Chapter in order to obtain designs with both solid and porous material.
The optimization problem is solved by the use of the iterative algorithm MMA, which requires the gradient of both the objective function and the restrictions with respect to all design variables at each design step. The adjoint method, along with the analytical derivation of the global matrices with respect to each design variable, allows the evaluation of the sensitivities of the objective function.

Results show that for the solid material, optimized designs resemble a chain with several aligned holes; whereas the distribution of porous material is harder to generalize. Also, [33] showed that structural continuity is not ensured for high optimization frequencies in comparison to the first natural

frequencies of the initial structure. In this Chapter, a static TO problem with a realistic structural force is introduced in order to circumvent this problem.

Chapter 6

Conclusions

In this Chapter, the main conclusions and contributions obtained in the present Thesis are presented.

The conclusions obtained in the present Thesis, concerning the development of efficient acoustic optimization methods of mufflers, aftertreatment devices, and sound barriers, are detailed below.

The fundamentals of sound theory have been recalled. The use of three-dimensional models (such as the pressure-formulation FEM, a hybrid pressure-velocity potential FEM, and other simplified approaches such as the MMM in combination with the FEM) has been justified for the acoustic analysis of mufflers and aftertreatment devices, considering thermal gradients and non-homogeneous bulk density distributions of dissipative material within the chamber.

A TO procedure has been proposed for the acoustic optimization (TL maximization) of dissipative and hybrid mufflers along a target frequency range. For this purpose, the MMA and the adjoint method have been successfully applied to the scheme. Non-trivial distributions of the dissipative material within the chamber have been obtained, that resemble designs already studied, including several rings with different material densities, and extended ducts.

To conclude, the aforementioned scheme has allowed obtaining high levels of attenuation, even with small amounts of porous material, by optimizing its distribution within the chamber.

Additionally, a sizing and shape optimization of aftertreatment devices (CC and DPF) has been implemented, by using a previous in-house code that combines the use of the MMM and the FEM for the study of axially-uniform cross sections of the chamber. A GA has been applied to optimize the position of the inlet and outlet ducts, but also other geometric parameters, such as the length of the monolith and chamber, and the type of the former. It has been derived from the study that the position of the inlet and outlet ducts has the biggest influence, and should be different, such that the transversal acoustic modes excited by the inlet are not able to transmit their energy to the outlet. Therefore the latter should be strategically positioned at the nodes of the modes transmitting the most energy, at the given frequency.

Finally, the vibroacoustic TO problem has been addressed by considering the mixed displacement-pressure formulation (applied only in the design region), in combination with the standard pressure formulation. A three-

material scheme is considered for the obtaining of two-material (solid, porous) sound barriers.

A methodology has been obtained, for designing non trivial structures containing holes and porous infills, with a view to reducing noise emissions in multiple applications, such as a ventilation duct coating or a train fairing.

Chapter 7

Further publications

Some relevant contributions related to the present PhD Thesis are listed below:

7.1. International journals (JCR)

i. B. Ferrándiz, F.D. Denia, J. Martínez-Casas, E. Nadal, J.J. Rodenas, "Topology and shape optimization of dissipative and hybrid mufflers", *Structural and Multidisciplinary Optimization*, vol. 62, pp. 269–284, 2020. https://doi.org/10.1007/s00158-020-02490-x.

ii. B. Ferrándiz, F.D. Denia, J. Martínez-Casas, E. Nadal, J.J. Ródenas, "Acoustic topology optimization using a mixed formulation and a three-material scheme", submitted to *Structural and Multidisciplinary Optimization*, 2023.

7.2. National congresses

i. B. Ferrándiz, E. Nadal, J. Martínez-Casas, J.J. Ródenas, F.D. Denia. "Metodologías avanzadas de optimización geométrica y topológica en dispositivos de control de ruido", *XXII Congreso Nacional de Ingeniería Mecánica (CNIM)*, pp. 1278-1288. ISSN 0212-5072. Madrid 2018.

ii. B. Ferrándiz, F.D. Denia, J. Martínez-Casas, E. Nadal, J.J. Ródenas, "Control pasivo de ruido ferroviario mediante optimización topológica y formulación mixta", *Congreso de Métodos Numéricos en Ingeniería (CMN)*, pp. 161-173. ISBN 978-989-54496-0-6. Guimaraes 2019.

iii. E.M. Sánchez-Orgaz, F.D. Denia, B. Ferrándiz, J. Martínez-Casas, E. Nadal, "Optimización acústica de catalizadores de automoción", *Congreso de Métodos Numéricos en Ingeniería (CMN)*, pp. 112-125. ISBN 978-989-54496-0-6. Guimaraes 2019.

7.3. International congresses

i. B. Ferrándiz, L. Giovannelli, J. Albelda, E. Nadal, M. Tur. "Structural Simulation of metal foams from CT scans using machine learning techniques in the cgFEM framework", *6th European Conference on Computational Mechanics. 7th European Conference on Computational Fluid Dynamics (ECCM-ECFD)*. Glasgow 2018.

ii. E. Nadal, B. Ferrándiz, M. Tur Valiente, J.J. Ródenas, F.J. Fuenmayor Fernández. "Image-base material homogenization using Neural Networks under the cgFEM framework", *13th World Congress on Computational Mechanics (WCCM)*. New York 2018.

iii. B. Ferrándiz, J. Martínez-Casas, E. Nadal, J.J. Ródenas, F.D. Denia. "Advanced Methodologies for Topology and Geometry Optimization of Noise Control Devices", *6th International Conference on Engineering Optimization (ENGOPT)*, pp. 1154-1165. ISBN 978-3-319-97772-0. Lisbon 2018. http://doi.org/10.1007/978-3-319-97773-7_100

iv. B. Ferrándiz, F.D. Denia, J. Martínez-Casas, E. Nadal, J.J. Ródenas. "Railway rolling noise minimization by topology optimization techniques using the mixed FE formulation", *IX International Conference on Adaptive Modeling and Simulation (ADMOS)*. El Campello 2019.

v. B. Ferrándiz, E. Nadal, J. Martínez-Casas, F.D. Denia, J.J Ródenas, "Railway rolling noise minimization by topology optimization techniques using the mixed FE formulation", *48th International Congress and Exposition on Noise Control Engineering (Inter-Noise)*, pp. 10-21. ISBN 978-84-87985-31-7. Madrid 2019.

vi. F.D. Denia, E.M. Sánchez-Orgaz, B. Ferrándiz, J. Martínez-Casas, L. Baeza, "Efficient finite element modelling of sound propagation in after treatment devices with arbitrary cross section", *XXII Mathematical*

Modelling in Engineering & Human Behaviour, pp. 1-4. ISSBN 978-84-09-25132-2. Valencia 2020.

vii. B. Ferrándiz, F.D. Denia, J. Martínez-Casas, E. Nadal, J.J. Ródenas. "Topology Optimization of acoustic screens using a mixed formulation: Applications", *6th ECCOMAS Young Investigators Conference (YIC)*. Online, 2021.

viii. F.D. Denia, B. Ferrándiz, J. Martínez-Casas, L. Baeza, E.M. Sánchez-Orgaz, "Sound propagation in after-treatment devices with arbitrary cross section. Modelling and acoustic performance optimization", *27th International Congress on Sound and Vibration (ICSV)*, pp. 1603-1610. ISBN 978-1-7138-3516-5. Prague 2021.

Bibliography

[1] M. N. Harkude and R. R. Malagi, "Automobile noise and vibration-sources, prediction, and control", *Indian Journal of Scientific Research*, vol. 12, pp. 1–6, 2015.

[2] L. Fritschi, A. Brown, R. Kim, D. Schwela, and S. Kephalopoulos, *Burden of Disease from Environmental Noise Quantification of healthy life years lost in Europe*. World Health Organization. Regional Office for Europe, 2011.

[3] D. Thompson, *Railway Noise and Vibration: Mechanisms, Modelling and Means of Control*. Elsevier Ltd, 2009.

[4] J. Gutiérrez-Gil, X. Garcia-Andrés, J. Martínez-Casas, E. Nadal, and F. D. Denia, "Optimized perforation schemes in railway wheels toward acoustic radiation mitigation", *Journal of Vibration and Acoustics*, vol. 142 (041009), 2020.

[5] X. Garcia-Andrés, J. Gutiérrez-Gil, J. Martínez-Casas, and F. D. Denia, "Wheel shape optimization approaches to reduce railway rolling noise", *Structural and Multidisciplinary Optimization*, vol. 62, pp. 2555–2570, 2020.

[6] X. Garcia-Andrés, *Development of innovative methodologies to reduce railway rolling noise through Genetic Algorithm-based shape optimization techniques*. Doctoral Thesis. Universitat Politècnica de Valencia, 2021.

[7] C. J. C. Jones and D. J. Thompson, "Rolling noise generated by railway wheels with visco-elastic layers", *Journal of Sound and Vibration*, vol. 231, pp. 779–790, 2000.

[8] I. A. Resitoglu, *NOx Pollutants from Diesel Vehicles and Trends in the Control Technologies*. Diesel and Gasoline Engines. IntechOpen, 2020.

[9] M. J. Crocker, *Handbook of Acoustics*, vol. 70. John Wiley and Sons, Ltd, 1998.

[10] P. M. Morse, K. U. Ingard, and F. B. Stumpf, *Theoretical Acoustics*, vol. 38. McGraw-Hill, 1970.

[11] J. W. S. B. Rayleigh, *The Theory of Sound*. Dover Publications, 1945.

[12] A. Broatch, X. Margot, A. Gil, and F. D. Denia, "A CFD approach to the computation of the acoustic response of exhaust mufflers", *Journal of Computational Acoustics*, vol. 13, pp. 301–316, 2005.

[13] M. L. Munjal, *Acoustics of ducts and mufflers*. John Wiley & Sons, 2nd ed., 2014.

[14] W. F. Hughes and E. W. Gaylord, *Basic Equations of Engineering Science*. McGraw-Hill Book Co., 1964.

[15] F. D. Denia, E. M. Sánchez-Orgaz, J. Martínez-Casas, and R. Kirby, "Finite element based acoustic analysis of dissipative silencers with high temperature and thermal-induced heterogeneity", *Finite Elements in Analysis and Design*, vol. 101, pp. 46–57, 2015.

[16] T. Morel, J. Morel, and D. A. Blaser, "Fluid dynamic and acoustic modeling of concentric-tube resonators/silencers", *SAE Technical Paper 910072*, 1991.

[17] A. Antebas, *Contribución al modelado acústico de la línea de escape de motores de combustión. Aplicación a silenciadores y catalizadores*. Tesis Doctoral. Universitat Politècnica de Valencia, 2010.

[18] L. L. Beranek, *Acoustics*. Acoustical Society of America, 1996.

[19] A. D. Pierce, "Wave equation for sound in fluids with unsteady inhomogeneous flow", *Journal of the Acoustical Society of America*, vol. 87, pp. 2292–2299, 1990.

[20] M. C. Potter and D. C. Wiggeri, *Mecanica de Fluidos*. Thomson International, 2002.

[21] F. D. Denia, A. Antebas, J. Martínez-Casas, and F. J. Fuenmayor, "Transmission loss calculations for dissipative mufflers with temperature gradients", *20th International Congress on Acoustics 2010, ICA 2010 - Incorporating Proceedings of the 2010 Annual Conference of the Australian Acoustical Society*, vol. 3, pp. 2117–2122, 2010.

[22] J. F. Allard and N. Atalla, *Propagation of Sound in Porous Media: Modelling Sound Absorbing Materials*. John Wiley and Sons, 2009.

[23] J. L. Bento, *Acoustic characteristics of perforate liners in expansion chambers*. Doctoral Thesis. University of Southampton, 1983.

[24] A. I. El-Sharkawy and A. H. Nayfeh, "Effect of an expansion chamber on the propagation of sound in circular ducts", *Journal of the Acoustical Society of America*, vol. 63, pp. 667–674, 1978.

[25] P. O. A. L. Davies, "Practical flow duct acoustics", *Journal of Sound and Vibration*, vol. 124, pp. 91–115, 1988.

[26] I. Babuška, B. Andersson, P. J. Smith, and K. Levin, "Damage analysis of fiber composites part i: Statistical analysis on fiber scale", *Computer Methods in Applied Mechanics and Engineering*, vol. 172, pp. 27–77, 1999.

[27] R. Payri, *Análisis de la atenuación producida por filtros acústicos: Síntesis y modelado de silenciadores de escape*. Tesis Doctoral. Universitat Politècnica de Valencia, 1999.

[28] F. D. Denia, *Modelado del comportamiento acústico de silenciadores de escape mediante técnicas analíticas y el método de elementos finitos*. Tesis Doctoral. Universitat Politècnica de Valencia, 2004.

[29] L. J. Eriksson, "Higher order mode effects in circular ducts and expansion chambers", *Journal of the Acoustical Society of America*, vol. 68, pp. 545–550, 1980.

[30] F. C. Karal, "The analogous acoustical impedance for discontinuities and constrictions of circular cross section", *Journal of the Acoustical Society of America*, vol. 25, pp. 327–334, 1953.

[31] A. D. Sahasrabudhe, M. L. Munjal, and S. A. Ramu, "Analysis of inertance due to the higher order mode effects in a sudden area discontinuity", *Journal of Sound and Vibration*, vol. 185, pp. 515–529, 1995.

[32] L. Shu, M. Y. Wang, and Z. Ma, "Level set based topology optimization of vibrating structures for coupled acoustic-structural dynamics", *Computers and Structures*, vol. 132, pp. 34–42, 2014.

[33] G. H. Yoon, J. S. Jensen, and O. Sigmund, "Topology optimization of acoustic-structure interaction problems using a mixed finite element formulation", *International Journal for Numerical Methods in Engineering*, vol. 70, pp. 1049–1075, 2007.

[34] K. J. Bathe, *Finite Element Procedures*. Pearson Education, 2006.

[35] O. Zienkiewicz, R. Taylor, and J. Z. Zhu, *The Finite Element Method: its Basis and Fundamentals: Seventh Edition*. Butterworth-Heinemann, 2013.

[36] B. D. Upadhyay, S. S. Sonigra, and S. D. Daxini, "Numerical analysis perspective in structural shape optimization: A review post 2000", *Advances in Engineering Software*, vol. 155, p. 102992, 2021.

[37] M. P. Bendsøe and O. Sigmund, *Topology Optimization. Theory, Methods, and Applications*. Springer, 2002.

[38] M. P. Bendsøe and O. Sigmund, *Topology optimization by distribution of isotropic material*. Topology Optimization. Springer Berlin Heidelberg, 2004.

[39] X. S. Yang, *Engineering Optimization: An Introduction with Metaheuristic Applications*, vol. 160. John Wiley and Sons, 2010.

[40] K. Svanberg, "The method of moving asymptotes—a new method for structural optimization", *International Journal for Numerical Methods in Engineering*, vol. 24, pp. 359–373, 1987.

[41] O. Sigmund, "Morphology-based black and white filters for topology optimization", *Structural and Multidisciplinary Optimization*, vol. 33, pp. 401–424, 2007.

[42] M. B. Dühring, J. S. Jensen, and O. Sigmund, "Acoustic design by topology optimization", *Journal of Sound and Vibration*, vol. 317, pp. 557–575, 2008.

[43] K. H. Kim and G. H. Yoon, "Optimal rigid and porous material distributions for noise barrier by acoustic topology optimization", *Journal of Sound and Vibration*, vol. 339, pp. 123–142, 2015.

[44] D. Yang, H. Liu, W. Zhang, and S. Li, "Stress-constrained topology optimization based on maximum stress measures", *Computers and Structures*, vol. 198, pp. 23–39, 2018.

[45] B. Ferrándiz, F. D. Denia, J. Martínez-Casas, E. Nadal, and J. J. Ródenas, "Topology and shape optimization of dissipative and hybrid mufflers", *Structural and Multidisciplinary Optimization*, vol. 62, pp. 269–284, 2020.

[46] M. Stolpe and K. Svanberg, "An alternative interpolation scheme for minimum compliance topology optimization", *Structural and Multidisciplinary Optimization*, vol. 22, pp. 116–124, 2001.

[47] K. Svanberg, "A class of globally convergent optimization methods based on conservative convex separable approximations", *SIAM Journal on Optimization*, vol. 12, pp. 555–573, 2002.

[48] J. S. Jensen, *Topology optimization.* In: F. Romeo and M. Ruzzene, "Wave Propagation in Linear and Nonlinear Periodic Media". CISM Courses and Lectures, vol 540. Springer Vienna, 2012.

[49] J. H. Holland, *Adaptation in natural and artificial systems: an introductory analysis with applications to biology, control, and artificial intelligence.* MIT Press, 1975.

[50] A. Tripathy and H.-P. Schwefel, "Numerical optimization of computer models", *Journal of the Operational Research Society*, vol. 33, p. 1166, 1982.

[51] L. J. Fogel, A. J. Owens, and M. J. Walsh, *Artificial intelligence through a simulation of evolution.* Evolutionary Computation: The Fossil Record. Wiley-IEEE Press, 1998.

[52] C. Darwin, *On the Origin of Species by Means of Natural Selection, or the Preservation of Favored Races in the Struggle for Life.* Murray, 1959.

[53] S. N. Sivanandam and S. N. Deepa, *Introduction to genetic algorithms.* Springer Berlin Heidelberg, 2008.

[54] *Global Optimization Toolbox Documentation.* Mathworks Simulink, 2016.

[55] M. P. Bendsøe and N. Kikuchi, "Generating optimal topologies in structural design using a homogenization method", *Computer Methods in Applied Mechanics and Engineering*, vol. 71, pp. 197–224, 1988.

[56] O. Sigmund, "A 99 line topology optimization code written in Matlab", *Structural and Multidisciplinary Optimization*, vol. 21, pp. 120–127, 2001.

[57] R. Barbieri and N. Barbieri, "Finite element acoustic simulation based shape optimization of a muffler", *Applied Acoustics*, vol. 67, pp. 346–357, 2006.

[58] G. Zoutendijk, *Methods of feasible directions: a study in linear and non-linear programming.* Elsevier Pub. Co., 1960.

[59] Y. C. Chang and M. C. Chiu, "Shape optimization of one-chamber perforated plug/non-plug mufflers by simulated annealing method", *International Journal for Numerical Methods in Engineering*, vol. 74, pp. 1592–1620, 2008.

[60] K. F. D. Lima, A. Lenzi, and R. Barbieri, "The study of reactive silencers by shape and parametric optimization techniques", *Applied Acoustics*, vol. 72, pp. 142–150, 2011.

[61] O. Sigmund and K. Maute, "Topology optimization approaches: A comparative review", *Structural and Multidisciplinary Optimization*, vol. 48, pp. 1031–1055, 2013.

[62] J. W. Lee and Y. Y. Kim, "Topology optimization of muffler internal partitions for improving acoustical attenuation performance", *International Journal for Numerical Methods in Engineering*, vol. 80, pp. 455–477, 2009.

[63] E. L. Yedeg, E. Wadbro, and M. Berggren, "Interior layout topology optimization of a reactive muffler", *Structural and Multidisciplinary Optimization*, vol. 53, pp. 645–656, 2016.

[64] J. W. Lee, "Optimal topology of reactive muffler achieving target transmission loss values: Design and experiment", *Applied Acoustics*, vol. 88, pp. 104–113, 2015.

[65] F. M. Azevedo, M. S. Moura, W. M. Vicente, R. Picelli, and R. Pavanello, "Topology optimization of reactive acoustic mufflers using a bi-directional evolutionary optimization method", *Structural and Multidisciplinary Optimization*, vol. 58, pp. 2239–2252, 2018.

[66] G. H. Yoon, "Acoustic topology optimization of fibrous material with Delany-Bazley empirical material formulation", *Journal of Sound and Vibration*, vol. 332, pp. 1172–1187, 2013.

[67] A. Selamet, M. B. Xu, I. J. Lee, and N. T. Huff, "Dissipative expansion chambers with two concentric layers of fibrous material", *International Journal of Vehicle Noise and Vibration*, vol. 1, pp. 341–357, 2005.

[68] A. Selamet, M. B. Xu, I. J. Lee, and N. T. Huff, "Effect of voids on the acoustics of perforated dissipative silencers", *International Journal of Vehicle Noise and Vibration*, vol. 2, pp. 357–372, 2006.

[69] A. Selamet, I. J. Lee, and N. T. Huff, "Acoustic attenuation of hybrid silencers", *Journal of Sound and Vibration*, vol. 262, pp. 509–527, 2003.

[70] M. C. Chiu, "Optimization design of hybrid mufflers on broadband frequencies using the genetic algorithm", *Archives of Acoustics*, vol. 36, pp. 795–822, 2011.

[71] S. H. Lee and J. G. Ih, "Empirical model of the acoustic impedance of a circular orifice in grazing mean flow", *Journal of the Acoustical Society of America*, vol. 114, pp. 98–113, 2003.

[72] J. W. Sullivan and M. J. Crocker, "Analysis of concentric-tube resonators having unpartitioned cavities", *Journal of the Acoustical Society of America*, vol. 64, pp. 207–215, 1978.

[73] J. W. Sullivan, "A method for modeling perforated tube muffler components. i. theory", *Journal of the Acoustical Society of America*, vol. 66, pp. 772–778, 1979.

[74] T. H. Melling, "The acoustic impendance of perforates at medium and high sound pressure levels", *Journal of Sound and Vibration*, vol. 29, pp. 1–65, 1973.

[75] D. Ronneberger, "The acoustical impedance of holes in the wall of flow ducts", *Journal of Sound and Vibration*, vol. 24, pp. 133–150, 1972.

[76] X. Sun, X. Jing, H. Zhang, and Y. Shi, “Effect of grazing-bias flow interaction on acoustic impedance of perforated plates”, *Journal of Sound and Vibration*, vol. 254, pp. 557–573, 2002.

[77] F. D. Denia, A. Selamet, F. J. Fuenmayor, and R. Kirby, “Acoustic attenuation performance of perforated dissipative mufflers with empty inlet/outlet extensions”, *Journal of Sound and Vibration*, vol. 302, pp. 1000–1017, 2007.

[78] R. Kirby and F. D. Denia, “Analytic mode matching for a circular dissipative silencer containing mean flow and a perforated pipe”, *Journal of the Acoustical Society of America*, vol. 122, pp. 3471–3482, 2007.

[79] U. Ingard, “On the theory and design of acoustic resonators”, *Journal of the Acoustical Society of America*, vol. 25, pp. 1037–1061, 1953.

[80] V. A. Fok, *Doklady Akademii nauk SSSR 31.* Schaums Outline Series, 1941 (in Russian). Alternatively, see: S.N. Rschevkin, "A Course of Lectures on the Theory of Sound". Pergamon, 1964.

[81] M. E. Delany and E. N. Bazley, “Acoustical properties of fibrous absorbent materials”, *Applied Acoustics*, vol. 3, pp. 105–116, 1970.

[82] R. Kirby and A. Cummings, “Prediction of the bulk acoustic properties of fibrous materials at low frequencies”, *Applied Acoustics*, vol. 56, pp. 101–125, 1999.

[83] D. R. A. Christie, “Measurement of the acoustic properties of a sound absorbing material at high temperatures”, *Journal of Sound and Vibration*, vol. 46, pp. 347–355, 1976.

[84] F. D. Denia, E. M. Sánchez-Orgaz, L. Baeza, and R. Kirby, “Point collocation scheme in silencers with temperature gradient and mean flow”, *Journal of Computational and Applied Mathematics*, vol. 291, pp. 127–141, 2016.

[85] P. T. Williams, R. Kirby, C. Malecki, and J. Hill, “Measurement of the bulk acoustic properties of fibrous materials at high temperatures”, *Applied Acoustics*, vol. 77, pp. 29–36, 2014.

[86] A. G. Antebas, F. D. Denia, A. M. Pedrosa, and F. J. Fuenmayor, "A finite element approach for the acoustic modeling of perforated dissipative mufflers with non-homogeneous properties", *Mathematical and Computer Modelling*, vol. 57, pp. 1970–1978, 2013.

[87] E. M. Sánchez-Orgaz, *Advanced numerical techniques for the acoustic modelling of materials and noise control devices in the exhaust system of internal combustion engines.* Doctoral Thesis. Universitat Politécnica de Valencia, 2016.

[88] K. S. Peat and K. L. Rathi, "A finite element analysis of the convected acoustic wave motion in dissipative silencers", *Journal of Sound and Vibration*, vol. 184, pp. 529–545, 1995.

[89] S. S. Rao, *The finite element method in engineering.* Butterworth Heinemann, 5th ed., 2017.

[90] K. E. Atkinson, *An introduction to numerical analysis.* Wiley, 1989.

[91] R. Kirby, P. T. Williams, and J. Hill, "The effect of temperature on the acoustic performance of splitter silencers", *42nd International Congress and Exposition on Noise Control Engineering 2013, INTER-NOISE 2013: Noise Control for Quality of Life*, vol. 7, pp. 5826–5833, 2013.

[92] F. D. Denia, A. Selamet, M. J. Martínez, and A. J. Torregrosa, "Hybrid mufflers with short lateral chambers: Analytical, numerical and experimental studies", *13th International Congress on Sound and Vibration 2006, ICSV 2006*, vol. 2, pp. 1064–1071, 2006.

[93] M. Åbom, F. D. Denia, and A. J. Torregrosa, *Modeling of IC Engine Silencers and Tailpipe Noise: 1D and 3D Approaches.* in A. Onorati, G. Montenegro. 1D and Multi-D Modeling Techniques for IC Engine Simulation. SAE International, 2020.

[94] E. Dokumaci, "Sound transmission in narrow pipes with superimposed uniform mean flow and acoustic modelling of automobile catalytic converters", *Journal of Sound and Vibration*, vol. 182, pp. 799–808, 1995.

[95] R. J. Astley and A. Cummings, "Wave propagation in catalytic converters: Formulation of the problem and finite element to solution scheme", *Journal of Sound and Vibration*, vol. 188, pp. 635–657, 1995.

[96] A. Selamet, V. Easwaran, J. M. Novak, and R. A. Kach, "Wave attenuation in catalytic converters: Reactive versus dissipative effects", *Journal of the Acoustical Society of America*, vol. 103, pp. 935–943, 1998.

[97] S. Allam and M. Åbom, "Acoustic modelling and testing of diesel particulate filters", *Journal of Sound and Vibration*, vol. 288, pp. 255–273, 2005.

[98] S. Allam and M. Åbom, "Sound propagation in an array of narrow porous channels with application to diesel particulate filters", *Journal of Sound and Vibration*, vol. 291, pp. 882–901, 2006.

[99] F. D. Denia, E. M. Sánchez-Orgaz, B. Ferrándiz, J. Martínez-Casas, and L. Baeza, "Efficient finite element modelling of sound propagation in after-treatment devices with arbitrary cross section", *Mathematical Modelling for Engineering and Human Behaviour (MMEHB)*, pp. 59–65, 2020.

[100] F. D. Denia, J. Martínez-Casas, J. Carballeira, E. Nadal, and F. J. Fuenmayor, "Computational performance of analytical methods for the acoustic modelling of automotive exhaust devices incorporating monoliths", *Journal of Computational and Applied Mathematics*, vol. 330, pp. 995–1006, 2018.

[101] E. Dokumaci, "On transmission of sound in circular and rectangular narrow pipes with superimposed mean flow", *Journal of Sound and Vibration*, vol. 210, pp. 375–389, 1998.

[102] A. D. Pierce, *Acoustics*. Acoustical Society of America, 1991.

[103] A. M. Stamatelos, "A review of the effect of particulate traps on the efficiency of vehicle diesel engines", *Energy Conversion and Management*, vol. 38, pp. 83–99, 1997.

[104] A. Selamet and Z. L. Ji, "Acoustic attenuation performance of circular expansion chambers with extended inlet/outlet", *Journal of Sound and Vibration*, vol. 223, pp. 197–212, 1999.

[105] R. Kirby, "Transmission loss predictions for dissipative silencers of arbitrary cross section in the presence of mean flow", *Journal of the Acoustical Society of America*, vol. 114, pp. 200–209, 2003.

[106] E. Wadbro and M. Berggren, "Topology optimization of an acoustic horn", *Computer Methods in Applied Mechanics and Engineering*, vol. 196, pp. 420–436, 2006.

[107] J. Luo and H. C. Gea, "Optimal stiffener design for interior sound reduction using a topology optimization based approach", *Journal of Vibration and Acoustics, Transactions of the ASME*, vol. 125, pp. 267–273, 2003.

[108] J. Du and N. Olhoff, "Minimization of sound radiation from vibrating bi-material structures using topology optimization", *Structural and Multidisciplinary Optimization*, vol. 33, pp. 305–321, 2007.

[109] M. B. Søndergaard and C. B. Pedersen, "Applied topology optimization of vibro-acoustic hearing instrument models", *Journal of Sound and Vibration*, vol. 333, pp. 683–692, 2014.

[110] L. Shu, M. Y. Wang, Z. Fang, Z. Ma, and P. Wei, "Level set based structural topology optimization for minimizing frequency response", *Journal of Sound and Vibration*, vol. 330, pp. 5820–5834, 2011.

[111] R. Picelli, W. M. Vicente, and R. Pavanello, "Evolutionary topology optimization for structural compliance minimization considering design-dependent FSI loads", *Finite Elements in Analysis and Design*, vol. 135, pp. 44–55, 2017.

[112] A. Cummings and R. J. Astley, "The effects of flanking transmission on sound attenuation in lined ducts", *Journal of Sound and Vibration*, vol. 179, pp. 617–646, 1995.

[113] L. Kinsler, A. Frey, A. Coppens, and J. Sanders, *Fundamentals of Acoustics*. Wiley, 2000.

[114] I. P. Dunn and W. A. Davern, "Calculation of acoustic impedance of multi-layer absorbers", *Applied Acoustics*, vol. 19, pp. 321–334, 1986.

[115] J. Gutiérrez-Gil, X. Garcia-Andrés, J. Martínez-Casas, E. Nadal, and F. D. Denia, "Mitigation of railway wheel rolling noise by using advanced optimization techniques", *Proceedings of the 6th International Conference on Engineering Optimization (EngOpt 2018)*, pp. 1141–1153, 2019.